Spectrally resolved Extreme Ultraviolet Lensless Imaging With High-Order Harmonic Generation Sources

Xiaomeng Liu

Spectrally resolved Extreme Ultraviolet Lensless Imaging With High-Order Harmonic Generation Sources

Xiaomeng Liu

VRIJE UNIVERSITEIT

Spectrally resolved Extreme Ultraviolet Lensless Imaging With High-Order Harmonic Generation Sources

ACADEMISCH PROEFSCHRIFT

ter verkrijging van de graad Doctor of Philosophy
aan de Vrije Universiteit Amsterdam,
op gezag van de rector magnificus
prof.dr. J.J.G. Geurts,
in het openbaar te verdedigen
ten overstaan van de promotiecommissie
van de Faculteit der Betawetenschappen
op maandag 16 september 2024 om 13.45 uur
in een bijeenkomst van de universiteit,
De Boelelaan 1105

door

Xiaomeng Liu

geboren te Shandong, China

promotoren: dr. S.M. Witte
prof.dr. K.S.E. Eikema

promotiecommissie: prof.dr. A.J. den Boef
prof.dr. M.S. Pchenitchnikov
prof.dr. I.M.N. Groot
dr. P.M. Kraus
prof.dr. P. Eng-Johnsson

This work was carried out at the Advanced Research Center for
Nanolithography (ARCNL), a public-private partnership between the
University of Amsterdam (UvA), Vrije Universiteit Amsterdam (VU),
Rijksuniversiteit Groningen (RUG), the Dutch Research Council (NWO), and
the semiconductor equipment manufacturer ASML.
This work was supported by the European Research Council (project
LENSLESS, grant agreement no. 637476).

Cover: Concept and design by Xiaomeng Liu
Printed by: ProefschriftMaken, Amsterdam, The Netherlands
DOI: http://doi.org/10.5463/thesis.729
A digital version of this thesis is available at: https://research.vu.nl/

“Whether you think you can, or you think you can’t – you’re right.”

– Henry Ford

Contents

1 Introduction **9**

1.1 Microscopy and lensless imaging 9
1.2 Coherent diffractive imaging and Ptychography 10
1.3 High-order harmonic generation 13
1.4 Phase matching and chromatic aberration 16
1.5 Table top extreme ultra-violet radiation source 18
1.6 Structure of this thesis 21

2 Spectrally resolved coherent diffractive imaging **23**

2.1 Introduction 23
2.2 Experiment and multispectral image reconstruction 24
2.3 Spectral data extraction 26
2.4 Discussion and conclusion 28

3 Tailoring spatial entropy in EUV focused beams **31**

3.1 Introduction 32
3.2 Spatial entropy minimization 33
3.3 Simulation 36
3.4 Multispectral ptychography 42
  3.4.1 Forward model 42
  3.4.2 Multistep-propagation 42
  3.4.3 Regularization 43
3.5 Polychromatic ptychography with structured illumination 44
  3.5.1 NIR setup 44
  3.5.2 Structured versus smooth illumination in monochromatic ptychography 45
  3.5.3 Structured versus smooth illumination in multispectral ptychography 46
3.6 Experimental results 48
  3.6.1 Zone plate design considerations for EUV ptychography . . 48
  3.6.2 Nanofabrication 49
  3.6.3 Experimental setup 51
  3.6.4 Ptychography scan 51
3.7 Discussion and conclusion 53

4 Ptychographic EUV wavefront sensing **55**
- 4.1 Introduction 56
- 4.2 Methods 57
  - 4.2.1 Experiment 57
  - 4.2.2 Binary mask design for ptychographic wavefront sensing . . 59
- 4.3 Results and discussion 60
- 4.4 Conclusion 68

5 Chromatic aberration in HHG **71**
- 5.1 Introduction 72
- 5.2 Setup for ptychographic wavefront sensing 74
- 5.3 Results: HHG wavefronts and chromatic aberrations 75
- 5.4 Discussion 77
- 5.5 Conclusion 82
- 5.6 Appendix 82
  - 5.6.1 Calculating HHG focus position from fundamental beam reconstructions 82
  - 5.6.2 HHG beam diameters at the generation plane 84
  - 5.6.3 Harmonic-resolved beam profile reconstructions 85

Summary **87**

Acknowledgments **89**

Bibliography **93**

Chapter 1

Introduction

1.1 Microscopy and lensless imaging

Optical microscopy has been an essential method for examining and characterizing the microscale realm since the 17th century with the invention of compound lens microscopes. Today, advances in technology, including semiconductors, nanoscience, and quantum technology, have elevated the expectations for microscopy to provide not only high-resolution imaging of complex 3D nanoscale structures but also to quantify their physical and chemical properties, and even monitor dynamic processes.

To attain nanoscale resolution using optical microscopes, technology needs be pushed to its fundamental limits. The primary hurdle is the optical diffraction limit, which dictates that the maximum resolution of a microscope is restricted by the numerical aperture and wavelength of the light used. Several approaches have been explored to overcome this limit, including increasing the numerical aperture using materials with high or even negative refractive indices [1, 2], or utilizing shorter wavelengths for illumination such as extreme ultraviolet (EUV) or X-ray radiation. Moreover, it has been demonstrated that resolutions surpassing the diffraction limit are achievable by employing special illumination schemes such as stimulated emission depletion (STED) [3].

Coherent diffraction imaging (CDI) offers an attractive solution to high-resolution imaging. This technique uses the coherent diffraction patterns of light that scattered from a sample as a starting point, and reconstructs an object image by numerical means instead of physical optical components [4, 5]. In CDI, the phase of the diffraction pattern is numerically retrieved from the measured intensity data, after which the reconstructed optical field at the sample location can be found. The straightforward and cost-effective nature of CDI makes it a promising alternative to more complex and expensive high-resolution imaging methods, especially at short wavelength.

1.2 Coherent diffractive imaging and Ptychography

CDI is a computational imaging technique [4]. Instead of using conventional imaging lenses, the spatial information of the object is computationally reconstructed using the recorded diffraction amplitude and an iterative image reconstruction algorithm. To understand the algorithm, it is necessary to first look at the numerical calculation of the beam propagation.

According to scalar diffraction theory [6], the diffraction pattern as observed at a distance behind an object is related to the electric field of light directly after the object (the 'exit wave') through the Huygens Fresnel principle. This exit wave $E(x, y)$ is a product of the probe light shining on the object $P(x, y)$ and the object function $O(x, y)$ that describes the sample

$$E(x, y) = P(x, y) \cdot O(x, y). \tag{1.1}$$

After free space propagation over a distance z, this electric field will evolve to a new electric field $E(x, y, z)$, which can be written as the inverse Fourier transform of the angular spectrum of the original electric field $\hat{E}(k_x, k_y, 0)$ multiplied with a propagation phase factor $e^{iz\sqrt{k^2-k_x^2-k_y^2}}$

$$E(x, y, z) = \int\int \hat{E}(k_x, k_y, 0)e^{iz\sqrt{k^2-k_x^2-k_y^2}}e^{-i(k_x x+k_y y)}dk_x dk_y. \tag{1.2}$$

The angular spectrum $\hat{E}(k_x, k_y, 0)$ can be obtained by taking the Fourier transform of the initial field,

$$\hat{E}(k_x, k_y, 0) = \int\int E(x', y', 0)e^{-i(k_x x+k_y y)}dk_x dk_y, \tag{1.3}$$

where prime denotes source plane coordinates. The numerical evaluation of this angular spectrum propagation can be efficiently performed using two Fourier transforms:

$$E(x, y, z) = \mathscr{F}^{-1}\{\mathscr{F}\{(E(x', y', 0)e^{iz\sqrt{k^2-k_x^2-k_y^2}}\}\}. \tag{1.4}$$

This expression provides a generally applicable solution to calculate the field at a propagation distance z from the initial exit wave. If z is much larger than a wavelength, it is possible to simplify the transfer function and reduce the angular spectrum propagation function to a simpler *Rayleigh-Sommerfeld diffraction integral* [6],

$$E(x, y, z) = \frac{1}{i\lambda}\int\int E(x', y', 0)\frac{z}{r}\frac{e^{ikr}}{r}dx'dy', \tag{1.5}$$

which can be used to calculate the propagation between parallel and nonparallel planes.

In the approximation that propagation distance z is much larger than the diffraction pattern, a second-order Taylor expansion can be applied to r to simuplify the Rayleigh-Sommerfeld diffraction equation Eq. 1.5. This Fresnel approximation results in a different expression:

$$E(x,y,z) = \frac{e^{ikz} e^{\frac{x^2+y^2}{2z}}}{\lambda z i} \int \int E(x',y',0) e^{ik\frac{(x'^2+y'^2)}{2z}} e^{-ik(\frac{xx'}{z}+\frac{yy'}{z})} dx'dy'. \qquad (1.6)$$

The Fresnel approximation is only valid when the diffraction angle is small. If the propagation distance is large enough, the propagated electric field further reduces to a scaled version of the Fourier transform of the original electric field, in this case, the diffraction can be referred to as *Fraunhofer diffraction*, which is the simplest form of the propagation equation. To determine which propagator is suitable for the application, the Fresnel number F is a convenient parameter to use as a criterion:

$$F = \frac{a^2}{z\lambda}, \qquad (1.7)$$

where a is the dimension of the object, z is the propagation distance, λ is the wavelength. When the Fresnel number is close to 1 (i.e., F $\sim$ 1), the Fresnel integral approximation, Eq. 1.6 can be used to model diffraction effects accurately. This approximation is appropriate when the observation plane is in the near-field region, where the curvature of the wavefront is significant. When the Fresnel number is much smaller than 1 (i.e., F $<<$ 1), Fraunhofer diffraction applies and the diffraction pattern can be modeled as the Fourier transform of the exit wave.

In a coherent diffractive imaging experiment, a camera is used to record the intensity of the diffraction. If the phase information is also known, it will be possible to combine the amplitude information stored in the diffraction pattern and the phase information to directly propagate the electric field from the camera plane to the object plane, and an image of the object can be obtained. However, because of the fast oscillating electromagnetic field of light, no camera or photo diode can record the phase information of the field. Therefore, an iterative phase retrieval algorithm is used to retrieve phase information in the camera plane, allowing the reconstruction of spatial information of the object [4].

In conventional CDI experiments, the sample or the object is generally required to be isolated [4, 7]. And if curved wave fronts are used as probe, ambiguity in the defocus value of the reconstruction will arise. In 2004, Rodenburg and Faulkner reviewed the work of Hoppe and came up with a new lensless imaging algorithm, Ptychography [8].

In a ptychography experiment, the sample is illuminated with a probe beam and sequentially scanned laterally at many positions of the sample with the probe beam, as shown in Fig. 1.1. A certain ratio of overlap is kept between each of the two adjacent scan positions, while the camera records the diffraction pattern for each exposure. The overlap between scan positions provides a large amount of redundant information, which in return allows for object reconstruction with a high resolution and a theoretically unlimited field of view. Ideally, as long as the oversampling condition is fulfilled, the true solution can be found [9], but in reality, when noise and other experimental imperfections are included, a significant overlap in the range of 50% or higher is usually required.

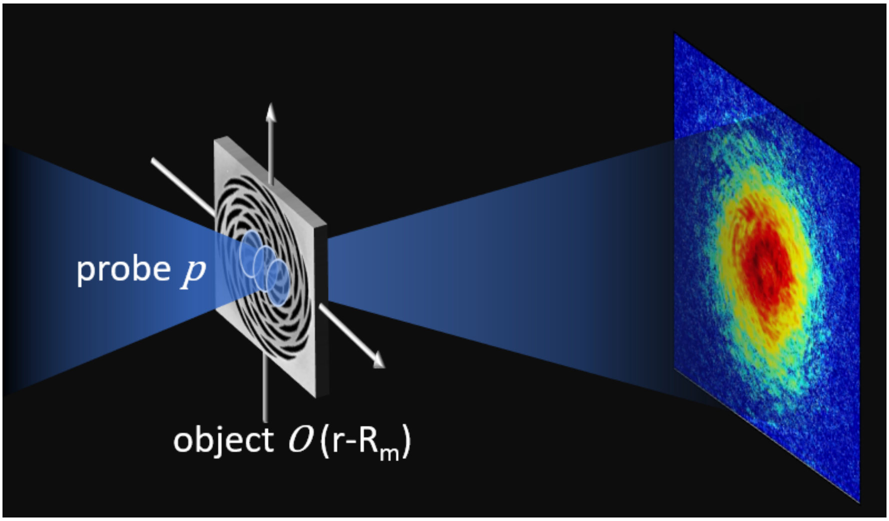

Figure 1.1: The schematic illustration depicts the scanning process of a sample using a probe beam P, in a raster scan grid. Each scan position is denoted as $O(r - R_m)$, where r is the real space coordinate and R_m is the sample translation vector.

In 2009, Maiden and Rodenburg further improved the ptychography algorithm and published *extended ptychographic iterative engine, ePIE* [10], which allowed simultaneous reconstruction of both the probe and object. This advancement marked a significant milestone in the development of ptychography.

However, it should be noted that maintaining high consistency of the probe throughout the ptychographic scan is a requirement for successful probe and object reconstruction.

Upon completion of a ptychographic scan, the acquired data set is ready to be entered into the reconstruction algorithm for image reconstruction. To start the image reconstruction, the algorithm starts with an initial guess of the complex probe function P_0 and the complex object transmission function O_0 , then it enters into the iterative update steps, here, and example of such update step is described, starting from the n^{th} updating step:

(1) Calculate the exit wave of the m^{th} scan position, $\psi_m = P_n \times O_n(r - R_m)$, where r is the real space coordinate, R_m is the translation vector of the sample, then the calculated exit wave ψ_m is numerically forward propagated to the camera plane over a distance z to obtain the propagated electric field, assuming far field diffraction, the calculated camera-plane complex electric field is $E_m = |E_m|e^{i\phi_m} = \mathscr{P}(\psi_m, z)$, where $\mathscr{P}$ denotes forward propagation over a distance z, $|E_m|$ the amplitude of the calculated electric field and ϕ_m the phase of the calculated field.

(2) Update the amplitude of the electric field $|E_m|$ with the camera measured

diffraction pattern I_m while keeping the calculated phase term, the updated electric field is $E_m^{'} = \sqrt{I_m} e^{i\phi_m}$.

(3) Inversely propagate the new electric field $E_m^{'}$ back to the object plane that is upstream to obtain the updated exit wave, $\psi_m^{'} = \mathscr{P}^{-1}(E_m^{'}, z)$, where$\mathscr{P}^{-1}$ denotes inverse propagation.

(4) Deconvolve the updated exit wave and updated object transfer function $O_m^{'}(r - R_n)$ and the updated probe function $P_m^{'}$ using the following rule:

$$O_n^{'}(r - R_m) = O_n(r - R_m) + \alpha \frac{P_n^*}{|P_n|^2}(\psi_m^{'} - \psi_m), \tag{1.8}$$

$$P_n^{'} = P_n + \beta \frac{O_n^*(r - R_m))}{|O_n(r - R_m)|^2}(\psi_m^{'} - \psi_m), \tag{1.9}$$

where P_n^* and O_n^* are the complex conjugate. The update sequence for this scan position is then finished. The updated probe and object function can be used as an initial guess for the $(m+1)^{th}$ scan position. After selecting a new scan position, repeat steps 1 to 4, until all the scan positions have been updated, and one full iteration has been completed.

(5) Calculate the error metric

$$Error_n = \Sigma_m \frac{\Sigma(x, y)|I_m(x, y) - |\psi_m(x, y)|^2|}{\Sigma_{(x,y)} I_m(x, y)}. \tag{1.10}$$

(6) Repeat through steps 1 to 5, until the error is small enough and the image of the object converges to a desired value.

Because ptychography offers a way to reconstruct the probe and object simultaneously without a priori knowledge, it can also be used for wavefront sensing. In Chapter 4, a detailed discussion of measuring multi-wavelength EUV wavefronts using ptychography is provided. In contrast to traditional ptychography techniques, which use a focused or confined probe beam to scan an extended sample, this project involves measuring and reconstructing an EUV beam that is freely propagated and spatially extended. This beam is larger than the test sample and includes numerous harmonics, all of which have similar wavefronts with minor variations. We show that multiple wavefronts of the harmonic beam can be reconstructed simultaneously. Note that a carefully designed wavefront sensor is required for this technique. The design considerations are discussed in detail in Chapter 4.

1.3 High-order harmonic generation

Despite the numerous advantages of CDI, several challenges must be addressed to fully realize its potential. In particular, CDI requires coherent and intense X-ray or electron sources and the acquisition of high-quality diffraction data, which can be difficult to achieve in practice. Therefore, the development and maturity of CDI imaging technology are highly dependent on advancements in illumination light sources.

In fact, the concept of recovering diffraction patterns to reconstruct images of the sample has been around for some time, but it was not until 1999 that CDI was first demonstrated using X-rays generated by synchrotron radiation sources (SRS) [4]. Since then, the advent of advanced synchrotron and X-ray free electron lasers (XFEL) has facilitated the development of CDI. However, widespread use of CDI was limited due to the high cost and complexity of large synchrotron facilities as well as limited access to beam time and beam lines. The development of femtosecond laser-based high-order harmonic generation (HHG) sources has challenged these limitations [11, 12]. HHG sources are significantly more cost-effective, compact, and energy-efficient than synchrotron and XFEL sources. The integration of HHG with CDI leverages the unique features of the HHG light source, including ultra-short pulses, ultra-broadband spectrum, high spatial coherence, and compactness, driving the development of lensless imaging techniques.

McPherson first reported the experimental observation of high-order harmonic generation in 1987, demonstrating the generation of the 17^{th} harmonic at 14.6 nm wavelength in neon using high peak intensity ultraviolet radiation [13]. Despite the groundbreaking nature of this discovery, the lack of a theoretical explanation resulted in limited attention from the scientific community. In 1993, Corkum and Krause et al. provided a detailed physical understanding of the HHG process with a semi-classical model [14, 15], that is commonly referred to as the "three-step model". This contribution paved the way for a deeper understanding of the HHG process and sparked increasing interest in this field.

When an atom is exposed in an extremely strong drive laser field, the field has to be treated as a strong perturbation to the Coulomb potential of the atom and significantly tilts the Coulomb potential. The highly tilted Coulomb potential allows weakly bound electrons to tunnel out with a certain probability and become quasi-free electrons traveling in the continuum band [16]. These electrons accelerate in the strong driving laser electric field and gain kinetic energy.

The electrons will take different trajectories in the continuum depending on the relative time of release, this is the time when the tunneling events take place with respect to the driving laser electric field phase. Due to the different trajectories, these electrons spend a different amount of time in the continuum and therefore accumulate different amounts of energies. Subsequently, when the electric field changes sign, the electrons will be driven back towards the parent ion. Only a small fraction of the electrons can be recaptured by the parent ions, leading to a low conversion efficiency. However, once the electrons recombine with the ion core, the accumulated kinetic energy will be released, leading to the emission of chirped broadband EUV pulses [17]. The repetitive nature of this process in a multicycle driving laser pulse then results in a comb-like HHG spectrum, with distinct peaks at frequencies corresponding to odd order harmonics of the driving laser frequency [18, 19].

The HHG spectrum usually consists of two regions, the plateau region and the cutoff region. In the plateau region, the conversion efficiency for different harmonics is very close to each other, whereas in the cutoff region, the conversion

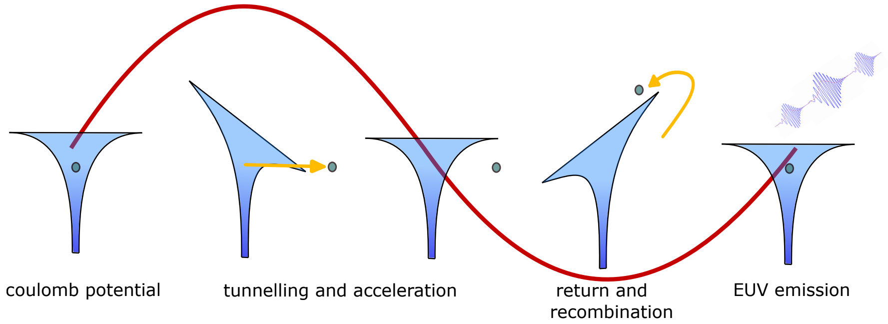

Figure 1.2: The schematic illustration of the three-step model. The red line represents the fundamental laser field, the blue funnel is the Coulomb potential, and the blue dot is the tunneling electron. Step 1, the Coulomb potential of the atom is tilted by the fundamental laser field, allowing the outer electron to tunnel out to the continuum. Step 2, the electron is driven by the fundamental laser field and travels in the continuum while accumulating energy. Step 3, recombination, the electron returns to the parent ion and releases the accumulated energy and emits EUV pulses.

efficiency decreases very rapidly as the harmonic order increases. The maximum achievable EUV photon energy is the sum of the ionization energy I_p plus the ponderomotive energy that the electron accumulated in the continuum U_p, which leads to the following expression

$$h\nu = I_p + 3.17U_p, \tag{1.11}$$

where the ponderomotive energy U_p is defined as:

$$U_p = \frac{e^2E^2}{4m_e\omega^2}, \tag{1.12}$$

with m_e the electron mass, E the strength of the drive laser electric field, ω the drive laser frequency. The formula reveals that the achievable photon energy of the generated EUV radiation depends only on three variables: the atom species, which determines the ionization potential, the laser intensity and frequency [20].

However, in an actual HHG experiment such a typical plateau and cutoff are not always observed, as practical aspects such as phase matching, plasma reabsorption and filter transmission all influence the HHG spectrum. A typical HHG spectrum is shown in Fig. 1.3.

Noble gases, such as helium, neon and argon, are commonly used in HHG experiments because of their favorable electronic structure and high ionization potential I_p, which allows a high degree of experimental control over the ionization process in HHG. A lower I_p would lead to more ionization, which may give more flux at lower harmonics, but the laser-produced plasma will make phase matching higher harmonics more difficult. An atom with higher I_p is more difficult to ionize at a given laser intensity, but a lower amount of laser produced plasma will in return help phase matching higher harmonic orders. Because no-

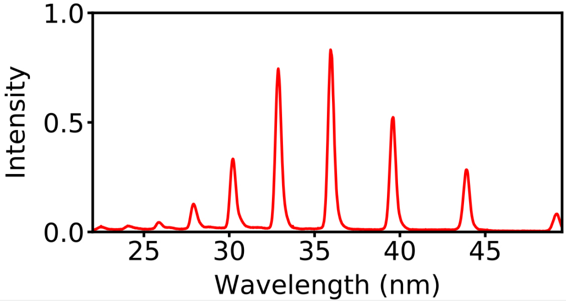

Figure 1.3: Experimentally observed HHG spectrum produced in a 1 mm wide jet of Argon gas with 25 fs, 800 nm laser pulses, as was typically used throughout the work described in this thesis. This particular spectrum was measured using Fourier-transform spectroscopy [21]

ble gases are inert, it is easier to work with them at high pressures, which is important for phase matching.

1.4 Phase matching and chromatic aberration

The three step model depicts the frequency up-conversion in an HHG event on the atomic level, but it does not give an explanation for the high degree of spatial coherence of the HHG beam [22, 23]. The key is the phase matching of the HHG process. Phase matching is the condition where the phase velocities of the fundamental laser beam and the generated harmonics are equal or nearly equal, allowing them to propagate coherently together over a longer distance in the medium. When phase matching is achieved, the harmonics add up constructively, leading to a higher conversion efficiency.

However, the nonlinear medium may exhibit complex dispersion. While the atoms lead to a negative phase dispersion between fundamental and EUV, the free electrons that are present after ionization add positive dispersion. In addition, the geometric phase of the drive laser and the atomic dipole phase can also affect the phase matching process. All these contributions should be balanced to achieve effective phase matching.

More specifically, for a loosely focused fundamental laser beam, the wavefront of the fundamental beam can be treated as a plane wave with a homogeneous intensity profile. The geometric phase and dipole phase can be then approximated to zero and the phase mismatch Δk is given by

$$\Delta k = \underbrace{-qp(1-\eta)\frac{2\pi}{\lambda_L}(\Delta\delta + n_2)}_{\text{neutral gas}} + \underbrace{qp\eta N_a r_e \lambda_L}_{\text{free electron}}, \tag{1.13}$$

where q is the high harmonic order, p is the pressure, η is the ionization fraction, λ_L is the fundamental laser wavelength, $\Delta\delta$ is the difference in the refractive index per bar between the fundamental and harmonic wavelength, n_2 is the nonlinear refractive index change due to the high intensity, N_a is the number of atoms per atmosphere and r_e is the classical electron radius [24].

For a tight focusing geometry, the geometric phase needs to be considered, which consists of the fundamental laser phase and the Gouy phase.

$$\phi_{Gouy} = -arctan\frac{z}{z_R}, \tag{1.14}$$

where z is the propagation distance relative to the focus and z_R the Rayleigh range and the fundamental laser phase $\phi_{fundamental}$. It contributes positively to phase mismatch. The dipole phase is the phase that an electron accumulated during the time between tunnel ionization and recombination. Therefore, this contribution depends on the trajectory that the electron takes and the intensity profile of the fundamental laser [25, 26]. It is obvious that the final harmonic phase is determined by many factors, and each of these factors can individually have a significant impact on the final harmonic phase and wavefront.

The generated EUV pulses are very short in duration, and due to their wide spectrum, the pulses can be further compressed to attosecond duration, making them a great tool for probing attosecond physics [27, 28].

However, such a broad bandwidth at such short wavelengths comes with complexities, as it will be sensitive to small spatial and/or temporal aberrations. To tightly focus such an attosecond HHG pulse and maintain its ultra-short duration, spatiotemporal coupling effects [25], dispersion [17, 29], and wavefront aberrations need to be controlled to a high degree. Although optical components may lead to such complications, it turns out that even the highly nonlinear HHG process itself can imprint spatiotemporal couplings in the generated EUV pulses [25, 30].

To understand the origin of such spatiotemporal coupling effects, one can start from how the HHG process induces harmonic-order-dependent wavefront aberrations. The phase of a high-harmonic field can be expressed as [25]:

$$\Phi_q(r,z) = q\phi(r,z) + \Phi_i(r,z), \tag{1.15}$$

where $\phi(r,z)$ is the drive laser phase, q is the harmonic order and $\Phi_i(r,z)$ is the atomic dipole phase [20, 31]. For an HHG beam with a Gaussian spatial intensity profile, the radius of curvature of the HHG wavefront can be obtained by approximating the phase with a polynomial expansion up to r^2 (considering only short trajectories), plus the wavefront curvature of the drive laser [25]:

$$\frac{1}{R_q} = \frac{1}{R_l(z)} + \frac{4\gamma_s c\,(q\omega_l - \omega_p)^2}{I_0 w_0^2 q\omega_l}, \tag{1.16}$$

in which $R_l(z)$ is the radius of curvature of the laser field at the gas jet, I_0 is the peak intensity, and w_0 is the beam waist, $\omega_p = I_p/\hbar$ is the frequency corresponding to the ionization energy I_p and $\gamma_s = a\omega_l^2$ with ω_l the laser frequency and a a constant. In this expression we can see that the HHG beam wavefront takes both contributions from drive laser wavefront and from the dipole phase, which has dependency on the harmonic order.

In Chapter 5, the wavefront of an HHG beam is characterized with a lensless imaging method known as ptychography, which allowed us to demonstrate this intrinsic chromatic aberration with unprecedented detail. It is shown that the high-harmonic generation process can have significant intrinsic chromatic aberration, particularly for converging incident laser fields. Furthermore, we identify regimes where such chromatic effects can be minimized and show that analytical models for the single-atom response allow for accurate redictions of the expected harmonic wavefronts produced by a specific driving field.

1.5 Table top extreme ultra-violet radiation source

The high-energy IR pulses that are used to drive the HHG are generated in a high-power ultra-fast laser system. A schematic overview is provided in Fig. 1.4.

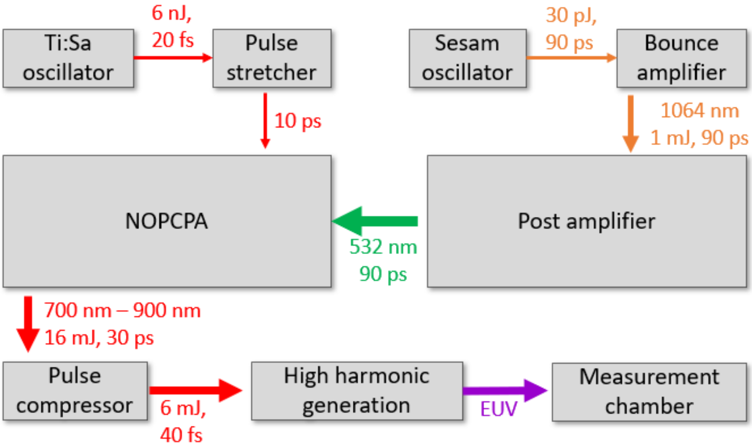

Figure 1.4: Schematic illustration of the high-power fundamental laser source.

The pulses are first generated in a Ti:Sapphire modelocked oscillator pumped with 532 nm CW laser. The pump beam is focused into the titanium-doped sapphire crystal, which leads to two lasing modes, continuous wave (CW) mode and pulsed mode. Within the laser crystal, the pump beam is focused to a spot size smaller than the CW mode. Femtosecond pulses are generated through Kerr-lens mode-locking, where self-focusing minimizes the mode size, thereby enhancing the gain for high-intensity pulsed operation over the CW mode [32]. It is important to note that in order to maintain the pulsed mode, the femtosecond pulses should retain their spectral phase, therefore dispersion needs to be compensated in the oscillator. To do this, chirped mirrors and a pair of thin glass wedges are used to control the dispersion.

Out of the Ti:Sa oscillator, the pulse energy is only a few nanojoules, while the pulse energy required to drive the HHG needs to be on the order of a few millijoules for some of the experiments described in this thesis. At the same time, the pulse must be sufficiently short to obtain a peak intensity of $10^{14} - 10^{15}\,\mathrm{W\,cm^{-2}}$.

To amplify the pulse to the desired energy level over its full ultra-wide bandwidth, non-collinear optical parametric chirped pulse amplification (NOPCPA) is used [33, 34]. In the NOPCPA module, the broadband IR pulses generated with the Ti:Sa oscillator are used as seed for the NOPCPA, and the seed beam is spatially overlapped with the high-intensity pump beam inside a birefringent BBO crystal. Facilitated by the second-order nonlinear susceptibility of the crystal, the energy of the pump photons is divided into two new photons at distinct wavelengths, governed by energy and momentum conservation. In the presence of a seed beam, one of these photons will be at the wavelength of the seed photons, thus acting as an amplification process.

This amplification is an instantaneous process, which means that not only the pump beam and seed beam need to overlap in space, but also need to arrive at the same time when entering the nonlinear crystal. This requires that the seed and the pump are synchronized in time, which is achieved with electronic synchronization.

A strict requirement for efficient amplification is phase matching. The wave number of the pump beam k_p needs to be a sum of the wave number of the signal k_s and the wave number of the idler k_i, $k_p = k_i + k_s$. This requirement can be met by tuning the phase matching angle θ, which is the angle between the pump beam and the optical axis of the birefringent crystal. However, because of the large spectral width of the signal beam, dispersion also needs to be managed in the propagation. This means that the group velocity of the signal beam should equal the group velocity of the idler beam along the direction of the seed beam. A second parameter that can be used to meet this requirement is the non-colinear angle, which is the angle between the pump and seed beams [33].

To ensure a high photon conversion efficiency, the duration of the seed pulse needs to be of the same order of magnitude as that of the pump pulse. If the seed pulse is much shorter than the pump pulse, the full spectrum will overlap with the most intense part of the pump pulse, then the full spectrum will be amplified, but due to the small overlap, the part before and after the signal seed in the pump pulse is not efficiently used. Stretching the seed pulse in this case will lead to an increase in the amplification efficiency. Care must be taken not to over stretch the seed pulse, as this will lead to a spectral narrowing since the outer part of the spectrum only overlaps with the weaker part of the pump pulse. Therefore, pulses generated from the Ti:Sa oscillator are sent through a grating-based pulse stretcher, where the amount of stretching can be precisely controlled.

The pump beam consists of intense pulses of 100 mJ pulse energy, 90 ps pulse duration at 532 nm wavelength, the repetition rate is 300 Hz [35]. The beam is split into two arms with a half wave plate and a thin film polarizer. A low power arm that carries 15 mJ pulse energy, which is used to preamplify the seed pulses, and a main arm carries the remaining 85 mJ pulse energy, which is used to amplify the pulse to the maximum energy. After splitting, the low power arm is demagnified to 2 mm in diameter and a top-hat intensity profile is imaged at the first BBO crystal, to ensure a homogeneous amplification of the seed pulse because the small-signal gain is exponentially dependent on the pump intensity.

$$I(z) \approx I(0)\frac{1}{4}e^{2gz}, \tag{1.17}$$

where $I(0)$ and $I(z)$ are the signal beam intensity before and after amplification and g is the parametric gain coefficient, which is proportional to the pump intensity [33].

The thickness of the BBO crystal is 5 mm to ensure a good amplification efficiency while keeping the group velocity dispersion under control. After the first pre-amplification, the pump pulse in the low power arm is still energetic enough to amplify the seed pulse a second time. Therefore, the beam is directed to the second BBO crystal, and again the top hat intensity profile is imaged onto this crystal.

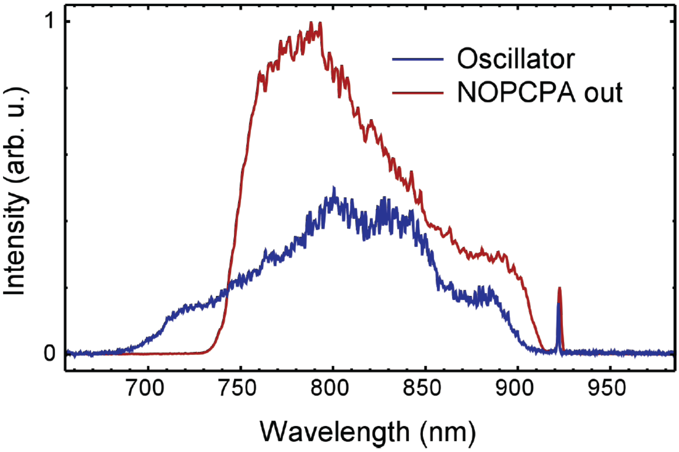

Figure 1.5: Spectrum measured out of the Ti:Sa oscillator in color blue and the spectrum meausred out of the NOPCPA after amplification in color red

After two preamplification stages, the seed pulse is amplified from several nJ per pulse to almost a mJ per pulse. The seed beam is magnified to 8 mm in diameter and meets the main arm in the last amplification stage and is amplified to 16 mJ. A typical spectrum of the seed beam before entering the NOPCPA and after amplification is shown in Fig 1.5.

The amplified IR pulse is spatially filtered by inserting a pinhole into the focus of a $4f$ relay imaging system. Subsequently, the pulses are sent to a grating-based compressor to compress the pulse from 50 ps to approximately 40 fs. The transmission through the spatial filter and compressor is about 50%, therefore, 7 to 8 mJ is available for driving the HHG.

1.6 Structure of this thesis

The thesis is structured as follows: In Chapter 2, spectrally resolved lensless imaging is used to achieve chemical element sensitivity using Fourier transform spectroscopy and, coherent diffractive imaging is introduced. In Chapter 3, a way of designing diffractive optical elements for broadband EUV radiation using the concept of spatial entropy is explored. It is shown that a specially designed zoneplate is able to focus multi-wavelength HHG beam to a desired focal spot, and the focusing property is characterized with multi-wavelength ptychography. In Chapter 4, high-resolution multiwavelength EUV wavefront sensing with ptychography is discussed. It is experimentally demonstrated that with a carefully designed wavefront sensor, multiple EUV wavefronts generated with HHG can be reconstructed simultaneously, which allows for studying the HHG physics. In Chapter 5, by recording ptychography data as a function of the HHG generation conditions, a detailed analysis of the intrinsic chromatic effects in the HHG process is investigated.

Chapter 2

Spectrally resolved coherent diffractive imaging

2.1 Introduction

The growing complexity of nano and quantum devices requires the use of high-precision imaging and metrology techniques to measure and characterize them. Imaging with extreme ultraviolet (EUV) radiation is an attractive option for such characterization, as many materials exhibit unique absorption and transmission characteristics in this wavelength range [36]. High-harmonic generation (HHG) serves as a tabletop EUV radiation source and produces broadband EUV radiation [11–13, 37], making it an excellent tool for characterizing nanostructures, including features that may be hidden underneath opaque layers that are not accessible with visible light.

As a first demonstration of the capabilities of HHG-based imaging, we present a spectrally resolved lensless imaging experiment utilizing a sample with a 3D compositional structure. Our non-destructive method is capable of extracting qualitative layer thickness information. This experiment is a first step towards element-sensitive metrology, and our approach can serve as a basis for more advanced high-precision imaging and metrology of microscopic 3D structures.

This project is built upon the concept of spatially resolved Fourier transform spectroscopy (FTS) [38–40], and diffractive shear interferometry (DSI) [21, 41].

In spatially resolved HHG-FTS, a set of phase-locked extreme ultraviolet (EUV) pulses is produced using two spatially separated HHG sources. These pulse pairs propagate through free space, and their wavefronts diverge, causing them to expand in size. Subsequently, they overlap and interfere in the far field, generating an interferogram. The interferogram images are recorded using a charge-coupled device (CCD) camera as a function of time delay between the two pulses. Fourier transforming the resulting data cube along the time axis produces the spectrum for each image pixel. By selecting the same spectral component over all pixels, monochromatic intensity images for each harmonic are obtained. Performing this technique when a sample is inserted in the beams allows for selecting the monochromatic exit wave for each spectral component, which fulfills the requirement for image reconstruction using DSI.

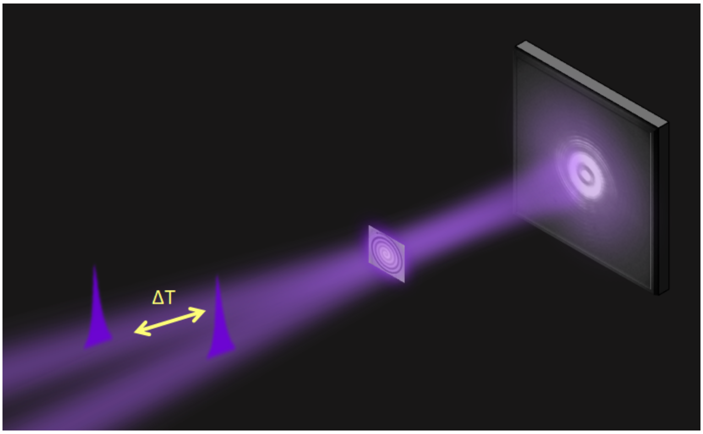

Figure 2.1: Schematic overview of the DSI measurement setup. Two identical and mutually coherent EUV beams illuminate the multilayer sample with a finite shear angle between them and a controlled time delay ΔT. A series of diffraction patterns is then recorded as a function of ΔT.

DSI employs these two identical and mutually coherent EUV pulse trains to illuminate the sample. The two beams are set up with slightly different angles, resulting in a shear between the two exit waves that leave the back surface of the sample, as illustrated in Fig. 2.1. The CCD camera placed downstream records the diffraction pattern, which is the coherent sum of the two exit waves in the far field. Similar to the Fourier-transform interferometry described above, by taking multiple measurements as a function of the delay time between the two EUV pulses trains, and performing FTS, we can extract the interference term at all harmonic frequencies. An iterative phase retrieval algorithm is used to retrieve the phase of the electric field at the camera plane [21]. Once the phase and amplitude of the camera plane electric field is known, the object plane exit wave can be obtained by taking an inverse Fourier transform of the camera plane field.

2.2 Experiment and multispectral image reconstruction

A multilayered sample was fabricated using sputter coating and focused ion beam (FIB) milling techniques. A 50 nm thick freestanding Si_3N_4 membrane was used as the substrate, coated with a 59 nm thick layer of titanium, followed by a 100 nm thick gold capping layer. A spiral shaped pattern is milled on the multilayer sample using the FIB (Fig. 2.2). The spiral shape with narrow linewidth will give rise to far-field diffraction patterns with significant information at larger diffraction angles, which aids DSI reconstruction.

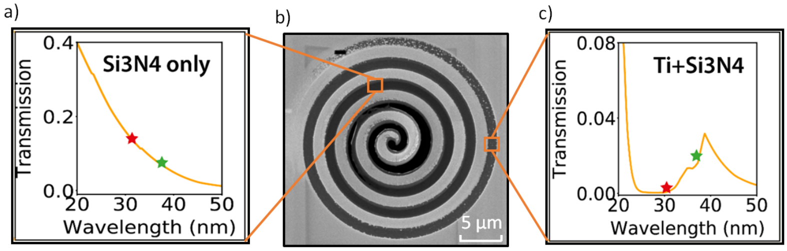

Figure 2.2: a) The transmission profile of the Si_3N_4 layer. The red star indicates the transmission at the 27^{th} harmonic (37 nm), while the green star indicates transmission at the 23^{th} harmonic (31 nm). b) Scanning electron microscope (SEM) image of the spiral sample. c) The transmission profile of the $Si_3N_4 + Ti$ layer. The red star indicates the transmission at the 27^{th} harmonic (37 nm), while the green star indicates transmission at the 23^{th} harmonic (31 nm).

An important ingredient of the design is that the spiral pattern has a varying depth profile from the center to the outside. At its center, all layers are completely removed, resulting in full transmission. As the spiral line progresses towards the outside, the Si_3N_4 layer starts to appear and gradually increases in thickness to 50 nm. The EUV transmission profile for a 50 nm Si_3N_4 layer is shown in Fig. 2.2a). Further towards the outside of the spiral, the Ti layer is also still present with gradually increasing thickness. The EUV transmission for 50 nm Si_3N_4 plus 59 nm Ti is shown in Fig. 2.2c). At the tail of the spiral, the full thickness is retained. In this region, the transmission is expected to drop to zero, as the gold layer is fully opaque for our HHG spectrum. To mark where the spiral ends, a fully transmissive rectangular hole is milled as a reference marker. A DSI measurement is performed on this multilayer sample with the HHG setup described in Chapter 1, depicted schematically in Fig. 2.1.

The two EUV beams have a relative angle of 0.4 mrad. This configuration resulted in two sheared copies of the diffraction pattern of the spiral sample, at the CCD camera placed 18 cm downstream. The CCD chip has 2048x2028 pixels with a size of 13.5 μm. The low transmission necessitated an 18-second integration time for each camera exposure, with 4-by-4 binning and 4× camera pre-amplifier gain. The scan was optimized for the high-harmonic generation (HHG) spectrum, with a time delay step of approximately 32 as, corresponding to 9.7 nm optical path difference, enabling measurement of the theoretically shortest wavelength of 19.4 nm. The entire experiment comprised 485 time steps, resulting in a total delay of 15.7 fs, spanning multiple optical cycles of the driving laser and ensuring sufficient spectral resolution. The monochromatic diffraction patterns for 37 nm (green) and 31 nm (red) resulting from the FTS measurement are shown in Fig. 2.3a and b. The wavelength scaling between the patterns at 31 and 37 nm is clearly visible.

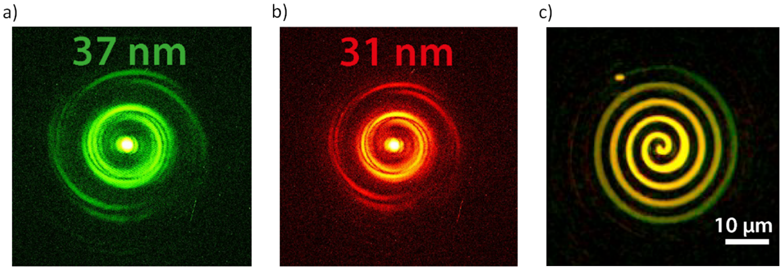

Figure 2.3: Monochromatic diffraction pattern at wavelength of a) 37 nm (green) and b) 31 nm (red). c) Image reconstructions superimposed at wavelengths of 37 nm (green) and 31 nm (red). A yellow color represents similar transmission at both wavelengths, while red or green color indicates increased transmission at 31 or 37 nm, respectively.

An iterative phase retrieval technique based on DSI is employed to reconstruct the images of the spiral at 31 and 37 nm wavelength from the diffraction pattern. The DSI approach is complemented by incorporating additional information obtained from FTS that captures the phase gradient in the direction of the shear [21]. This supplementary constraint augments the efficacy of the algorithm and accelerates its convergence. The reconstructed spiral transmissivity images at 31 and 37 nm are visually represented using color, where the former is assigned the color red and the latter green.

The two reconstructed spiral images are superimposed, as illustrated in Fig. 2.3c, with their transmissivities normalized at the center of the spiral where no material is present. The color of the composite image then reveals the relative strength of the two wavelengths. This central region thus appears yellow, indicating equal relative transmission for 31 and 37 nm. Moving towards the periphery, it can be seen that the color changes slightly towards the red in the region where only Si_3N_4 is present, and turns more green in the regions with Ti. These observations are consistent with the expectations from the known transmission of these materials (Fig. 2.2).

2.3 Spectral data extraction

In order to establish a correlation between the reconstructed image and the chemical composition of the spiral sample, Energy-dispersive X-ray spectroscopy (EDX) [42, 43] measurements were carried out, and the results are presented in Fig. 2.4a for the elements Si, Ti and Au. An EDX image encodes the abundance of the corresponding element in the brightness of the image. The Si image is representative of the Si_3N_4 layer, and appears dark in the center of the spiral, indicating that the layer has been completely removed. Along the spiral line, the brightness increases, indicating an increase in the thickness of the layer. Similar observations were made for the other two elements, but with different gradients and positions where the material is fully removed. .

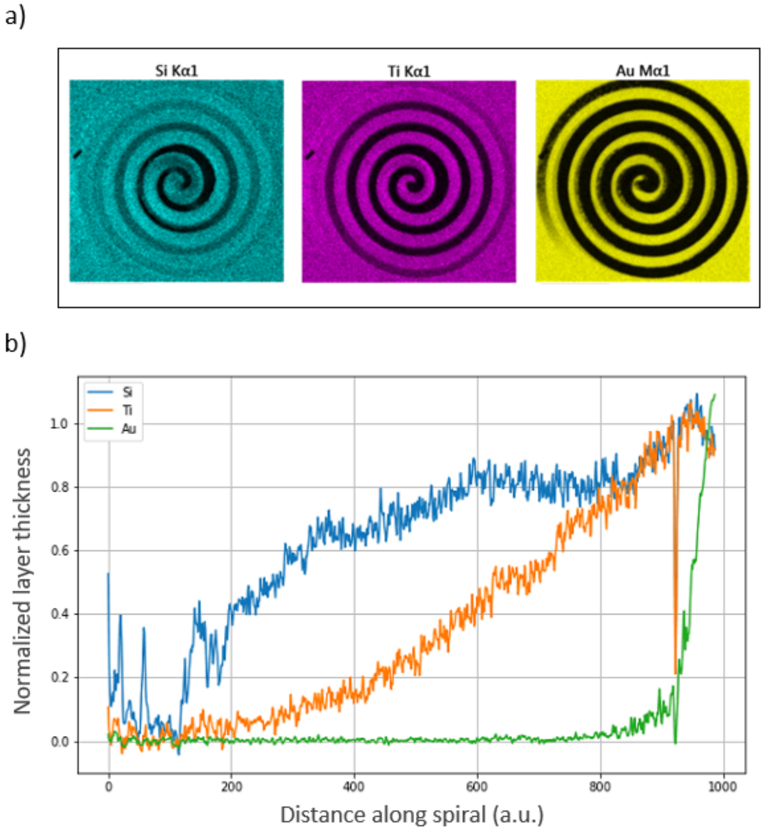

Figure 2.4: a) Energy-dispersive x-ray spectroscopy (EDX) measurements of the spiral sample: Si, Ti and Au data is shown. b) Line-out along the spiral on the EDX data, giving an indication of the local layer thicknesses.

The EDX data is analyzed by taking a line-out along the spiral line and normalizing it to the signal outside the spiral, as illustrated in Fig. 2.4b. This signal is interpreted as the local layer thickness d_l for each element. From this data, the EUV spectral transmission of each material is subsequently estimated through the utilization of a comprehensive X-ray database, provided by the Center for X-Ray Optics (CXRO) [44]. The Beer-Lambert Law is then used to derive the transmission as a function of layer thickness, following the expression: $T_{layer} = T_t^{d_l/d_t}$, where T_t and d_t are the expected transmission and the nominal thickness of the fabricated layers. Finally, the overall transmission of the spiral thin-film is calculated by multiplying the individual layer transmissions. Similarly, a line-out was taken from the DSI data, to determine the experimentally observed normalized transmissivity along the spiral. The comparison of the DSI and EDX results is shown in Fig. 2.5.

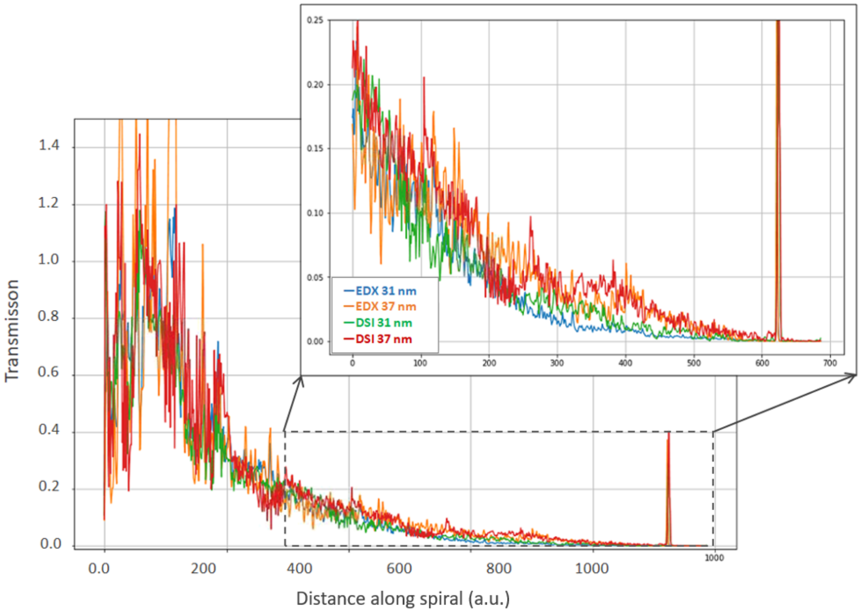

Figure 2.5: Comparison of the relative transmissivity along the spiral, as determined by DSI at 37 nm (red) and 31 nm (green) wavelength, and calculated from the layer thicknesses determined from EDX data for 31 nm (blue) and 37 nm (orange).

2.4 Discussion and conclusion

Qualitatively, good agreement is found between the transmission percentages extracted from the EDX data and from the DSI data. However, it is also noticeable that quantitative layer thickness information is challenging to extract solely based on the amplitude information provided by DSI: while there seems to be good correlation between EDX and DSI data at 31 and 37 nm, the noise on the transmissivity is at a similar level as the difference in signal at the different wavelengths. To obtain more accurate spectrally resolved and elemental information, the phase of the exit wave must be taken into consideration, which would enable a spatially resolved determination of the optical path length variation of the light traversing the film. In a DSI reconstruction, the phase information is mixed with the phase of the beam that is used to illuminate the sample, making it difficult to unambiguously retrieve the phase induced by the dispersive sample and separate it from the phase curvature of the illumination beam.

A lensless imaging technique called *ptychography* can overcome this issue [45, 46]. Through the iterative phase retrieval and image reconstruction algorithm, ptychography enables simultaneously reconstruct the complex electric field of the probe beam and the complex field of the sample. Our current experiment demonstrates both the capabilities and the limitations of DSI (and in general single-shot CDI-based methods) for element-resolved imaging. These results form a major motivation to push forward in the direction of ptychography, as a more powerful imaging concept that may enable quantitative spectrally resolved 3D imaging.

Chapter 3

Tailoring spatial entropy in extreme ultraviolet focused beams for multispectral ptychography

Diffractive optics can be used to accurately control optical wavefronts, even in situations where refractive components such as lenses are not available. For instance, conventional Fresnel zone plates (ZPs) enable focusing of monochromatic radiation. However, they lead to strong chromatic aberrations in multicolor operation. In this work, we propose the concept of spatial entropy minimization as a computational design principle for both mono- and polychromatic focusing optics. We show that spatial entropy minimization yields conventional ZPs for monochromatic radiation. For polychromatic radiation, we observe a previously unexplored class of diffractive optical elements (DOEs), allowing for balanced spectral efficiency. We apply the proposed approach to the design of a binary ZP, tailored to multispectral focusing of extreme ultraviolet (EUV) radiation from a high-harmonic tabletop source. The polychromatic focusing properties of these ZPs are experimentally confirmed using ptychography. This work provides a new route towards polychromatic wavefront engineering at EUV and soft-X-ray wavelengths.

The content of this chapter has been published as: L. Loetgering, X. Liu, A. C. C. de. Beurs, M. Du, G. Kuijper, K. S. E. Eikema, and S. Witte, *Tailoring spatial entropy in extreme ultraviolet focused beams for multispectral ptychography,* Optica. **8**(2):130-138 (2021).

3.1 Introduction

Microscopy with EUV tabletop sources is a promising diagnostic tool for nanoscience, but remains challenging due to the relatively low photon flux available as compared to large-scale facilities such as synchrotrons or free-electron lasers. In addition, focusing and shaping polychromatic EUV radiation using refractive optics such as lenses is intrinsically difficult, as most elements across the periodic table exhibit high absorption and low refractive index contrast in this spectral region. Alternative imaging approaches are therefore required. Full field tabletop EUV microscopes employ Fresnel ZPs to directly image a specimen onto a detector [47, 48]. Since the focal length of Fresnel ZPs is wavelength-dependent, EUV full field microscopes are typically restricted to monochromatic radiation. Although cascaded systems of DOEs with achromatic focusing capabilities have been reported [49, 50], a monolithic approach is preferred for EUV radiation, where phase-shifting optical elements are hard to realize and thus binary DOEs with lower diffraction efficiency have to be used [51].

The requirement for monochromaticity results in a loss of rich chemical information that can be extracted from spectrally-resolved refractive index studies [52]. A direction that has been followed more recently for EUV microscopy is coherent diffraction imaging (CDI) [53, 54], which computationally recovers specimen information from a single diffraction intensity. While this technique has been applied for EUV tabletop microscopy, it works reliably only when information about the specimen, such as finite support or sparsity [55, 56], is known *a priori*. CDI requires spatially coherent EUV radiation, which is available from table-top setups through high-harmonic generation (HHG) [57–59]. HHG sources have the additional benefit of producing extremely broad EUV and soft-X-ray spectra, making them intrinsically suited for spectrally-resolved microscopy. However, CDI requires monochromaticity, which principally limits its range of application for EUV microscopy, although some methods have been reported that relax this shortcoming through algorithmic extensions [60, 61] or experimentally via spectrally-resolved diffraction measurements [62]. Both full field microscopy and CDI have a finite field of view limitation. Attempts have been reported to extend the field of view by using a compact scanning transmission microscope (STM) based on an HHG source [63]. However, in STM the lateral resolution is directly coupled to the beam size. In addition, the results in [63] were obtained with a multilayer mirror that limited the illumination to a single harmonic. Grazing incidence mirrors may be used to focus polychromatic radiation, but these typically suffer from low numerical apertures and are sensitive to misalignment [64]. Thus all the aforementioned techniques lack spectral sensitivity and involve a compromise between field of view and resolution.

A promising technique to solve these challenges is ptychography [65, 66], a combination of STM and CDI. Ptychography enables simultaneous wavefront sensing and quantitative phase contrast microscopy at theoretically unlimited field of view [67–69]. Additionally, ptychography decouples spatial resolution from the illumination spot size. The large amount of information available in ptychography makes it possible to decode polychromatic wavefronts using only monochromatic detectors [70, 71]. This is particularly useful for EUV microscopy, where polychromatic operation offers increased flux and enables chemical sensitivity, but wavelength-resolving cameras are not available. Most HHG-based ptychography applications to date have used multilayer mirrors that filtered the source spectrum to quasi-monochromatic radiation [68, 72–76], and to our knowledge only a single result on multispectral EUV ptychography has been reported [77]. In the latter reference, the authors demonstrated the use of an ellipsoidal mirror in grazing incidence to produce a polychromatic focused beam. This approach is flux efficient, but it does not allow control over the structure of the incoming beam, which can be of great importance for reconstruction quality [78–81].

Here, we demonstrate multispectral ptychography using structured EUV beams. To this end, we address the sub-problem of designing DOEs that are suitable for both confining and structuring polychromatic EUV radiation. This goal is achieved through a novel computational design principle based on spatial entropy minimization. While the designs reported in this paper are tailored to EUV radiation, the underlying concept may be used for both refractive and diffractive optics design in other spectral domains. In the first part of the paper, we introduce spatial entropy minimization, which formulates diffractive focusing as an optimization problem. It is shown that the approach generates conventional ZPs in the limit of monochromatic radiation. A wider class of designs is examined for polychromatic radiation, with the ability to balance spectral flux. In the second part, we report experimental results for multispectral EUV ptychography, where we apply entropy optimization to generate structured and focused beams. The proposed approach paves the way for utilizing the full potential of HHG sources for spectrally-resolved EUV microscopy.

3.2 Spatial entropy minimization

Designing a multispectral ZP consists of two main ingredients, which we shortly summarize before proceeding to the mathematical formulation: First, polychromatic radiation needs to be confined into a preferably small focus. As detailed below, this constraint may be imposed by requiring the side lobes of the focal spot to decay with increasing distance from the optical axis. However, for the case of binary ZPs, we cannot prevent the presence of a zeroth order diffraction contribution. Hence, the first constraint is enforced only inside the geometrical shadow of a central stop of the ZP, which is the interior of the purple circle in Fig. 3.1. In the final experiment, portions of the beam far away from the optical axis may be clipped using an order sorting aperture (OSA) complementary to the target focal plane region to suppress the zeroth order. Second, the ZP is required to be binary. This property facilitates nanofabrication and reduces losses due to absorption when used in transmission.

With regard to the first requirement, we consider the spatial entropy functional

$$\mathcal{S}\left[\psi_k\left(\boldsymbol{x}\right)\right] = -\sum_{\boldsymbol{x}} A\left(\boldsymbol{x}\right) I\left(\boldsymbol{x}\right) \log I\left(\boldsymbol{x}\right), \tag{3.1}$$

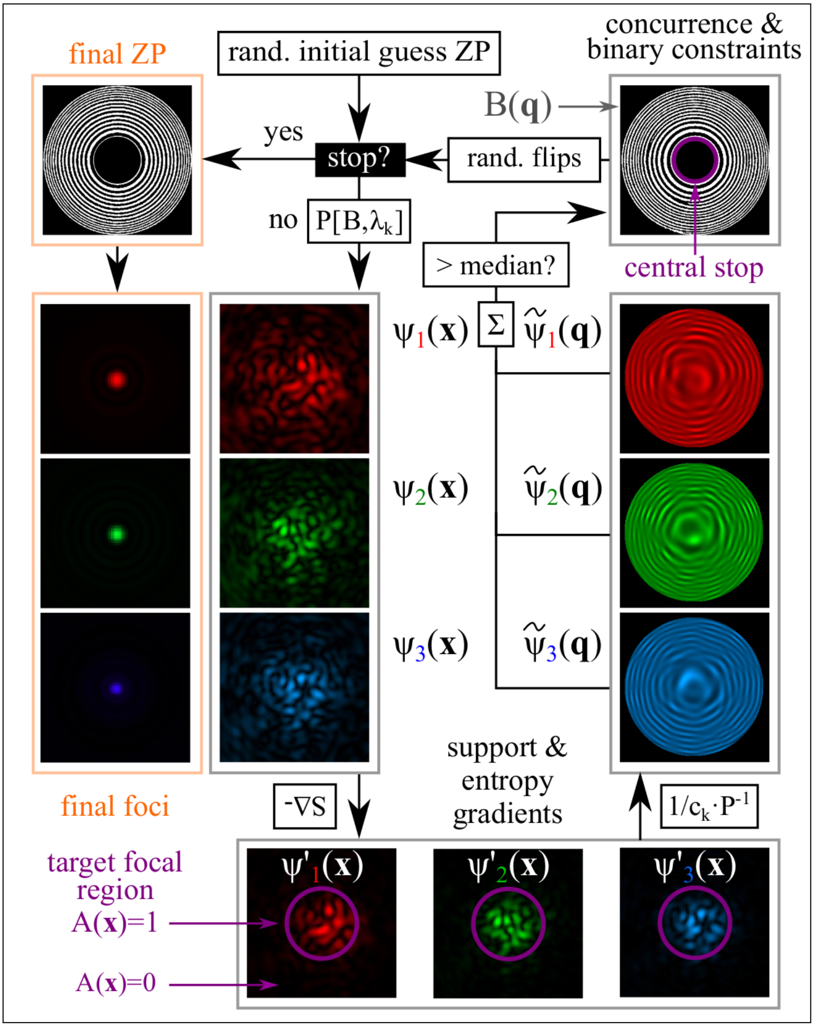

Figure 3.1: ZP optimization. Starting at a suboptimal binary ZP initial guess, the focal spot distribution for each spectral wavefront is calculated, where a gradient step towards minimum spatial entropy and support is applied. The updated beams are backpropagated into the ZP plane, where spectral holograms are combined into a single ZP via the concurrence and binary constraints. A subset of the ZP pixels are randomly flipped to prevent stagnation in local minima before the next iteration starts. The violet circles in the top and lower part of the figure depict the beam and central stop supports in the focal and ZP planes, respectively.

where the summation is over all pixels with non-zero intensity in the focal plane. We assume the focal plane intensity $I(\boldsymbol{x}) = \sum_k \psi_k^* (\boldsymbol{x}) \psi_k (\boldsymbol{x})$ to be the incoherent sum over all spectral field contributions $\psi_k (\boldsymbol{x})$ $(k = 1, \ldots, K)$ at wavelengths λ_k. The variable $\boldsymbol{x}$ denotes focal plane coordinates, and $A(\boldsymbol{x})$ is a binary function that is unity inside the geometrical shadow of the ZP central stop and zero elsewhere. Constraining the focused beam inside this finite domain in the target focal region leaves the zeroth order widely unaffected. Throughout this paper we normalize the intensity inside the focal plane,

$$\sum_{\boldsymbol{x}} A(\boldsymbol{x}) I(\boldsymbol{x}) = 1, \tag{3.2}$$

when evaluating Eq. 3.1 to make the quoted entropy values (as in Table 3.1) independent of flux. We use the natural logarithm in Eq. 3.1; any other basis scales the entropy by a constant factor and does not affect the results. With these definitions, we make three observations: (i) $\mathcal{S}$ is non-negative. (ii) Minimum entropy is achieved when the normalized total intensity (cf. Eq. 3.2) is concentrated in a single pixel, corresponding to an optimally focused beam. In this case $\mathcal{S}$=0. (iii) Maximum entropy occurs when all pixels in the target domain have equal intensity. The first and second property directly follow as a result of the normalization in Eq. 3.2 and the logarithm evaluating negative for arguments $0 < I(\boldsymbol{x}) < 1$. A proof of the third property is provided in [82]. Together, these properties motivate us to use spatial entropy as a focusing measure.

Next, we consider a strategy that minimizes the entropy functional in Eq. 3.1. The complex gradient [83] of Eq. 3.1 with respect to ψ_k is given by

$$\frac{\partial \mathcal{S}}{\partial \psi_k^* (\boldsymbol{x})} = -A(\boldsymbol{x}) \psi_k (\boldsymbol{x}) (1 + \log I(\boldsymbol{x})) . \tag{3.3}$$

We minimize Eq. 3.1 using a gradient descent iterative update

$$\psi_k' (\boldsymbol{x}) = \psi_k (\boldsymbol{x}) - \alpha \frac{\partial \mathcal{S}}{\partial \psi_k^* (\boldsymbol{x})}, \tag{3.4}$$

where the parameter α may be adjusted to control the step size along the search direction. Equation 3.4 forces the spectral beam estimates towards minimum spatial entropy inside the target focal region where $A(\boldsymbol{x}) = 1$. We refer to Eq. 3.4 as the *minimum entropy update step.*

To calculate the required ZP we define the spectrally summed hologram

$$H(\boldsymbol{q}) = \sum_k \left| \tilde{\psi}_k (\boldsymbol{q}) + \max \left| \tilde{\psi}_k (\boldsymbol{q}) \right| \right|^2, \tag{3.5}$$

where

$$\tilde{\psi}_k (\boldsymbol{q}) = \frac{1}{c_k} \mathcal{P}^{-1} \left[\psi_k' (\boldsymbol{x}), \lambda_k \right] \tag{3.6}$$

are the reweighted focal plane spectral fields backpropagated into the ZP plane with coordinates $\boldsymbol{q}$. Each $\mathcal{P}[\dots,\lambda_k]$ is a bandlimited angular spectrum propagator at the respective wavelength λ_k [84]. The weights c_k, given by

$$c_k^2 = \sum_{\boldsymbol{x}} A(\boldsymbol{x}) \left|\psi'_k(\boldsymbol{x})\right|^2 , \tag{3.7}$$

are used to equalize the relative strength of the spectral intensities in the target focal region. Other choices may be used if unbalanced spectra are desired in the focal plane. The $\max\left|\tilde{\psi}_k(\boldsymbol{q})\right|$ term in Eq. 3.5 acts as a plane holographic reference with amplitude scaled to the maximum of each respective spectral field. We want the ZP to consist of either fully transmissive or opaque features. Therefore we rewrite $H(\boldsymbol{q})$ as a binary ZP pattern according to

$$B(\boldsymbol{q}) = \begin{cases} 1, & H(\boldsymbol{q}) > \mathrm{median}\left[H(\boldsymbol{q})\right] \\ 0, & \text{else} \end{cases} . \tag{3.8}$$

The comparison with the median constrains the number of transmissive and opaque elements of the ZP to be equal. We refer to Eqs. 3.5 and 3.8 as the *concurrence* and *binary constraints*, respectively. During the search process a small subset of pixels in $B(\boldsymbol{q})$ is randomly selected and flipped from 0 to 1 and vice versa. We denote the binary ZP resulting from the latter step by $B'(\boldsymbol{q})$. The number of random flips is gradually annealed to zero (see details below). The simulations presented in the next section indicate that random flips help prevent stagnation around local minima of Eq. 3.1. As a final step, the updated focal plane spectral fields are given by

$$\psi''_k(\boldsymbol{x}) = \mathcal{P}\left[B'(\boldsymbol{q}), \lambda_k\right] . \tag{3.9}$$

After setting $\psi_k(\boldsymbol{x}) \leftarrow \psi''_k(\boldsymbol{x})$ the algorithm iterates through Eqs. 3.4 to 3.9 and stops when no progress in Eq. 3.1 is made towards lower entropy or when a predefined number of iterations is reached.

3.3 Simulation

We performed simulations of the entropy minimization algorithm proposed above and examined the influence of the source spectrum, the role of the entropy gradient, and the number of random flips following the concurrence and binary constraints. In each simulation we fixed the ZP diameter to D= 159 µm, the smallest feature size to Δx =310 nm, and the focal length to f = 4.9 mm, assuming radiation from an HHG source with a fundamental driving laser of 800 nm up-converted to the 17th to 23rd harmonic (34.8 nm to 47.1 nm). All values listed above were chosen similar to the experimental parameters below. We note that the feature size is defined here as the smallest spatial scale over which the ZP can switch from opaque to transmissive and vice versa. The bandlimited angular spectrum propagator $\mathcal{P}$ assumes the same pixel size in the zone plate and focal

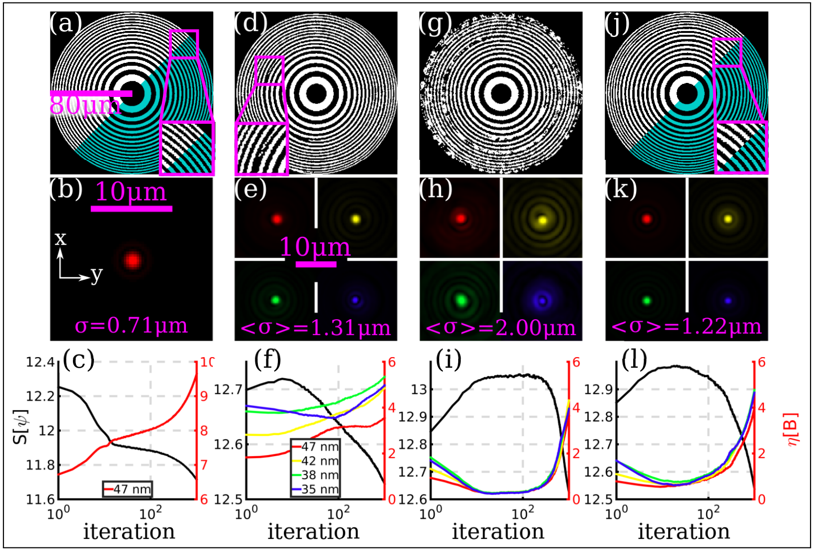

Figure 3.2: Simulated ZP designs. (a) Monochromatic spatial entropy minimization zone plate estimate. The violet inset in (a) indicates a match out to the smallest zones between the optimized ZP (white) and a conventional ZP with fitted parameters (turquoise). (b) Monochromatic focal plane intensity cross-section corresponding to the ZP estimate in (a). (c) Entropy (black) and efficiency (red) versus iteration (1000 iterations, logarithmic scale). (d) Optimization result for multicolor ZP with a small percentage (5%) of random flips. (e) Focal plane intensity cross sections for four different harmonic wavelengths. (f) Entropy (black) and efficiency for all four wavelengths. (g-i) Multicolor ZP with 25% of random flips and entropy gradient switched off. (j-l) Multicolor ZP with 25% of random flips and entropy gradient switched on. The solution in (j) cannot be fit to a conventional ZP. In the bottom row we compare the focal plane entropy (black line, left vertical axis) and the focal plane beam spectral efficiencies (colored lines, right vertical axis) for each respective ZP. The scale bars are shared throughout each row. The parameters for this simulation are summarized in Table 3.1.

plane. All simulations below are performed with

$$A\left(\boldsymbol{x}\right)=\begin{cases}1, & \left\|\boldsymbol{x}\right\|<5um\\ 0, & \text{else}\end{cases} \tag{3.10}$$

and $\alpha = 0.25$ (compare Eq. 3.4). The spectral beam size σ_k is defined here via the truncated second moment

$$\sigma_k^2=\frac{\sum_{\boldsymbol{x}}\boldsymbol{x}^2 A\left(\boldsymbol{x}\right)\left|\psi_k\left(\boldsymbol{x}\right)\right|^2}{\sum_{\boldsymbol{x}} A\left(\boldsymbol{x}\right)\left|\psi_k\left(\boldsymbol{x}\right)\right|^2}, \tag{3.11}$$

where $A\left(\boldsymbol{x}\right)$ is used to mask out zero-order contributions beyond the target focal region. The average beam size is the arithmetic mean over all spectral beam sizes in the focal plane

$$\langle\sigma\rangle = \frac{1}{\Lambda}\sum_{k}\sigma_k, \tag{3.12}$$

where Λ is the number of spectral lines. The spectral efficiency is defined here as the ratio of the energy in the target focal region divided by the energy incident on the circular area containing the ZP, evaluated separately at each wavelength λ_k,

$$\eta_k\left[B\right] = \frac{4}{\pi D^2}\sum_{\boldsymbol{x}} A\left(\boldsymbol{x}\right)\left|\psi_k\left(\boldsymbol{x}\right)\right|^2 \Delta x^2, \tag{3.13}$$

where D is the ZP diameter and we assume the ZP is illuminated by a plane wave of unit intensity at every pixel and wavelength.

panel	$\langle\eta\rangle$	S_{final}	λ [nm]	% rand. flips	∇S
(a-c)	9.65%	11.71	47.1	25% - 0%	✓
(d-f)	4.68%	12.54	34.8 - 47.1	5% - 0%	✓
(g-i)	3.96%	12.63	34.8 - 47.1	25% - 0%	
(j-l)	4.54%	12.53	34.8 - 47.1	25% - 0%	✓

Table 3.1: Simulation parameters for the ZP optimization results in Fig. 3.2. For each ZP we show the average spectral efficiency, the final spatial entropy, wavelength range, percentrage of random flips during annealing, and whether or not the entropy gradient was applied in the focal plane.

Figure 3.2(a) shows in the upper left corner the entropy minimization result (white) for only the 17th harmonic present in the spectrum incident on the ZP. The fraction of random flips in the allowed ZP area, limited by the fixed ZP diameter and the central stop, was linearly annealed from 25% to 0% within a total of 1000 iterations. A standard ZP characterized by two parameters, namely the wavenumber κ and a constant phase offset ϕ, was fit to the output of the entropy minimization algorithm by solving the nonlinear least squares problem

$$\underset{\kappa,\,\phi}{\operatorname{argmin}}\sum_{\boldsymbol{q}} w\left(\boldsymbol{q}\right)\left(B\left(\boldsymbol{q}\right) - \operatorname{sgn}\left[\cos\left(\kappa\sqrt{f+\boldsymbol{q}^2}+\phi\right)\right]\right)^2. \tag{3.14}$$

For the simulations in this section the weighting function $w\left(\boldsymbol{x}\right)$ is given by

$$w\left(\boldsymbol{q}\right) = \begin{cases} 1, & 10\ \mu m < \|\boldsymbol{q}\| < 79.5\ \mu m \\ 0, & \text{else} \end{cases} \tag{3.15}$$

to account only for the pixels inside the outer diameter (159 µm) and outside the central stop diameter (20 µm) of the ZP. We note that the central stop diameter is chosen larger than the target focal plane diameter (10 µm) to reduce the contribution of the zeroth order in the target focal plane. The ZP fit to the output of the monochromatic minimum entropy ZP is shown in the lower right corner (turquoise) of Fig. 3.2(a), where the violet inset highlights the match for the outermost zones. Here the fitting parameters are $\kappa = 0.1335$ nm^{-1} and $\phi = 0.5587$ rad. A lateral cross-section of the focused beam in the target focal plane is shown in Fig. 3.2(b). Here, and in all other panels in the middle and bottom rows of Fig. 3.2, the colorcoding indicates the wavelengths from long to short, namely: red (17th harmonic, $\lambda_1 = 47.1$ nm), yellow (19th harmonic, $\lambda_2 = 42.1$ nm), green (21st harmonic, $\lambda_3 = 38.1$ nm), and blue (23rd harmonic, $\lambda_4 = 34.8$ nm). The monochromatic and average beam sizes are indicated by σ and $< \sigma >$, respectively, according to Eqs. 3.11 and 3.12. In Fig. 3.2(c), we plot the evolution of the spatial entropy functional $\mathcal{S}\left[\psi_k\right]$ of the beam in the focal plane (black, left vertical axis) and the spectral efficiency $\eta_k\left[B\right]$ (red, right vertical axis) of the ZP design versus iteration number. The minimum entropy solution for the monochromatic case results in a conventional binary ZP reaching a final efficiency of 9.65%. Due to losses introduced by the central stop [81], this is slightly lower than the theoretical maximum for a conventional, binary ZP of $1/\pi^2 \approx 10.13\%$ [51]. We conclude that our entropy minimization approach results in conventional ZPs for monochromatic radiation. In Fig. 3.2(d-f) we assumed all four harmonics (17th to 23rd) to be present in the incident beam. We first study the role of the number of random flips in the design. Here the fraction of random flips in the allowed ZP area was linearly annealed from 5% to 0% within 1000 iterations, instead of 25% to 0% as done in all other simulations reported in this section. Similar to the monochromatic case, Fig. 3.2(f) shows the efficiencies of the spectral intensities (red, yellow, green, and blue; y-axis on the right) increase as the spatial entropy (black; left y-axis) is minimized. The formation of asymmetries, such as pitchfork-shaped bifurcations in Fig. 3.2(d) suggests the algorithm found a sub-optimal result, as there should not be a preferred direction in the solution of the problem. The individual spectral efficiencies in the target focal region are found to be $\eta_1 = 3.55\%$, $\eta_2 = 4.85\%$, $\eta_3 = 5.34\%$, $\eta_4 = 4.98\%$, resulting in an average spectral efficiency of ($\langle\eta\rangle = 4.68\%$).

In Fig. 3.2(g-i) we investigated the effect of not making use of the entropy gradient and only imposing a support constraint, pushing the tails of the focal plane spectral beams to zero outside the target region. This is achieved by neglecting the log-term in Eq. 3.3. In this case, the algorithm settled for a sub-optimal result, qualitatively indicated by the large number of asymmetries in both the final ZP (Fig. 3.2(g)) and the focal plane beam intensities (Fig. 3.2(h)), and quantitatively expressed by the lower average spectral efficiency ($\langle\eta\rangle = 3.96\%$) in Fig. 3.2(i) as compared to the previous and following case. This underlines the importance of the entropy gradient in finding a ZP for multispectral operation. In Fig. 3.2(j-l) we repeated the simulation with identical parameters as Fig. 3.2(d-f) but annealed the fraction of random flips in the ZP from initially 25% to a final of 0%. In this case a highly symmetric solution was found which resulted in the lowest spatial entropy in the focal plane among the polychromatic cases tested (see supplementary media). This shows that the number of random flips is crucial in allowing the algorithm to escape local minima in the entropy functional. We attempted to fit a conventional ZP (turquoise in Fig. 3.2(j) to the output (white) of the entropy minimization algorithm for the polychromatic focusing problem (best fit parameters: $\kappa = 0.1655$ nm^{-1} and $\phi = 3.4795$ rad.). The mismatch in the violet inset shows that the aforementioned parameters cannot model the output of the ZP estimate for the polychromatic focusing problem Fig. 3.2(j), in contrast to the ZP estimate for the monochromatic focusing problem in Fig. 3.2(a). The conventional ZP fit (turquoise) yields highly unbalanced spectral efficiencies $\eta_1 = 0.90\%$, $\eta_2 = 3.96\%$, $\eta_3 = 9.77\%$, $\eta_4 = 6.96\%$ ($\langle\eta\rangle = 5.39\%$). Although the average efficiency performs better than our entropy minimization designs, the efficiencies in the target focal region for the 17th and 21st harmonics are an order of magnitude apart, rendering conventional ZPs poor candidates for multispectral operation. In contrast, the result of our entropy minimization algorithm exhibits a good balance in the spectral efficiencies $\eta_1 = 3.98\%$, $\eta_2 = 4.73\%$, $\eta_3 = 4.77\%$, $\eta_4 = 4.65\%$ ($\langle\eta\rangle = 4.54\%$), making them more applicable for operation at multiple wavelengths than conventional ZPs. The most relevant parameters of the simulations in this section are summarized in Table 3.1.

Further insight into the flux balancing mechanism provided by entropy minimization is obtained by examining the resulting axial beam cross sections around the focal plane. In Fig. 3.3 we compare axial beam cross sections obtained from the conventional ZP in Fig. 3.2(a) and the minimum entropy ZP in Fig. 3.2(j), both in polychromatic operation. The left column of Fig. 3.3 shows the focusing behavior of the conventional ZP. It is seen that a wavelength shift causes an axial displacement of the focal plane. This axial displacement is an immediate consequence of the exchangeable roles that the wavelength and the propagation distance play in paraxial diffraction [85]. The flux in a single observation plane (semi-transparent line) is widely unbalanced as a result of the beam being dominated by a single diffraction order. The right column of Fig. 3.3 shows the focusing behavior of the ZP optimized for minimum entropy from Fig. 3.2(j). It is seen that the entropy minimization approach yields multiple and more balanced diffraction orders as compared to the conventional ZP. Changing the wavelength results in an axial displacement of the minimum entropy beam. However, for the minimum entropy beam the diffraction orders coincide upon axial displacement, in contrast to the beam generated from the conventional ZP. We conclude that entropy minimization achieves flux balancing through axial alignment of higher diffraction orders.

Two final notes concern the uniqueness of the simulation results and computational complexity: First, we have constrained the algorithm to focus into a relatively large target focal region with a diameter of 10 µm. However, the entropy minimization algorithm gives a solution with significantly smaller beam size. If the target focal region is constrained to be circular as given in Eq. 3.10, the entropy functional in Eq. 3.1 is invariant under translation of the focal spot intensity and the solution is non-unique. In particular, this can result in ZPs with off-axis focus. Practically, we omitted this by choosing a smooth apodization function

$$A\left(\boldsymbol{x}\right) = e^{\left(-\frac{\boldsymbol{x}^2}{2\sigma^2}\right)} \tag{3.16}$$

with a full width at half maximum of $\mathrm{FWHM} = 2\sqrt{2\ln\left(2\right)}\sigma = 10\,\mu\mathrm{m}$. This was used only for the entropy update step (Eq. 3.4) while the renormalization step

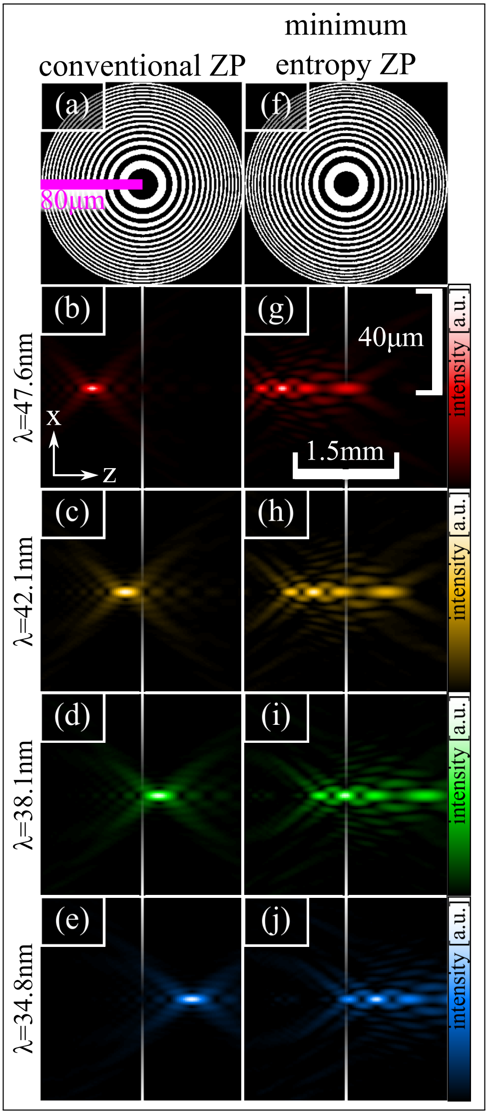

Figure 3.3: Simulated axial cross sections of conventional (left) and minimum entropy (right) ZPs. Conventional ZPs concentrate most flux into a single diffraction order while minimum entropy ZPs distribute the flux among multiple orders. In both cases wavelength modifications cause an axial displacement of the beam around the focal plane. In contrast to conventional ZPs, the minimum entropy ZP exhibits balanced diffraction orders which coincide upon axial displacement. In panels (b)-(e) and (g)-(j) the semi-transparent lines serve as reference to compare the axial location of the diffraction orders.

(Eq. 3.7) and the evaluation of spectral efficiency (Eq. 3.13) used the circular apodization function described by Eq. 3.10. Second, the computational complexity of a single iteration of the entropy minimization algorithm scales with $\mathcal{O}\left[\Lambda \cdot P \cdot \log P\right]$, where P is the total number of pixels in the ZP. Each ZP optimization described in this section ($P = 2^{20}$, $\lambda = 4$, 10^3 iterations) required 160 s using GPU-accelerated computation on a NVIDIA Tesla K40 and a MATLAB software implementation.

3.4 Multispectral ptychography

3.4.1 Forward model

All results reported in this chapter are based on ptychographic information multiplexing [70], which models the observed intensity on the monochromatic detector as an incoherent sum of multiple monochromatic diffraction patterns. We minimize the difference between the observed intensity $I_t(\boldsymbol{u})$ and the estimated summed spectral density S with respect to both the estimated probe $P\left(\boldsymbol{x}, \lambda\right)$ and the estimated object transmission function $O(\boldsymbol{x})$, i.e.

$$\underset{P(\boldsymbol{x},\lambda_k),\, O(\boldsymbol{x})}{\operatorname{argmin}} \sum_{\boldsymbol{t}} \sum_{\boldsymbol{u}} \left| I_{\boldsymbol{t}}\left(\boldsymbol{u}\right) - \sum_{k} M_{\boldsymbol{t}}\left(\boldsymbol{u}, \lambda_k\right) \right|^2 , \tag{3.17}$$

where $\boldsymbol{x}$ and $\boldsymbol{u}$ denote object and detector coordinates, respectively, and $\boldsymbol{t}$ is a lateral translation vector indicating scan position. The sample exit wave is related to the modeled spectral density through

$$M_{\boldsymbol{t}}\left(\boldsymbol{u}, \lambda_k\right) = \left|\mathcal{D}\left[P\left(\boldsymbol{x}\right) O\left(\boldsymbol{x} - \boldsymbol{t}\right), \lambda_k\right]\right|^2 , \tag{3.18}$$

where $\mathcal{D}$ is a two-step Fresnel propagator that allows to scale the real-space coordinates to the same pixel size for all wavelengths [86] (see subsection 3.4.2). An accelerated gradient optimizer is used to minimize Eq. 3.17 [87]. We note that in Eq. 3.18 the object is modeled as non-dispersive. It is possible to use a more general model where the complex amplitude transmission function changes with wavelength [70].

3.4.2 Multistep-propagation

In typical far-field and Fresnel ptychographic configurations the object pixel size is given by $\Delta x = \lambda z / D$, where z is the sample-detector distance and D is the detector size. Thus the pixel size scales with the wavelength of the probe. To prevent different pixel sizes for each wavelength-dependent probe and object estimate, several strategies have been proposed. One solution is to use zero padding of the detector array to a larger size, to keep the object pixel size constant as the wavelength increases [88]. This strategy has the drawback that the spectral illumination estimates $P\left(\boldsymbol{x}, \lambda\right)$ have varying number of pixels. Another approach is to accept the reconstruction pixel size to be different and, if necessary, interpolate the spectral object reconstructions to the same pixel sizes to overlay them [70]. Our approach is to use a two-step propagator, which first propagates the exit wave into an intermediate plane using an angular spectrum propagator (ASPW) with fixed pixel size and subsequently uses a Fresnel propagator describing diffraction from the intermediate plane to the detector [85, 86]. This is illustrated in Fig. 3.4. The location of the intermediate plane is selected such that the pixel size between all spectral reconstructions is the same. While the two-step approach has the drawback that it requires multiple Fourier transforms to compute the propagation between the sample and the detector, it enables imposing constraints between the spectral reconstructions (see subsection 3.4.3).

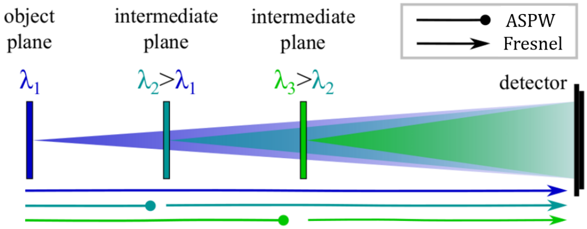

Figure 3.4: A two-step propagation scheme is used to scale the pixel size of each spectral reconstruction to be the same. The spectral wave emanating from the sample at the lowest wavelength λ_1 is directly propagated into the detector plane via Fresnel propagation. All other spectral waves are first propagated to intermediate planes using an angular propagator. In a second step each spectral exit waves is propagated from its respective intermediate plane to the detector.

3.4.3 Regularization

Several simplifications to the model in Eq. 3.17 can be made, to reduce the number of unknowns and render the inverse problem more constrained. If the object transmission changes slowly as a function of wavelength, the spectral estimates can be coupled via a spectral smoothness prior. Let $O(\boldsymbol{x}, \lambda_k)$, $k = 1, \ldots, K$, describe the spectral object transmissivity at wavelength λ_k. We impose spectral smoothness via the relaxation

$$O(\boldsymbol{x}, \lambda_k) \leftarrow (1-\alpha) O(\boldsymbol{x}, \lambda_k) + \alpha \frac{O(\boldsymbol{x}, \lambda_{k-1}) + O(\boldsymbol{x}, \lambda_{k+1})}{2}, \tag{3.19}$$

for $k = 2, \ldots K-1$, and

$$O(\boldsymbol{x}, \lambda_{1,K}) \leftarrow (1-\alpha) O(\boldsymbol{x}, \lambda_{1,K}) + \alpha O(\boldsymbol{x}, \lambda_{2,K-1}) \tag{3.20}$$

at the boundaries ($k = 1, K$) of the spectral domain. In words, the object estimate is weakly constrained to be the average of neighboring spectral reconstructions. At the boundaries the lowest spectral object estimate is coupled to the subsequent estimate, while the highest spectral object estimate is coupled only to the previous estimate. The parameter α can be chosen constant or scheduled decaying with increasing iteration. We refer to Eqns. 3.19 and 3.20 as *spectral smoothness*. If the object is not dispersive, such as binary objects, the model simplifies further and we may assume the same spectral object transmissivity at each given wavelength.

3.5 Polychromatic ptychography with structured illumination

To verify the polychromatic ptychography approach, we constructed a NIR test setup that enables a comparison to results obtained with monochromatic light. The ability to compare monochromatic and polychromatic reconstructions is more challenging for HHG radiation as it requires controllable spectral filtering. In addition, we compare the reconstruction quality for smooth versus structured beams.

3.5.1 NIR setup

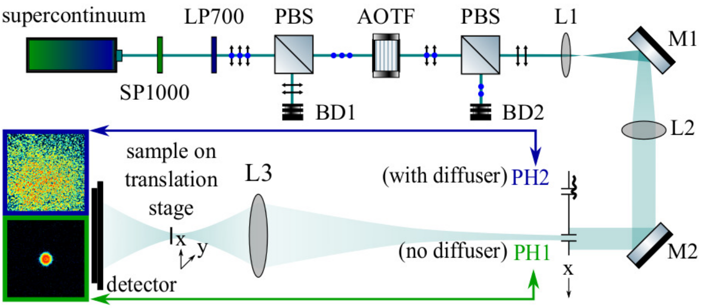

Figure 3.5: NIR experimental setup. A supercontinuum laser is spectrally limited via short (SP1000) and long pass (LP700) filters. Linearly polarized, mono- and polychromatic beams can be selected using a combination of polarizing beam splitters (PBS) and an AOTF. The beam is expanded through lenses L1 and L2. Pinholes (PH) with approximately equal area are imaged onto the specimen. PH1 is empty and PH2 contains a lens paper diffuser. Translating the specimen transversely and recording the resulting diffraction intensities gives the input data for the ptychographic analysis.

Our NIR setup is shown is Fig. 3.5. A supercontinuum source (NKT Photonics whitelase, 400 nm to 2000 nm, output power 200 mW) is spectrally limited by the use of two successive edgepass filters (Thorlabs LP700 and SP1000) to the range 700 nm to 1000 nm. An acousto-optic tunable filter (AOTF, Gooch & Housego, TF950-500-1-2-GH96) selects up to seven multiplexed quasi-monochromatic spectral lines (bandwidth 0.6 nm, $\lambda/\Delta\lambda > 1000$). In the experiments below the spectral line is selected to give an approximately equal flux on the detector in the absence of a specimen. Polarizing beam splitters (PBS) are used to feed a linearly polarized beam into the AOTF and to select the first diffraction order downstream the AOTF. After expanding the beam by means of two lenses L1 (f_1 = 25 mm) and L2 (f_2 = 300 mm), two pinholes (PH) can be selected to modulate the incoming beam. PH1 is a pinhole with an empty, transmissive area. PH2 has a lens paper diffuser stuck on top. The specimen is mounted on an encoded xy-translation stage (2x Smaract SLC-1770-D-S, 46 mm travel range, 70 nm repeatability). A CCD camera (AVT prosilica GX1920, 14 bit, pixel size 4.54 µm) records diffraction intensities for each specimen translation position. The sample-detector distance is 26.5 mm.

3.5.2 Structured versus smooth illumination in monochromatic ptychography

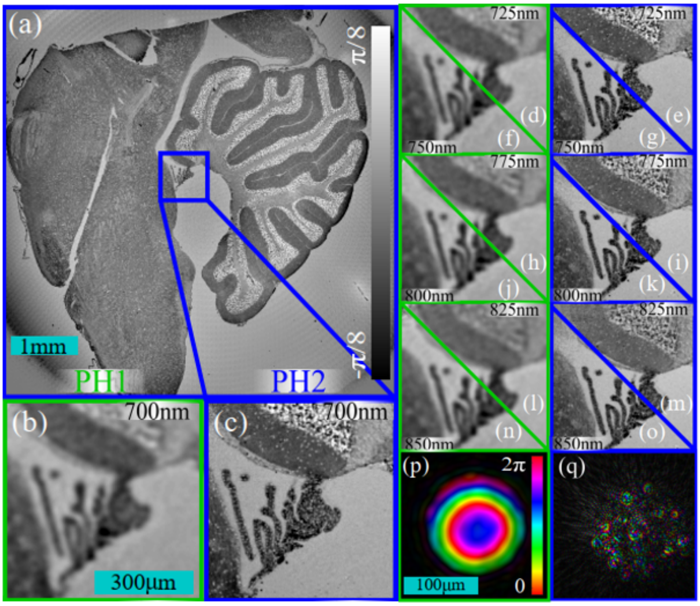

Figure 3.6: (a) Whole-slide ptychographic reconstruction of mouse brain in phase contrast at λ = 700 nm. (b-o) The insets compare at-wavelength phase reconstructions using a smooth beam (green) as compared to a structured beam (blue). (p,q) Smooth and structured beam reconstruction for PH1 and PH2, respectively, at λ = 700 nm.

We collected quasi-monochromatic ptychography scans in the wavelength range from λ_{min} = 700 nm to λ_{max} = 850 nm in $\Delta\lambda$ = 25 nm steps for both PH1 and PH2. For both pinholes we scanned the object over small and large field of views (FOVs) with diameters of 1.5 mm (250 scan positions) and 7 mm (6250 scan positions), respectively. The ptychographic reconstruction results are shown in Fig. 3.6. Fig. 3.6(a) shows a ptychographic phase reconstruction of a stained mouse brain over a large field of view (7 mm × 7 mm). A structured beam produced by PH2 was used for this reconstruction. Fig. 3.6(b-o) show phase reconstructions obtained from the smaller FOV at each wavelength and for both illumination with a smooth beam (PH1, left) and with a structured beam (PH2, right). The data was acquired such that for each wavelength the number of counts recorded on the detector pixel with highest exposure was approximately 2000 both for the smooth and the structured illumination scans. It is evident that the object reconstruction quality in the case of the structured beam is superior to that of the smooth beam. This can be explained by the significantly different total flux recorded on the detector for the two different beams. While the smooth beam yields detector signals where most of the photons are recorded in the center of the diffraction pattern, effectively acting as a low-pass spatial filter, the structured beam distributes the photons over the entire detector area and thereby allows to collect more photons within a single acquisition. This is seen in Fig. 3.5 to the left of the detector, where we show two experimentally measured diffraction intensities that were obtained with the smooth and structured beam as produced by PH1 and PH2, respectively. Fixing the maximum flux per pixel instead of the total flux recorded over the entire detector is a fair comparison when not allowing for multiple exposures. It is therefore desirable to record each diffraction pattern in a single exposure with as many photons as possible distributed over the detector area, which is achieved by the structured beam. It is noted that structured beams lead to superior reconstruction quality as compared to smooth beams even when fixing the total photon budget over the entire detector [79].

3.5.3 Structured versus smooth illumination in multispectral ptychography

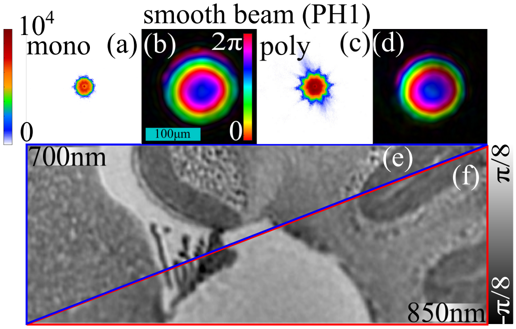

Figure 3.7: (a,c) Averaged diffraction pattern for mono- (b) and polychromatic smooth beam (d) at a wavelength of 700 nm. The scalebar in (a) shows the total number of photoelectron counts. The diffraction patterns displayed in (a) and (c) are recorded with the same integration time of 1 ms. (e,f) Object phase reconstruction from polychromatic data set for smooth beam at a wavelength 700 nm and 850 nm, respectively.

The experiments described in the previous subsection were repeated with polychromatic radiation consisting of seven equispaced spectral lines in the range

700 nm to 850 nm. In contrast to the previous section, where each scan was carried out with monochromatic light, in this section all beams are multiplexed. The results of these experiments are shown in Fig. 3.7. Figures 3.7(a,c) show mono- and polychromatic diffraction patterns averaged over all scan positions and using a smooth beam profile produced by PH1. The corresponding mono- and polychromatic beam reconstructions are shown in Fig. 3.7(b,d), respectively, at a wavelength of 700 nm. Two out of a total of seven object phase reconstructions are shown in Fig. 3.7(e,f) at wavelengths of 700 nm and 850 nm, respectively. As in the monochromatic case, the object phase reconstructions appear blurred due to the predominantly low scattering angles collected by the detector.

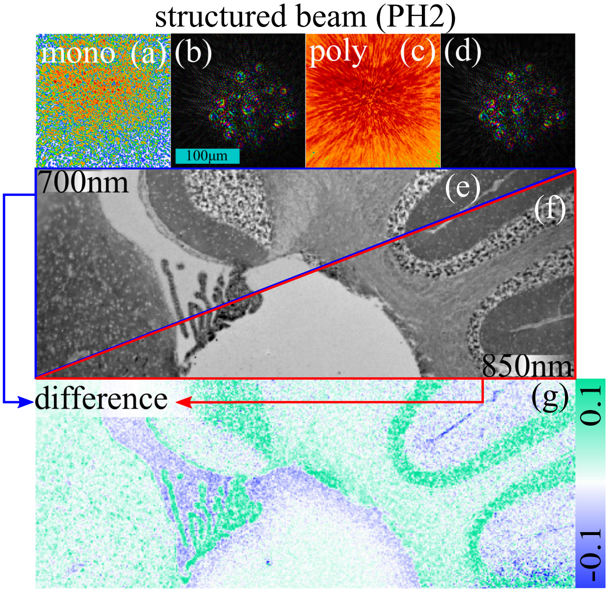

Figure 3.8: (a,c) Diffraction pattern for mono- (b) and polychromatic structured beam (d). Only the reconstructed beams at $\lambda = 700$ nm wavelength are shown. The diffraction patterns displayed in (a) and (c) are recorded with the same integration time of 100 ms. (e,f) Object phase reconstruction from polychromatic data set for structured beam at $700nm$ and 850 nm, respectively. (k) Difference between (e) and (f). Panels (a) to (f) use the same colorbars as in Fig. 3.7.

The polychromatic reconstruction results for the structured beam from PH2 are shown in Fig. 3.8. In Fig. 3.8(a,c) the diffraction patterns averaged over all all scan positions are shown for monochromatic (700 nm) and polychromatic illumination (700 nm - 850 nm). Note the radial structure in Fig. 3.8(c), which is characteristic for polychromatic speckle [89]. The corresponding mono- and polychromatic beam reconstructions are shown in Fig. 3.8(b,d), respectively, at a wavelength of 700 nm. It is seen that the mono- and polychromatic beam reconstructions are consistent despite the presence of multiple wavelengths in the latter. The object phase reconstruction for the structured beam illumination is shown in Fig. 3.8(e,f). Similar to the monochromatic results in Fig. 3.6, the polychromatic reconstructions also show a drastically improved lateral resolution when using structured beam illumination (Fig. 3.8(e,f)) compared to the smooth beam (Fig. 3.7(e,f)).

As explained above, this is the result of improved availability of information at larger scattering angles. In Fig. 3.8(g) we show the mean subtracted difference between the object phase reconstructions at 700 nm and 850 nm revealing different relative phase shifts mostly in the granular layer. This spectral contrast may be used for segmentation applications or to extract quantitative optical tissue properties over an extended wavelength range [90].

3.6 Experimental results

3.6.1 Zone plate design considerations for EUV ptychography

In this section we summarize considerations to match free parameters in the minimum entropy ZP design for operation in our EUV ptychography setup. We start with the diameter of the target focal plane. While the object field of view in monochromatic far-field ptychography is theoretically unlimited through transverse scanning, the probe field of view (pFOV) is restricted by the experimental geometry,

$$\mathrm{pFOV} = \frac{\lambda z}{b \Delta u}, \tag{3.21}$$

where Δu is the detector pixel size, b is the binning factor, and z is the sample-detector distance [85]. In polychromatic ptychography Eq. 3.21 is a function of wavelength, with the most restricted pFOV found at the minimum wavelength in the probe spectrum. Under optimized conditions for HHG in Argon using an 800 nm driving laser, our source provides appreciable flux down to $\lambda_{\mathrm{min}} = 25$ nm. For a sample-detector distance of $z = 90$ mm, dictated by the geometry of our experimental vacuum chamber, and a binning factor of $b = 4$ (to reduce the computational overhead of the Fourier transforms involved in the multispectral ptychography solver, see subsection 3.6.4 below), this results in a minimum pFOV of 41.6 µm. We achieve an oversampling ratio better than 2 per dimension [91] by restricting the target focal region to 15 µm.

Another important consideration is the desired beam shape. We demonstrated above that minimum entropy ZPs can be designed for multispectral operation. However, they are not necessarily optimal for ptychography, which benefits from spatially extended and structured beams [78–81]. While this has previously been shown for monochromatic radiation, the same observation holds for polychromatic ptychography (see section 3.5). We thus decided to find a compromise between the need for probe localization as dictated by Eq. 3.21 (which is achieved by entropy minimization) and introducing spectrally-dependent spatial structure into the polychromatic wavefront. Revisiting the simulation results in Fig. 3.2(d-f) and the corresponding row in Table 3.1, we see that aberrations caused by the presence of bifurcations in the ZP design can introduce structure into the illumination while still providing a fair balance between the energy of each spectral field in the focal plane [81]. Our final ZP design was optimized using entropy minimization for six harmonics (17th to 27th order) simultaneously. We note that annealing with only 0.5%-0% random flips was used to promote the formation of bifurcations in the ZP, while searching for a solution with low entropy. Based on this a ZP was manufactured with additional support structure as shown in Fig. 3.9(a). The ZP has an outer diameter of 240 µm, a smallest feature size of 155 nm, and a focal distance of 4.2 mm. A central stop with a diameter of 75 µm was left opaque. This region can be used in conjunction with an order-sorting aperture of the same size to block the undiffracted portion of the radiation transmitted through the ZP. Our simulations indicate that the ZP has an estimated average spectral efficiency of better than 3%.

3.6.2 Nanofabrication

The multicolor binary ZP as described in the previous subsection was fabricated on a 90 nm thick Au layer sputter coated on a 50 nm thick Si_3N_4 membrane (Ted Pella Inc.). The pattern was milled with a 30 keV focused gallium ion-beam (FEI Helios Nanolab 600). The ion-beam current was set to 48 pA with a focal spot diameter of 50 nm. The ZP was milled in 12 cycles with a sputter step size of 35 nm and dwell time of 60 ms. The total time required for nanofabrication was approximately 6 hours. In addition, we fabricated a binary sample for wavefront analysis of the multispectral wavefront produced by the ZP. Periodic structures were initially taken into consideration. However, periodic samples are not ideal for ptychography, as they give rise to localized diffraction peaks. These saturate a few detector pixels quickly while leaving others at a low level of exposure, allowing only a small total number of photons to be recorded. Moreover, self-calibration methods such as lateral position correction are challenging [93]. Hence we designed a sample (see Fig. 3.9(d) left side) that is aperiodic upon lateral translation. An analytical expression for the sample transmission function is given by

$$O(\rho,\theta) = \frac{1}{2}\left(1 + \operatorname{sgn}\left[\sin\left(a\theta + 2\pi\left(\frac{\rho}{b}\right)^2\right)\right]\right) t(\rho), \tag{3.22}$$

where (ρ,θ) are polar coordinates,

$$t(\rho) = \operatorname{rect}\left(\frac{\rho}{d_1}\right) \cdot \left[1 - \operatorname{rect}\left(\frac{\rho}{d_2}\right)\right] + \operatorname{rect}\left(\frac{\rho}{d_3}\right), \tag{3.23}$$

and

$$\operatorname{rect}(\rho) = \begin{cases} 1, & \rho \leq 1/2 \\ 0, & \text{else} \end{cases} \tag{3.24}$$

$t(\rho)$ is an apodization function that guarantees each spectral wavefront downstream of the sample is oversampled according to Eq. 3.21. This is a useful property when reconstructing strongly defocused beams. The free parameters in

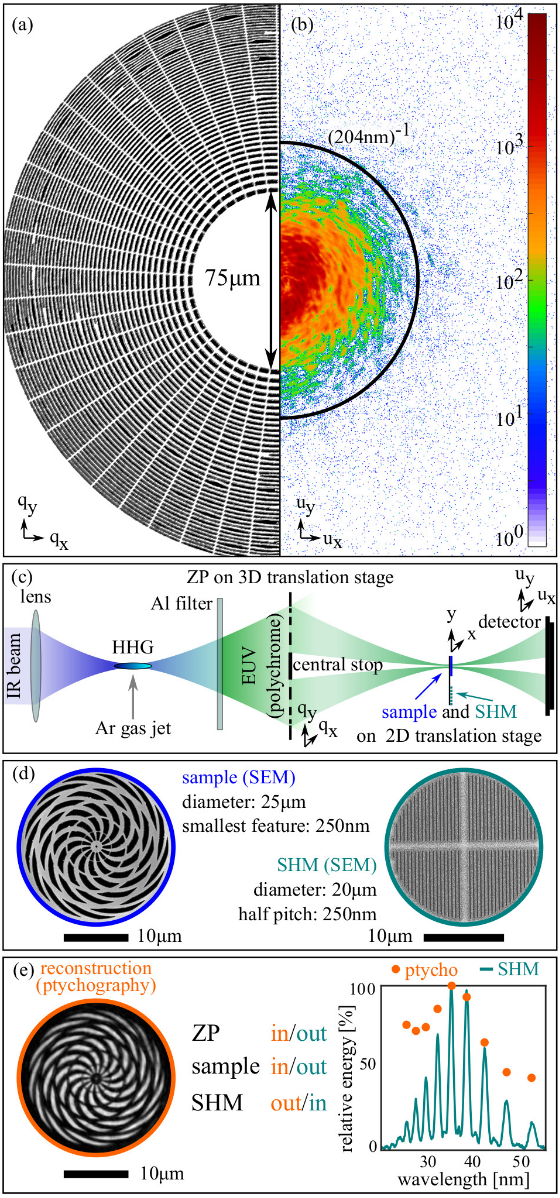

Figure 3.9: (a) SEM image of ZP. (b) Experimental diffraction pattern produced by illuminating the sample shown in (d) using the ZP shown in (a). (c) Experimental setup. A fundamental infrared (IR) beam is focused into an Argon (Ar) gas jet resulting in high-harmonic generation (HHG). After the IR beam (blue) is blocked by an aluminium (Al) filter, a binary ZP focuses the polychromatic EUV (green) beam onto a sample (d) mounted on a translation stage. A spectral Hartmann mask (SHM) [92], consisting of 21 grating-apertures as the one shown in (d), can be moved into the beam with the ZP removed to identify the spectral lines in the HHG spectrum (see panel e). (e) ptychographic reconstruction of sample (left) and reconstructed (orange) versus measured (turquoise) spectrum (right).

the first term in Eq. 3.22 allow to control the number ($a = 13$) and the curvature of the spokes ($b = 5$ µm). The free parameters in the apodization function control the outer (d_1) and inner diameter (d_2) of the object. Stabilizing support rings and a dot were added at the center with a diameter (d_3) close to the lateral resolution limit at the central wavelength our ptychography setup (124 nm full period at 32 nm). These parameters were chosen as $d_1 = 25$ µm, $d_2 = 2$ µm, $d_3 = 250$ nm. An SEM image of the final sample is shown in Fig. 3.9(d).

3.6.3 Experimental setup

The EUV measurements have been carried out using a table-top HHG source. A non-collinear optical chirped-pulse amplifier system amplifies infrared pulses with a central wavelength of 800 nm generated by a Ti:sapphire oscillator. This system delivers driving pulses with a duration of 25 fs at a repetition rate of 300 Hz. A pulse energy of 2 mJ is typically used for HHG. These pulses are focused into an Argon (Ar) gas jet and are up-converted to EUV wavelengths through the HHG process as illustrated in Fig. 3.9(c). An aluminum (Al) membrane with a thickness of 200 nm is used to filter out the fundamental beam while the HHG beam is transmitted. This EUV beam is focused by the ZP onto a sample which is mounted on a two-dimensional translation stage (Smaract SLC-1730) required to perform ptychography scans. In addition, a spectral Hartmann mask (SHM) is mounted next to the sample [92]. The SHM consists of multiple apertures with gratings inscribed, one of which is shown in Fig. 3.9(d). We note that the SHM cannot be used for wavefront sensing on focused beams and is used here only for the characterization of the HHG spectrum with the ZP removed from the beam path. The identified spectral lines, but not their relative weights, are used in the ptychography algorithm below as prior knowledge. Finally a CCD camera (Andor Ikon-L 936 SO, 2048x2048 pixels, pixel size 13.5 µm) collects diffraction patterns at a distance of 92.5 mm downstream of the specimen and SHM. A typical multi-wavelength HHG diffraction pattern with the described setup is shown in Fig. 3.9(b).

3.6.4 Ptychography scan

Our reconstruction algorithm is based on ptychographic information multiplexing [70], which models the observed intensity on the monochromatic detector as an incoherent sum of multiple monochromatic diffraction patterns. All algorithmic details are given in the supplementary information. We collected a ptychographic scan consisting of 252 scan positions covering a field of view with a diameter of 50 µm. The average scan step was 2.5 µm and the diameter of the binary object is 25 µm, resulting in a linear overlap of approximately 90% [94]. This relatively high degree of overlap in scan positions enabled us to reconstruct the spatial structure and the spectral weights of the beam. In Fig. 3.10(a1-i1) we show the simulated beam assuming the ZP design from Fig. 3.9(a) under plane wave illumination. In Fig. 3.9(e) and in Fig. 3.10(a2-i2) we show the ptychographic reconstruction of the object and the spectral beam profiles, re-

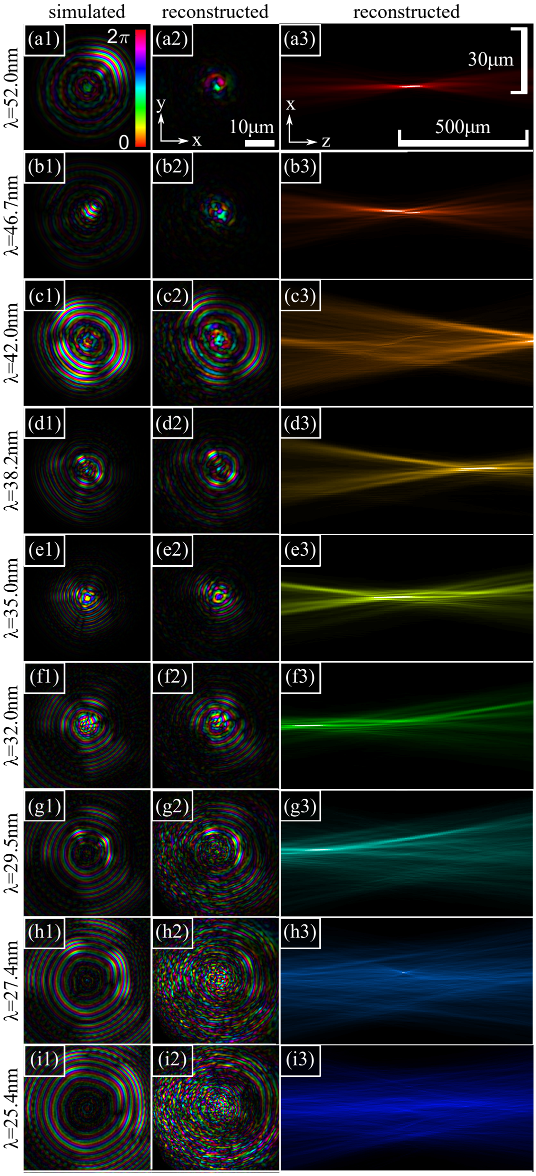

Figure 3.10: Left column: lateral (xy) cross sections of simulated spectral beam profiles (a1-i1) assuming the ZP design in Fig. 3.9(a). Middle column: lateral (xy) cross sections of ptychographic spectral beam reconstructions (a2-i2). The scale bar in panel (a2) depicts the extent of the focal plane support and is shared among the first two columns. Right column: axial (xz) cross sections (a3-i3). The scale bars along the horizontal and vertical directions have different scaling and are shared among the third column. The left and middle columns represent complex beam profiles, where amplitude and phase is encoded as brightness and hue, respectively. The right column depicts intensity linearly encoded as brightness and color encodes wavelength.

spectively. We find good qualitative agreement between simulation, as shown in Fig. 3.10(a1-i1), and experiment, in particular for the central harmonics. The largest discrepancy is observed at the extremal spectral lines, where the signal-to-noise ratio is lowest and defocusing is most severe. Moreover, differences between the simulated and the reconstructed beam profiles arise from fabrication errors in the ZP, as seen in Fig. 3.9(a). In addition, the spectral wavefronts illuminating the ZP are not perfectly planar. In Fig. 3.10(a3-i3) we show each spectral beam intensity integrated along the y-direction at ±500 µm around the focal plane. This projected view is adopted here due to the lack of centrosymmetry in the beam.

Figure 3.9(e) shows the relative energy of the reconstructed beam (orange dots) as compared to the spectrum extracted using the SHM (turquoise line). We note that the spectrum measured by the SHM is measured without ZP in the beam. Thus the spectra obtained from the SHM are not expected to match in the weights of the spectral lines estimated by ptychography. It is emphasized that no a priori knowledge was used to obtain the spectral weights during the reconstruction process. This is possible because the object is binary (ptychographic reconstruction shown in Figure 3.9(e), left). In cases where the object is dispersive, modulating each spectral wavefront in a different way, additional information about the source spectrum is required [70].

3.7 Discussion and conclusion

In summary, we proposed a new route to polychromatic focusing based on spatial entropy minimization, enabling flux balancing in the design of polychromatic focusing optics. The ability to efficiently shape and focus the polychromatic flux offered by HHG sources is a key challenge in the realization of spectrally-resolved tabletop EUV microscopes in the near future. Our proof-of-concept experiments demonstrate multispectral focusing and wavefront shaping are possible with binary DOEs, which were previously not considered for tabletop ptychographic scanning microscopes. Furthermore, we show that multispectral ptychography is capable of reconstructing a multitude of complex-shaped EUV field distributions in parallel, thus providing a method that can effectively use the generated wavefronts for spectrally-resolved high-resolution imaging. Future studies may build on this work, pre-characterizing polychromatic wavefronts and subsequently leveraging this information as a priori knowledge for EUV microscopy with chemical sensitivity.

Recent work suggests that multispectral ptychography may be used to characterize both the spatial and spectral structure of attosecond pulses [71]. We have seen in this study that entropy minimization yields DOE designs producing beams with multiple, flux-balanced diffraction orders, which axially coincide upon discrete wavelength changes. Consequently this approach may result in beams with extended depth of focus or even non-diffracting beams when applied to attosecond pulses [95]. However, the influence of our DOEs on the temporal structure of such attosecond pulses has not been investigated, and may be expected to lead to significant spatio-temporal couplings that are common to diffractive optics [96].

In this case we expect that entropy minimization is inefficient, as the total flux for each spectral beam contribution has to be shared among a continuum of diffraction orders. We believe that beam shaping based on minimum entropy is most suitable for light sources with discrete line spectra. However, cascaded rather than monolithic DOEs may be considered in future work to increase efficiency and achieve achromatic performance [49, 50].

Future challenges are computational in nature: first, while the entropy constraint in the focal plane allowed us to use continuous optimization techniques, the binary constraint imposed on the ZP renders the underlying optimization problem non-convex. We proposed a heuristic search strategy based on random flips and annealing, which worked for the moderately sized binary ZPs used here but will require more efficient schemes for large-scale focusing optics with orders of magnitude more resolution elements per dimension. This would enable the design of DOEs with larger opening angles and smaller outer zone widths. Similarly, reflective DOEs require larger areas to be optimized but could reach higher efficiencies when used in grazing incidence.

The present work constitutes an approach to polychromatic wavefront sensing that offers orders of magnitude higher lateral resolution than traditional Hartmann-Shack sensors. This may provide new insights into the transfer of aberrations and their spectral dependence in the up-conversion of high-harmonic generation [25, 97].

Chapter 4

High-resolution wavefront sensing and aberration analysis of multi-spectral extreme ultraviolet beams

Coherent multi-spectral extreme ultraviolet beams have great potential for providing high spatial and temporal resolution for microscopy and spectroscopy applications. But due to the limitations of short-wavelength optics and the broad bandwidth, it remains a challenge to perform quantitative, high-resolution beam characterization. Here we present a wavefront sensing solution based on multiplexed ptychography, with which we show spectrally-resolved, high-resolution beam reconstructions. Furthermore, using these high fidelity quantitative wavefront measurements, we investigate aberration transfer mechanisms in the high harmonic generation process, where we present and explain harmonic-order dependent astigmatism inheritance from the fundamental wavefront. This ptychographic wavefront sensing concept thus enables detailed studies of the high-harmonic generation process, such as spatiotemporal effects in attosecond pulse formation.

The content of this chapter has been published as: Mengqi Du, Xiaomeng Liu, Antonios Pelekanidis, Fengling Zhang, Lars Loetgering, Patrick Konold, Christina L. Porter, Peter Smorenburg, Kjeld S. E. Eikema, and Stefan Witte, *High-resolution wavefront sensing and aberration analysis of multi-spectral extreme ultraviolet beams,* Optica. **10**, 255:263 (2023).

4.1 Introduction

Tabletop high-order harmonic generation (HHG) sources produce broadband, spatially coherent radiation in the extreme ultraviolet (XUV) and soft-X-ray (SXR) regime [98, 99]. Recent advances in HHG source development offer high-brightness high-harmonic beams with stable spectrum, intensity and wavefront distributions, which have enabled a wide range of applications in XUV microscopy [100–102] and attosecond science [103, 104]. For many applications, it is beneficial to be able to measure and control the wavefront of high-harmonic beams to achieve a desired beam shape [105, 106], or to improve the focusability [107–109]. Among XUV wavefront sensing methods, Hartmann sensors have been first used at a synchrotron source [110], where spectrally filtered monochromatic wavefronts were measured. Spectrally averaged wavefronts of HHG beams have also been characterized in this way [111, 112]. Hartmann sensors only require a single-shot measurement, but the spatial resolution is limited by the spacing of the pinhole arrays, which is often in the range of tens or hundreds of microns. Point-diffraction interferometry [113] also offers a single-shot measurement of an averaged HHG wavefront by creating a point source as a reference wave. The common limitation of theses methods is that any difference between harmonic orders is neglected.

In order to characterize wavefronts for each harmonic order, a scanning diffraction method called SWORD has been developed [114, 115]. SWORD scans a slit across a high-harmonic beam and records frequency-resolved diffraction signals using a flat-field spectrometer. By calculating the centroid of spectrally separated diffraction orders, local wavefront slopes can be determined for each harmonic independently. Using SWORD, order-dependent intensity and wavefront distributions of high-harmonic beams have been measured and investigated [115]. These measurements led to a better understanding of the physics of HHG process, including spatialtemporal coupling effects, as well as long and short trajectory contributions to HHG wavefronts [116]. The drawback of SWORD is that only a strip of the wavefront is measured by the scanning slits, and the reconstruction often relies on assumptions of certain symmetry of the beam. Furthermore, the resolution is limited by the width of the scanning slit, often in the range of tens of microns, while narrower slit leads to more scan points and longer measurement times. An alternative method, called lateral shearing interferometry (LSI) [117], circumvents slow scanning by acquiring a double-shot measurement, which however relies on producing two identical high-harmonic beams and controlling the shearing between them. Recently, a single-shot spectrally resolved wavefront sensing method called spectroscopic Hartmann sensors was developed [118], where empty apertures in conventional Hartmann masks are replaced by transmission gratings to provide spectral sensitivity. In this case, wavefront reconstructions rely on identification of each diffraction peak from each aperture. This requires the spacing among apertures on the mask to be large, often in the range of tens or hundreds of micrometers, which leads to sparse sampling of the wavefront. That sampling requirement ultimately limits the spatial resolution and the accuracy of the wavefront reconstructions.

Since many materials absorb XUV and SXR light, refractive optics are impossible and broadband reflective optics need to be grazing with nm-scale smoothness and figure error. To overcome the optics limitation for this wavelength range, computational methods have been advanced in diffractive optics design for beam control [109, 119], as well as in diffractive microscopy [67]. Ptychography [65, 67] is a scanning coherent diffractive imaging and wavefront sensing technique, where conventionally an object is translated across a localized beam in overlapping regions, and a series of diffraction patterns are recorded as a function of scan positions. Using phase-retrieval algorithms, both complex-valued object and probe beam can be reconstructed simultaneously. In the past, ptychography has been explored as a wavefront sensing tool in the optical [120, 121] and X-ray regimes [122, 123]. The unique advantage of ptychographic wavefront sensing is that it offers robust reconstructions of both intensity profiles and wavefront variations with high spatial resolution given by the numerical aperture of the optical system, which can be orders of magnitude higher than what Hartmann sensors offer. Another advantage is that ptychography can be used to measure partially coherent beams, reconstructing multiple spatial and/or temporal modes simultaneously [70, 109, 121, 123–125].

Conventional ptychography uses a focused or spatially localized beam to scan a relatively large, extended object. The finite extent of the beam fulfills the oversampling requirement in the measured diffraction patterns. Our challenge is to directly characterize a free-space propagated, extended multi-spectral high-harmonic beam that is typically much larger than the test object, where different harmonic orders exhibit similar intensity and wavefront distributions. We show that by swapping the roles between the beam and the object, we are able to reconstruct an extended XUV beam, with spectrally-resolved intensity and wavefront distributions at a high spatial resolution. We present an optimized design strategy for our ptychographic wavefront sensor (PWFS), capable of characterizing multi-spectral HHG sources. Furthermore, we discuss potential applications of this quantitative, high-fidelity wavefront sensing tool, where it can provide insights into the spatialtemporal coupling, electron trajectories, and other physical aspect of high-harmonic generation processes. Last but not least, we focus on investigating the aberration transfer mechanism from the fundamental beam to the high-harmonic beam, where we show harmonic-number dependent beam aberrations. We find a significant effect of the HHG process itself on the wavefront of the harmonics. Combined with theories, we show that the dipole phase can either increase or compensate astigmatism transferred from an astigmatic fundamental beam.

4.2 Methods

4.2.1 Experiment

The schematic of the experimental setup is shown in Fig. 4.1(a). The fundamental near-infrared (NIR) beam is generated from a Titanium:sapphire-seeded non-collinear optical parametric chirped-pulse amplifier [126]. The system out-

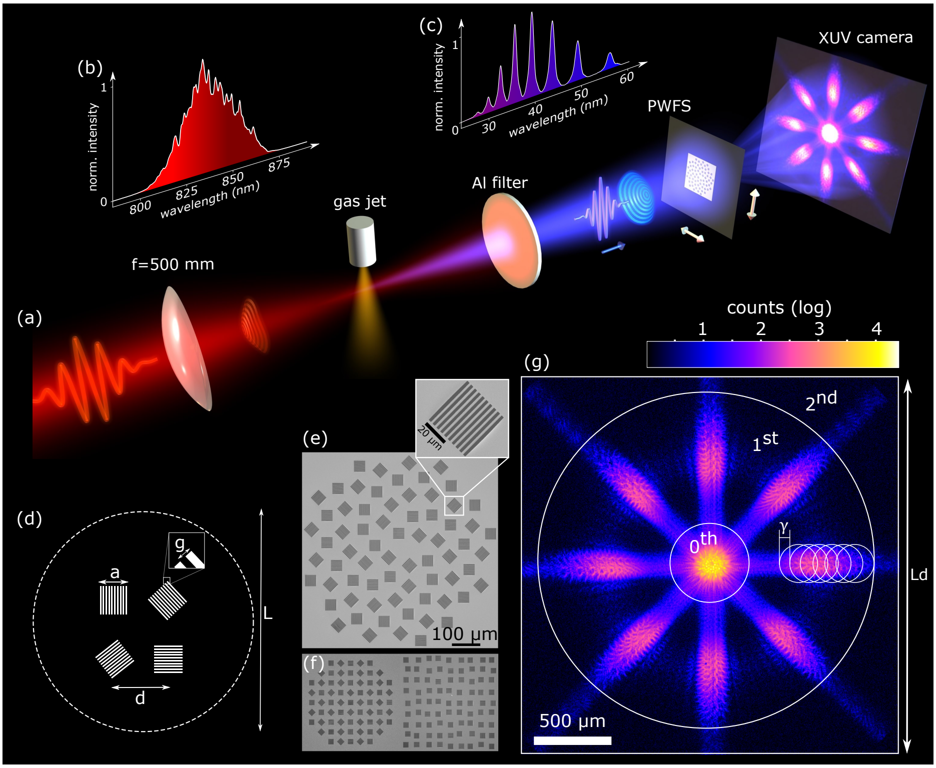

Figure 4.1: (a) HHG setup: The NIR beam is focused by a lens f = 500 mm into an argon gas jet to generate XUV beams. A 200 nm thick aluminium filter blocks the NIR beam. The PWFS is scanned transversely across the XUV beam, and the diffraction patterns are measured by the XUV camera. (b) Spectrum of the fundamental beam. (c) Spectrum of the high-harmonic beam after the Al filter. (d) Design concept of PWFSs. The key parameters are the aperture size a, the grating pitch g, the aperture separation distance d, and the PWFS size L. (e,f) SEM images of aperiodic, periodic, and quasi-periodic PWFSs. (g) Example of a measured diffraction pattern from the PWFS in e.

puts 4 mJ, 30 fs, 300 Hz NIR pulses centered at 830 nm. A typical spectrum of the fundamental beam is shown in Fig. 4.1(b). The NIR beam is focused by an f = 500 mm lens into an argon gas jet with an aperture size of 200 µm, and a backing pressure of 6 bar. We consider this a loose focusing geometry, where the Rayleigh length of the NIR beam is 5 mm, which is significantly longer than the estimated 1 mm interaction length. The generated harmonic beam is separated from the co-propagating NIR radiation using a 200 nm thick Aluminium transmission filter. The high-harmonic spectrum after the filter is obtained by measuring the diffraction from a transmission grating. A typical spectrum is shown in Fig. 4.1(c), where eight harmonics from the 15th to 29th order are observed. In contrast to conventional ptychography, where a relatively large object is translated with respect to a localized small beam, in our experiment we scan a relatively small PWFS across a larger extended multi-spectral XUV beam. In this way, the roles between the probe and the object are exchanged. The PWFS is mounted on an XY translation stage (Smaract, SLC-1730-S-HV), and scanned in a concentric ring pattern. The diffraction patterns are recorded using an XUV-sensitive CCD camera (Andor iKON-L) cooled to $-60\,^{\circ}$C.

4.2.2 Binary mask design for ptychographic wavefront sensing

To accurately characterize HHG wavefronts, a PWFS mask design is needed that densely samples local wavefront variations, while simultaneously having sufficient spectral diversity. We found that the key elements of a successful binary PWFS design are strongly wavelength-selective elements (gratings) and finite-sized apertures that provide clear near-field diffraction signatures (Fig. 4.1(d)). The combination of both far-field and near-field diffraction given by the gratings and apertures ensures robust ptychographic reconstructions. In contrast, tests with PWFS designs that lack one of these features, either only containing large gratings, or consisting of similarly laid-out apertures without gratings, all failed to yield multi-wavelength wavefront reconstructions.

To specify a successful PWFS design, we use the Fresnel number $F = \frac{x^2}{\lambda z}$ to quantify the near- and far-field diffraction features, where x is the size of the diffracting element, λ is the XUV wavelength, and z is the camera-PWFS distance. The aperture size a (in Fig. 4.1(d)) is chosen such that the Fresnel number of a single aperture is between 0.5 and 5, and the grating pitch g such that its Fresnel number is less than 0.1. The average distance d between apertures is between 1.5-2 times the aperture size to maintain a relatively high fill factor of about 25%, which allows for efficient use of beam flux. This fill factor is over 2x higher than what can typically be achieved with spectroscopic Hartmann masks [118], as they need larger separation between apertures for reliable spot centroiding. As a result, the efficiency of using PWFSs can be a similar factor 2 higher given the higher throughput. The grating apertures can be arranged in aperiodic, quasi-periodic, or periodic arrangements (Figs. 4.1(e,f)), and different grating orientations can be chosen to increase the camera fill factor.

The binary PWFSs shown in Figs. 4.1(e,f) are fabricated using focused-ion-beam milling, where the substrate is a freestanding 100 nm thick silicon nitride membrane, coated with a 100 nm thick gold layer for complete opaqueness in the XUV regime. These PWFSs are designed for measuring our high-harmonic beams in the wavelength range of 20 nm to 60 nm, with a working distance (PWFS to camera) of 50-80 cm. Each PWFS consists of square apertures with a size of $a = 40$ µm, filled with $g = 4$ µm pitch transmission gratings. The PWFS in Fig. 4.1(e) contains four different grating orientations, resulting in an 8-fold symmetric diffraction pattern on the camera as shown in Fig. 4.1(g), where the 0^{th} and the 1^{st} diffraction orders are fully captured and the 2^{nd} diffraction orders are partially captured. Note that in our experiments, a complete separation of the 1^{st}

diffraction order maxima from different wavelengths is not required, in contrast to the requirements for spectroscopic Hartmann sensors, which greatly improves transmitted flux. To ensure a sufficient spectral sensitivity, the separation factor γ (in Fig. 4.1(g)) of the 1^{st} diffraction orders needs to be more than 25%. The resolution of the wavefront measurement is given by the measured numerical aperture (NA), instead of the spacing between the apertures, which can be an order of magnitude higher than using Hartmann sensors.

In a ptychography experiment, the average scan step size needs to be smaller than the aperture size (a = 40 µm) to ensure overlap within each aperture during the scan, which in our case is chosen to be 30 µm. A high-overlap factor (above 90%) is generally needed for multi-spectral ptychography. In our case it is 95%. To cover a beam area of 1.5 mm diameter, 800 scan positions are taken. Individual diffraction patterns are recorded at 30 ms exposure time. The reconstructions are performed using the PtyLab [127] software package in Python, optimized for running on a single GPU of a stand-alone computer. More specifically, the ptychographic information multiplexing (PIM) algorithm [70] is used to reconstruct the data, with the input of the diffraction patterns, the scan grid, and the pre-calibrated harmonic wavelengths. The PWFS design is used as the initial guess for the probe. On average 50 to 100 iterations are needed to obtain convergence.

4.3 Results and discussion

Eight reconstructed high-harmonic beams at the PWFS plane are shown in Fig. 4.2(a), where the amplitude and the phase are represented by brightness and color, respectively. The spatial resolution of the reconstructed beams is 1.4 µm (full-pitch), over the total field-of-view of 15 mm in diameter. The corresponding reconstructed PWFS is shown in Fig. 4.2(b), and the inset shows that the 4 µm pitch grating is well resolved. The reconstructions are repeated 10 times with different initial guesses and randomized orders of diffraction patterns. The average and the standard deviation of the reconstructed spectral weights are shown in Fig. 4.2(c). From the quantitative beam reconstructions at the PWFS plane, we can propagate them to the camera plane, and incoherently sum up all the harmonic intensities (in Fig. 4.2(d)). We compare this calculated beam with the direct bare beam measurement on the camera (in Fig. 4.2(e)). Good agreement can be observed, which also verifies the quantitative reconstruction results.

Knowing both the amplitude and phase profiles of high-harmonic beams at the plane of the PWFS enables us to numerically propagate the beams back to the generation plane in the gas jet. Figures 4.3(a,b) show beam cross sections as a function of propagation distance in the xz (horizontal) and yz (vertical) planes respectively, where the red lines indicate the gas jet position. The divergence and focal positions of each harmonic beam can clearly be identified, and a comparison of the x- and y-cross sections reveals significant astigmatism in the HHG beams. In the x-direction all harmonic beams focus at a similar distance. Except for the longest wavelength, all beams exhibit virtual foci upstream of the gas jet. In

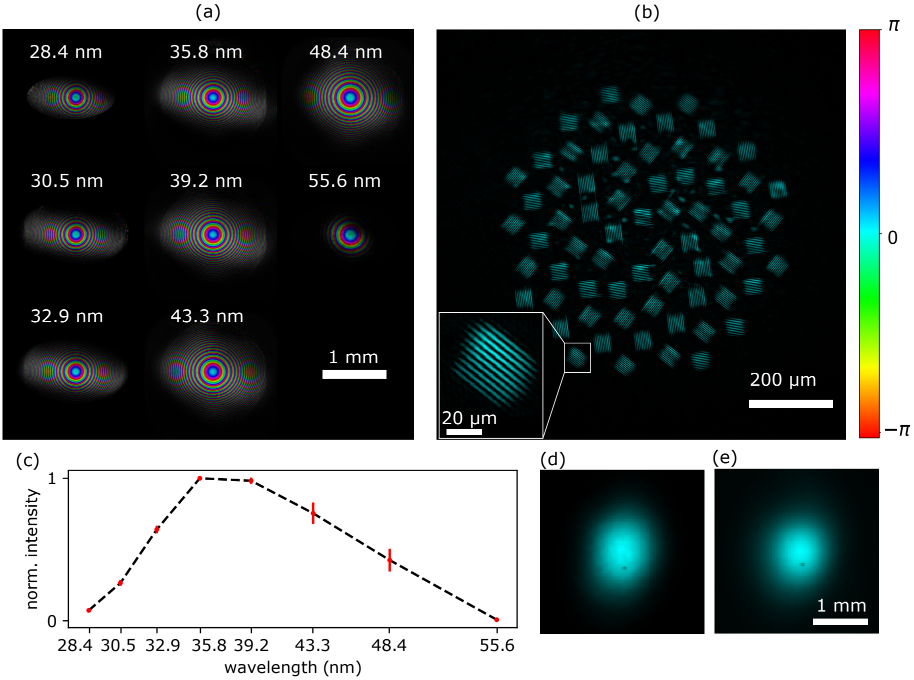

Figure 4.2: Ptychographic reconstruction of (a) eight harmonic beams and (b) the PWFS mask. In these images, brightness represents amplitude and color represents phase. (c) Retrieved spectral weights, average of 10 independent reconstructions. The error bar shows 5x the standard deviation. Images of the XUV beam at the camera plane (d) calculated from the reconstructions, and (e) directly measured by the camera, respectively.

contrast, in the y-direction a clear difference of focus positions with respect to the gas jet can be observed, and these are real foci because they appear downstream of the gas jet. This wavelength-dependent focus variation is effectively an intrinsic chromatic aberration of the HHG process, and this effect has recently attracted attention from the attosecond community [107, 115, 116]. Our PWFS approach has sufficient resolution to quantify this effect, enabling an accurate study of the influence of the dipole phase as a function of the generation geometry.

Propagating all harmonic beams to a common focal plane enables us to investigate the spatiospectral and spatiotemporal properties of the XUV beam focus. Figure 4.4(a) displays the intensity distributions of each harmonic focus, and the incoherent addition gives the polychromatic focus of attosecond pulses in Fig. 4.4(b). The broadband focus has a full-width-at-half-maximum (FWHM) of 30 µm. We can see that the upper and the lower parts of the beam are not reached by all harmonics, in contrast to the beam center where all harmonics are present. Within this focal distribution, three separate locations are marked with colored

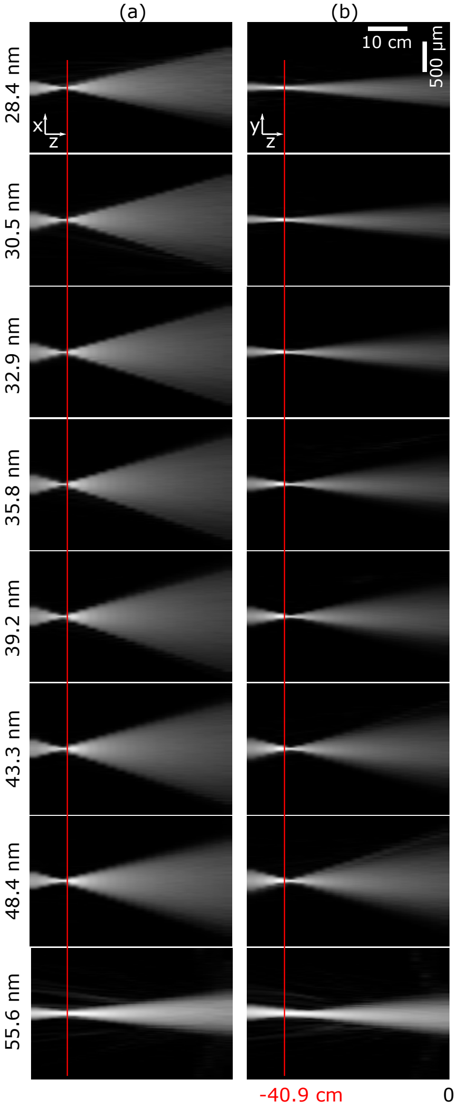

Figure 4.3: Cross section of eight high-harmonic beams in (a) xz, (b) yz planes. Beams propagate from left to right. The red lines indicate the physical location of the gas jet. The right edge of the images is the plane where the PWFS was located.

dots: the retrieved spectra at these positions (Fig. 4.4(c)) show significant differences. From these spectra the local Fourier-limited temporal pulse shapes can be determined (Fig. 4.4(d)), the FWHMs of which are 180, 215, and 246 attoseconds (as). To highlight the complicated spatiotemporal couplings that can arise from such spectrally-dependent wavefronts, a spatial map of the Fourier-limited pulse duration at the focus is shown in Fig. 4.4(e), and the duration varies between 150 and 280 as.

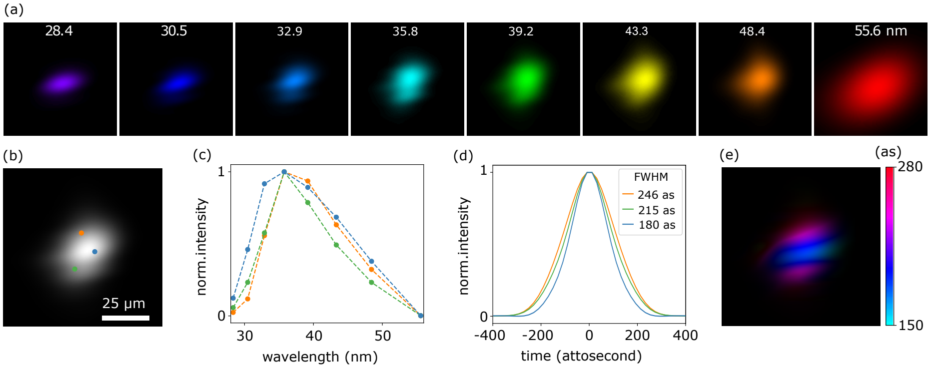

Figure 4.4: (a) Color coded intensity plots of each harmonic focus. (b) Intensity profile of the polychromatic focus summed over all high-harmonic beams. (c) Spectra and (d) Fourier-limited pulses, at three different locations within the focus as marked in (b). (e) 2D spatiotemporal map of the polychromatic focus.

Figure 4.3(a) also shows another important aspect of the focusing properties of attosecond XUV pulses, namely the wavelength-dependent astigmatism in the high-harmonic beams. Previous studies [111, 112] have investigated how aberrations are transferred from the fundamental to the high-harmonic beams. However only spectrally averaged wavefront measurements with limited spatial resolutions have been reported. Our spectrally-resolved, high-resolution wavefront reconstructions enable a more complete and quantitative analysis.

To quantify the wavefront transfer in the HHG process, high-resolution measurements of the fundamental beam wavefront are performed using ptychography in parallel to the XUV measurements as shown in Fig. 4.5(a). Due to the broad bandwidth of the fundamental beam, a range of bandpass filters (bandwidth 1 nm) are used to perform single-wavelength ptychography. Figure 4.5(b) shows the spectrum of the fundamental beam, centered at 830 nm and with a FWHM of 40 nm. The wavefront sensor (WFS) used for the fundamental beam is a binary mask containing 2 μm sized apertures arranged in a golden spiral pattern. The ptychographic reconstruction of the WFS is shown in Fig. 4.5(c). Three beam reconstructions at 808 nm, 830 nm, and 852 nm are presented in Fig. 4.5(d). From the Zernike analysis in Fig. 4.5(e), we can verify that different spectral components across the full spectrum show similar aberration compositions. Therefore, the beam at the central wavelength 830 nm is used to represent the fundamental beam in the simulations to investigate the aberration transfer mechanism in this work.

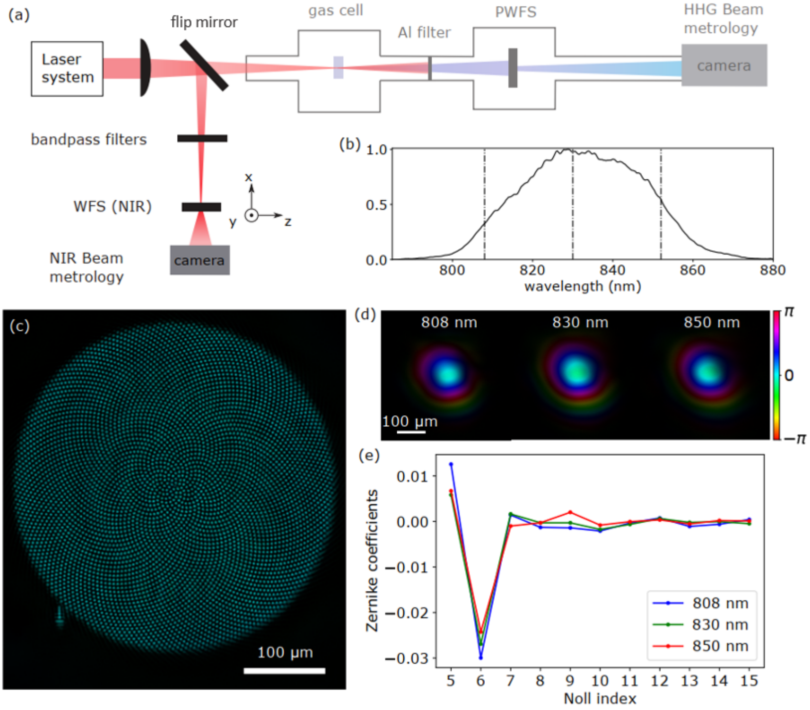

Figure 4.5: (a) Setup of ptychography measurement for fundamental beams. (b) A typical spectrum of the broadband fundamental drive laser. (c,d) Reconstructed WFS, and three beams at short, middle, and long wavelength range of the spectrum, respectively. (e) Zernike coefficients of the three beams.

We analyse beam aberrations using Zernike decomposition, where each wavefront is decomposed into mutually orthogonal Zernike polynomials with their resulting coefficients. We vary the astigmatism in the fundamental beam by tilting the focusing lens before the gas jet. Figure 4.6 displays two sets of data with more and less aberrated beams in the top and bottom rows, respectively. The reconstructed fundamental beams are propagated to the equivalent gas jet location, where the Zernike coefficients are extracted as presented in Figs. 4.6(a,d). To better visualize higher-order aberrations in the generated high-harmonic beams, the first four Zernike components in Noll convention, i.e. piston, tip, tilt, and defocus, are excluded in Figs. 4.6(b,e). The corresponding Zernike coefficients for higher-order polynomials (Noll index > 4) are plotted in Figs. 4.6(c,f). Firstly, we observe that aberrations, more specifically the oblique and vertical astigmatism contained in the fundamental beam, are transferred to the high-harmonic wavefronts. Secondly, harmonic-order dependent aberrations can also be seen in the aberrated case, in the sense that some harmonic orders inherit more astigmatism

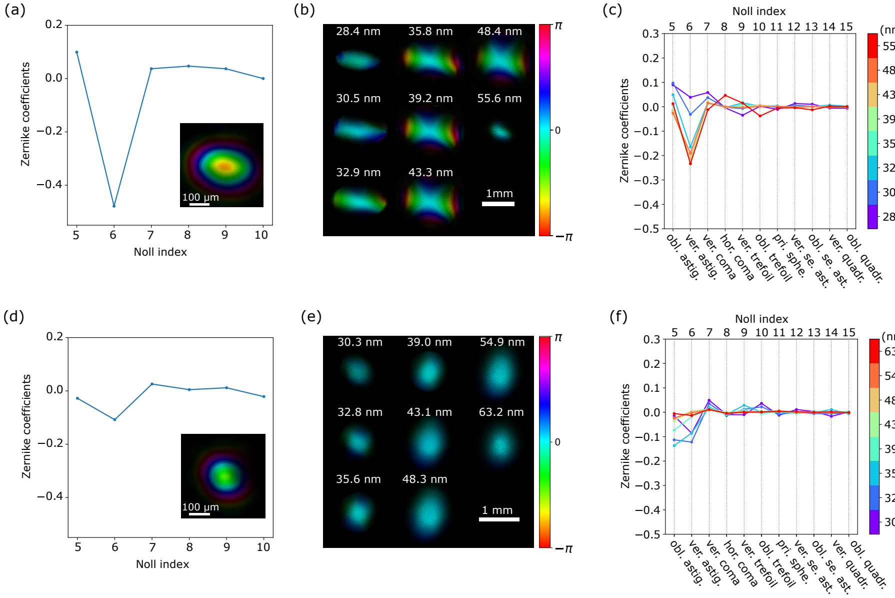

Figure 4.6: (a,b,c) Aberrated fundamental beam, high-harmonic beams, and their Zernike coefficients. (d,e,f) Aberration-minimized fundamental beam, high-harmonic beams, and their Zernike coefficients.

from the fundamental wavefront than others. This variation can be explained by taking into account the dipole phase contribution in the HHG process. In theory, the wavefront of a q$^{\text{th}}$-order harmonic beam can be expressed with two contributions [116]:

$$\Phi_q = q\Phi_f + \Phi_d(I_f), \tag{4.1}$$

where the first term describes the direct phase transfer from the phase of the fundamental beam (Φ_f) to the q$^{\text{th}}$ harmonic, and the second term is the dipole phase contribution ($\Phi_d(I_f)$), resulting from the electron propagation in the continuum. Generally, two different electron trajectories, i.e. the long and short trajectories, have different dipole phases. Since in our current experiments, the phase matching condition favors the short trajectories, in the discussion below only the dipole phase for the short trajectories is considered. Following an analytical solution to the strong-field approximation, the dipole phase is expressed as $\Phi_d(I_f) = \gamma_s(\Omega_q - \Omega_p)^2/I_f$ [116], where γ_s is a constant related to the central wavelength of the drive laser, Ω_q is the frequency of the q$^{\text{th}}$ harmonic, Ω_p is the frequency related to the ionization energy of the gas $E_{gas} = \hbar\Omega_p$, and I_f is the fundamental intensity. Therefore, the high-harmonic wavefront is affected by both the fundamental phase and intensity, as well as the harmonic order.

We can now use this insight to study and control the astigmatism in the high-harmonic beams, by tuning the dipole-phase effect through a variation of the

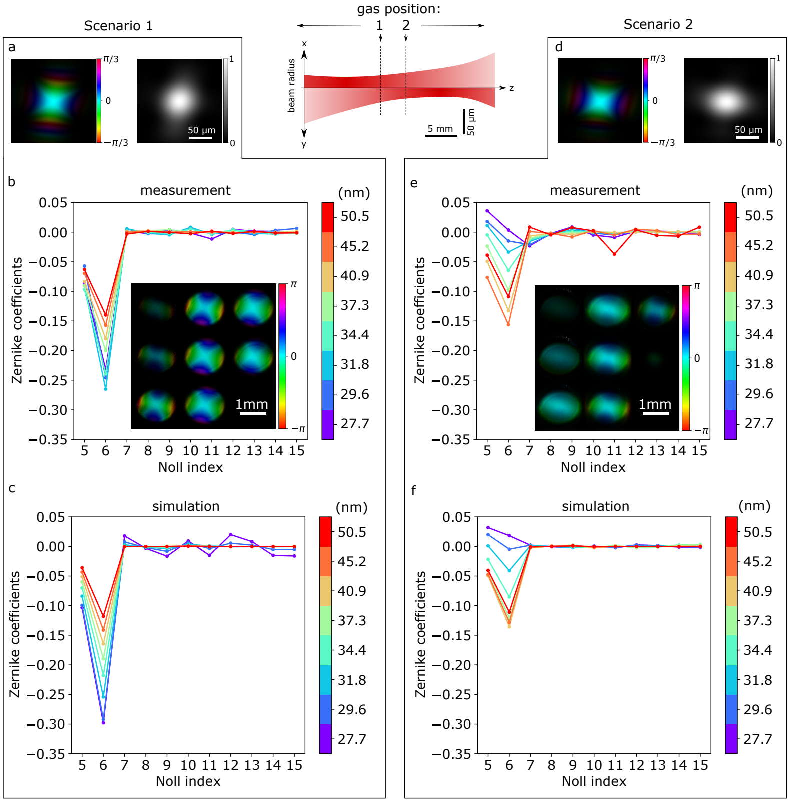

Figure 4.7: Astigmatism transfer analysis on HHG beams generated at two gas positions. (a) Fundamental phase and intensity, (b,c) Zernike coefficients of measured and simulated HHG beams in scenario one (gas position 1). (d) Fundamental phase and intensity, (e,f) Zernike coefficients of measured and simulated HHG beams in scenario two (gas position 2).

fundamental intensity profile. To demonstrate this concept, we generate high-harmonic beams from two different gas jet positions with respect to the beam waist of the astigmatic fundamental beam, as shown in Fig. 4.7. The cross-section (xz and yz) plot shows that the two foci of the fundamental beam are separated by 15 mm, and the focus in the x-axis is upstream of the one in y. In scenario one, the gas jet is placed at position 1 in between the two foci, where the fundamental intensity is circularly symmetric. The phase and intensity profiles of the fundamental beam are displayed in Fig. 4.7(a). From the direct phase transfer ($q\Phi_f$), high-harmonic beams inherit the astigmatism from the fundamental phase. The circular fundamental intensity leads to a stigmatic, or circularly symmetric dipole phase contribution. The resulting HHG wavefront aberrations are therefore dominated by the direct phase transfer, and higher-order harmonics exhibit larger Zernike coefficients for astigmatism (Fig. 4.7(b)).

In scenario two, the astigmatism contribution induced by the dipole phase and fundamental wavefront partially compensate each other. Specifically, the gas jet is moved to position 2, which is closer to the vertical focus and therefore the intensity profile of the fundamental beam is more elliptical (in Fig. 4.7(d)). This non-circular intensity shape results in an astigmatic dipole phase contribution. Intuitively, since the dipole phase ($\propto I_f^{-1}$) is always divergent, this elliptical profile will lead to a stronger wavefront curvature in the vertical direction, while the wavefront of the fundamental at position 2 is more divergent in the x-direction. Consequently, the two foci will shift closer to each other, and the dipole phase results in significant astigmatism compensation. Our measurements shown in Fig. 4.7(e) indeed confirm that less astigmatic high-harmonic beams are generated in this case. Moreover, the dipole phase has a quadratic dependence on the harmonic order, hence the compensation effect is stronger for higher harmonics, which is indeed what we observe in Fig. 4.7(e). To substantiate our findings, we simulated the high-harmonic wavefronts generated in these two scenarios using the theoretical model (Eq. 4.1), where we input the measured fundamental intensity and phase (Fig. 4.7(a,d)). The Zernike analysis on the simulated HHG wavefronts (Figs. 4.7(c,f)) shows good agreement with our experimental data.

In the first scenario (in Fig. 4.8), the gas jet is aligned in the middle of the two foci of the astigmatic fundamental beam, such that the intensity distribution is circularly symmetric. Using Eq. 4.1 and the reconstructed fundamental beam, we calculate the directly transferred phase ($q\Phi_f$), the dipole phase ($\Phi_d(I_f)$), and the total phase (sum of the two) for each harmonic beam in the gas plane, which are shown in Figs. 4.8(a1-a3), respectively. We assume the intensity of the high-harmonic beam in the gas jet is proportional to ${I_f}^4$, which matches the beam waist calculated from the reconstruction results. From the aberration analysis, we show that the astigmatism is inherited by the harmonic beam via the direct phase transfer from the fundamental phase, and the dipole phase hardly has any contribution. To better compare this simulation to the experimental results, we numerically propagated the simulated harmonic beams from the gas jet to the PWFS plane, and the Zernike decompositions in Figs. 4.8(b1-b3) show aberration analysis of the corresponding phases at the PWFS plane. Note that the the Zernike decomposition is not free-space propagation invariant. The sign flip in astigmatism from the gas jet to PWFS plane through propagation is related to the defocus term (Noll index 4) which is not shown in these plots. The same conclusion can be drawn at the PWFS plane: in this gas jet alignment, the high-harmonic beams exhibit astigmatism inherited from the direct phase transfer, and the coefficients monotonically increase with the harmonic orders.

In the second scenario, the gas jet is aligned at position 2 towards the focus in the y-axis (vertical) of the beam, where the intensity distribution of the fundamental beam is elliptical. This results in an elliptical dipole phase for each harmonic as shown in Fig. 4.9(a2), which leads to astigmatism in the dipole phase contribution. The corresponding aberration analysis shows that in the gas jet plane, the sign of the astigmatisms from the dipole phase is opposite from the direct phase transfer (Figs. 4.9(a1,a2)), therefore offering a compensation effect as shown in Fig. 4.9(a3). After propagating the beams to the PWFS plane in

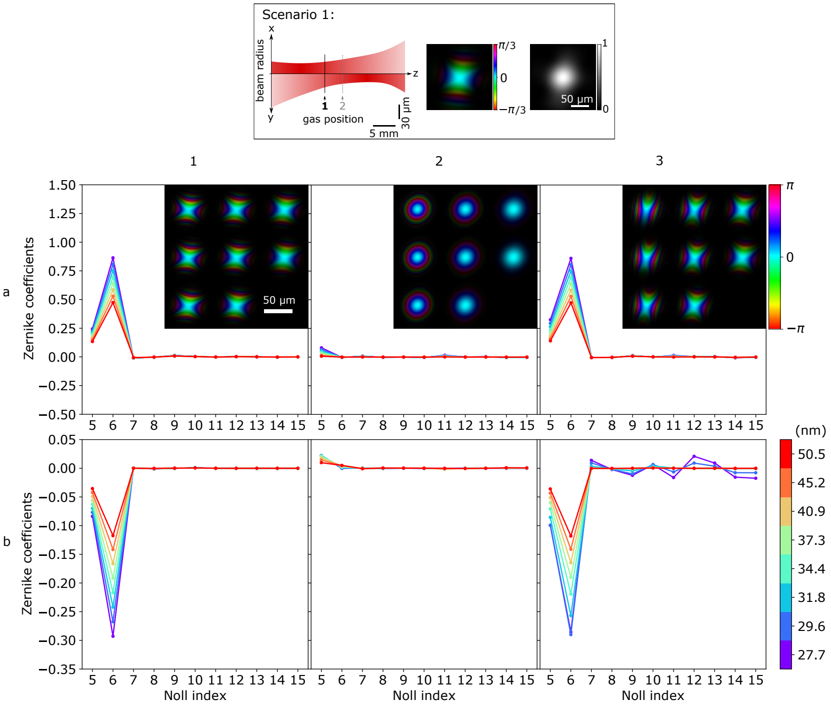

Figure 4.8: Simulated phase profiles of high-harmonic beams and the Zernike analysis in scenario 1, where the generated harmonic beams inherit strong astigmatism from the fundamental beam. Columns (1,2,3) are the directly transferred phase ($q\Phi_f$), the dipole phase ($\Phi_d(I_f)$), and the total phase (Φ_q), respectively. Rows (a,b) show analysis in the gas plane and the PWFS plane, respectively.

the far-field, the harmonic beams also contain less astigmatism as compared with Fig. 4.8(b3). These simulation results match well with our experimental results in Fig. 6.

4.4 Conclusion

We presented a high-resolution ptychographic wavefront sensing method for multi-spectral, spatially extended high-harmonic sources. The best design strategy for a ptychographic wavefront sensor is discussed, and high-fidelity reconstructions of eight harmonic beams with a full-pitch spatial resolution of 1.4 µm are shown. Using the quantitative reconstruction results and numerical propagation, we evaluated the spatiospectral, as well as spatiotemporal focusing properties of HHG pulses. Furthermore, we studied the aberration transfer mechanism in the high-harmonic generation process, where we observe a strong correlation in astigmatism between the fundamental beam and the high-harmonic beams. Moreover, with the help of a theoretical model, we experimentally demonstrated

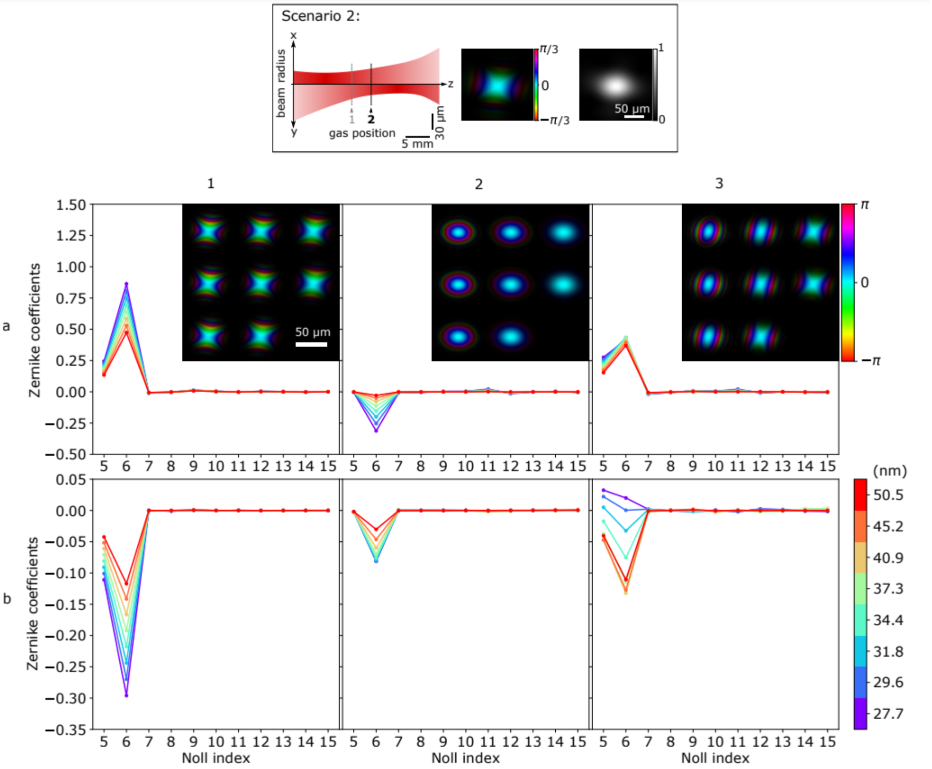

Figure 4.9: Simulated phase profiles of high-harmonic beams and the Zernike analysis in scenario 2, where the dipole phase effectively compensates for the astigmatism.. Columns (1,2,3) are the directly transferred phase ($q\Phi_f$), the dipole phase ($\Phi_d(I_f)$), and the total phase (Φ_q), respectively. Rows (a,b) show analysis in the gas plane and the PWFS plane, respectively.

that it is possible to control the astigmatism in the high-harmonic wavefronts generated from an astigmatic fundamental beam by tuning the dipole phase contribution through optimizing the gas jet position.

We believe that ptychographic wavefront metrology has great potential to facilitate quantitative studies on high-harmonic generation and attosecond XUV pulses at unprecedented spatial and spectral resolution. As an outlook, by combining a systematic focus scan with the wavefront measurements, we can further investigate chromatic aberration in the XUV beam to uncover potential spatiotemporal couplings in attosecond pulses. Moreover, using adaptive optics to precisely control and manipulate various aberration forms besides astigmatism in the fundamental beam, will enable us to study more complicated aberration transfer mechanisms in the high-harmonic generation process, which may in turn facilitate wavefront shaping methods for XUV beams.

Chapter 5

Observation of chromatic effects in high-order harmonic generation

High-harmonic generation sources can produce coherent, broadband radiation at extreme-ultraviolet and soft-X-ray wavelengths. The wavefronts of the generated high-order harmonics are influenced by the incident laser field, the generation conditions, and geometry. These influences depend on harmonic wavelength, which may result in wavelength-dependent focusing properties and spatiotemporal couplings that can affect attosecond physics experiments. We experimentally demonstrate and characterize these chromatic effects in high-harmonic generation by measuring the spectrally resolved high-harmonic wavefronts as a function of generation conditions. We find that the high-harmonic generation process can have significant intrinsic chromatic aberration, particularly for converging incident laser fields. Furthermore, we identify regimes where chromatic effects can be minimized, and show that analytical single-atom models allow accurate predictions of harmonic wavefronts produced by a specific driving field.

The content of this chapter has been published as: Xiaomeng Liu, Antonios Pelekanidis, Mengqi Du, Fengling Zhang, Kjeld S. E. Eikema, and Stefan Witte, *Observation of chromatic effects in high-order harmonic generation,* Phys. Rev. Res. **5**, 043100 (2023).

5.1 Introduction

High-order harmonic generation (HHG) as a laboratory-scale source of coherent soft-X-rays and extreme ultraviolet (EUV) pulses has become indispensable for many table-top coherent diffractive imaging (CDI) experiments [11, 21, 128], and attosecond physics [17]. In the high-harmonic generation process [14, 20, 129, 130], an intense broadband femtosecond infrared laser pulse, with a peak intensity on the order of $10^{14} - 10^{15}\,\mathrm{W\,cm^{-2}}$, is focused into a noble gas medium. The strong driving field leads to electron tunnelling, acceleration and recombination, subsequently leading to the generation of a chirped broadband EUV pulse [17], that for multicycle laser pulses consists of a comb of odd-order harmonics of the drive laser frequency [18, 19].

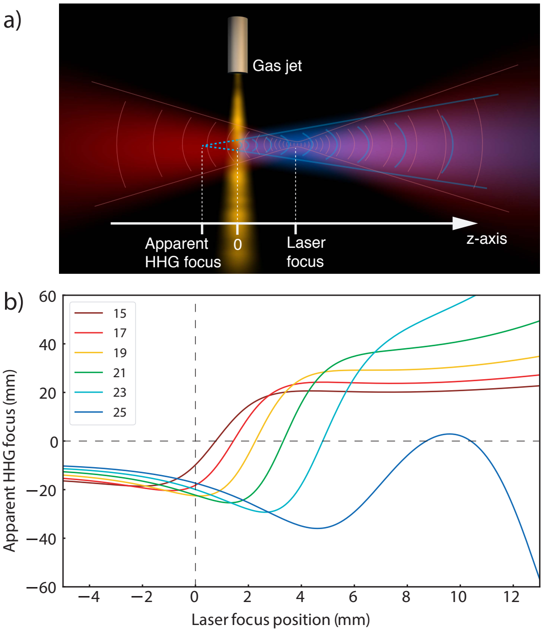

Figure 5.1: a) Typical geometry for high-harmonic generation (HHG). The wavefront curvature of the harmonics may differ from the driving field, mainly because of the dipole phase. b) Apparent focus positions of harmonics 15-25 generated in Argon with laser parameters $\lambda = 800$ nm, $I_0 = 1.7 \times 10^{14}$ W/cm^2, $w_0 = 50\ \mu$m. For both laser and HHG, positive numbers indicate a focus behind the gas jet (being a real HHG focus), and negative numbers mean the focus is before the jet (virtual HHG focus).

The ultrashort pulse duration and broad spectral bandwidth of HHG sources are key enabling features for probing ultrafast phenomena [27, 28], but there is the possibility of couplings between their temporal and spatial properties [96]. Such spatiotemporal couplings can significantly increase the pulse duration upon propagation [29], affect the propagation itself in dispersive nonlinear media [131], and have an influence on nonlinear effects [132]. In the case of time-varying polarization states, spatiotemporal couplings become even more complex [133]. In many experiments in attosecond spectroscopy [134, 135] and lensless imaging [128, 136], a high quality focus is crucial to obtain a short pulse duration and high peak intensity at the target.

While spatiotemporal coupling is typically associated with aberrations caused by optical components, recent work showed that the HHG process itself may already introduce chromatic aberrations [137–139], as the wavefront and intensity profile of the generated high-harmonic beam can depend both on the harmonic order and the generation geometry. Placing the gas medium slightly before the waist of the driving laser beam was shown to result in an HHG beam in which the wavefronts range from diverging to converging for different harmonics [139, 140].

The wavefront distribution of a high-harmonic field can be expressed as [137]:

$$\Phi_q(r, z) = q\phi(r, z) + \Phi_i(r, z), \tag{5.1}$$

where $\phi(r, z)$ is the drive laser phase, q is the harmonic order and $\Phi_i(r, z)$ is the atomic dipole phase [20, 31]. While the dipole phase is commonly approximated as $\Phi_i = \alpha_q I$ with I the laser intensity [31, 141, 142], we take the expression derived by Guo et al. [30, 137] that for the short trajectories takes the form $\Phi_i = \gamma_s(q\omega_l - \omega_p)/I$. In this expression, $\omega_p = I_p/\hbar$ is the frequency corresponding to the ionization energy I_p and $\gamma_s = a\omega_l^2$ with ω_l the laser frequency and a a constant. These two dipole phase expressions are mutually consistent when taking into account that the α_q-parameter depends on harmonic order and intensity [30]. The $1/I-$model is insightful as its prefactor is a true constant at fixed ω_l, and provides an analytical expression for the phase properties of HHG fields. For an HHG beam with a Gaussian spatial intensity profile, the radius of curvature of the HHG wavefront can be obtained by approximating the phase with a polynomial expansion up to r^2 (considering only short trajectories), plus the wavefront curvature of the drive laser [137]:

$$\frac{1}{R_q} = \frac{1}{R_l(z)} + \frac{4\gamma_s c\,(q\omega_l - \omega_p)^2}{I_0 w_0^2 q\omega_l}, \tag{5.2}$$

in which $R_l(z)$ is the radius of curvature of the laser field at the gas jet, I_0 is the peak intensity, and w_0 is the beam waist.

Figure 5.1 shows the concept of the harmonics being generated with a different wavefront curvature than the driving field. We set the geometry as in Fig. 5.1a, with the gas jet as the origin and positive z-values being further downstream (behind the medium). The difference in wavefront curvature of the driving laser field leads to a different ‘apparent’ focus position where the harmonics appear to originate from, with significant dependence on the harmonic order [137, 139]. We use Eq. (5.2) to calculate the expected apparent foci for our typical generation conditions, with the results shown in Fig. 5.1b. In particular for the laser focusing behind the gas jet, strong wavelength-dependent variations of several Rayleigh lengths in the HHG focus positions are predicted, with most harmonics changing from a virtual to a real focus at a specific generation position. Refocusing such beams for strong-field attosecond experiments would result in severe chromatic aberrations, even when using fully achromatic refocusing optics.

A quantitative experimental verification of these predicted chromatic aberrations is challenging, as it requires a wavelength-resolved focus characterization with high spatial resolution. Alternatively, a model-independent reconstruction of the HHG focal spot is possible from high-resolution far-field measurements of the transverse complex field distribution of each harmonic. While various far-field wavefront sensing methods have been developed for HHG sources [110, 113, 138, 143–145], achieving both sufficient spatial and spectral resolution without relying on model assumptions remained challenging. Recently, a computational imaging method called ptychography has been applied for wavefront sensing applications [128, 146], where the quantitative complex electric field can be reconstructed with diffraction-limited spatial resolution. Specifically, for characterization of HHG sources, we have developed a multi-wavelength ptychographic wavefront sensing (PWFS) method [147]. In this work, we employ PWFS to study the intrinsic chromatic variations in the HHG process with unprecedented detail. The reconstructed complex field distributions from PWFS can be numerically propagated back to their apparent focus position near the generation medium, without requiring Gaussian optics or assuming certain beam symmetry. By recording PWFS data as a function of the HHG generation geometry, a detailed analysis of these intrinsic chromatic effects in HHG becomes possible. By simultaneously characterizing the complex field of the drive laser, we can compare the measured HHG beams with single-atom-model predictions for a given driving field, enabling a critical comparison of different model approaches.

5.2 Setup for ptychographic wavefront sensing

We measure the multispectral EUV wavefronts and the fundamental laser wavefront with the experimental setup outlined in Fig. 5.2a. High harmonics are generated in a gas jet, using 0.61 mJ, 45 fs, 825 nm wavelength laser pulses from a noncollinear optical chirped pulse amplifier running at 300 Hz repetition rate. The gas jet is formed by a supersonic expansion from a pulsed nozzle into a stainless steel tube with 0.6 mm inner diameter, at 2 bar Argon backing pressure. The laser crosses the jet through 100 μm diameter holes in the side of the tube. As the interaction length is significantly shorter than the 3.4 mm Rayleigh length of the laser focus, propagation effects are expected to be limited [142, 148], and we therefore focus our analysis on the single atom response and the influence of the driving laser wavefront. For the PWFS measurements, an EUV wavefront sensor mask (EUV WFS) as used in [147] is mounted on a two-dimensional translation stage (Smaract SLC-1730) and placed 40.9 cm after the gas jet. A 200 nm thick free-standing aluminum filter blocks the fundamental beam, and the HHG beam is detected by an EUV-sensitive camera (Andor Ikon-L 936SO, 2048×2048 pixels, pixel size 13.5 μm) placed 56.5 cm behind the EUV WFS. A series of diffraction patterns is recorded as the EUV WFS is transversely scanned through the HHG beam. To characterize the fundamental field, a near-

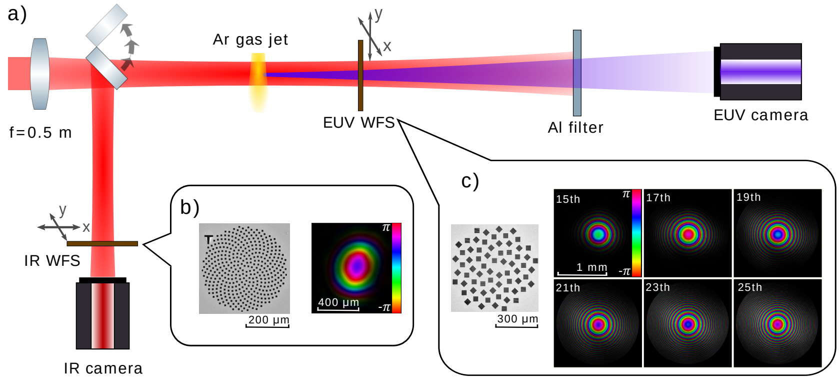

Figure 5.2: a) Experimental setup for wavelength-dependent EUV wavefront measurements. Ultrashort near-infrared pulses are focused into an Argon gas jet for HHG, using a $f = 0.5$ m lens. An EUV wavefront sensor mask (EUV WFS) is transversally scanned through the generated HHG beam for ptychographic wavefront characterization, and the resulting EUV diffraction patterns are recorded by an EUV-sensitive CCD camera. The fundamental field is also characterized using ptychography, in a separate measurement arm. b) Scanning electron microscopy (SEM) image of the near-IR wavefront sensor mask, and a reconstructed laser field (brightness linearly encodes amplitude, color represents phase). c) SEM image of the EUV WFS mask, and a set of reconstructed fields for different harmonics.

infrared ptychography measurement is set up in an auxiliary beam path outside the vacuum system. Band-pass filters are used to select single wavelengths from the driving laser, enabling characterization of the driving laser at several wavelengths across the broad spectrum. A different wavefront sensor mask is used to measure the fundamental wavefront (Fig. 5.2b). An infrared camera (Allied Vision Prosilica GT3400) is used to capture the diffraction patterns.

5.3 Results: HHG wavefronts and chromatic aberrations

From a single ptychography scan, complex fields at all harmonic wavelengths are reconstructed (Fig. 5.2c). These fields can be numerically propagated backward along the beam direction, enabling an accurate characterization of the focus position and the properties of the HHG beam [147].

A reconstruction result with an example of the numerical beam propagation for multiple harmonics is shown in Fig. 5.3. The first column (Figs. 5.3,a1-a6) contains the reconstructed multispectral EUV fields for harmonics 15 to 25 at the position of the EUV WFS. The plots in the middle column (Figs. 5.3,b1-b6) show the numerical propagation of the EUV beam through the beam waist, in which the beam direction is from left to right. The dashed white line indicates the position of the gas jet. It should be noted that only linear propagation is

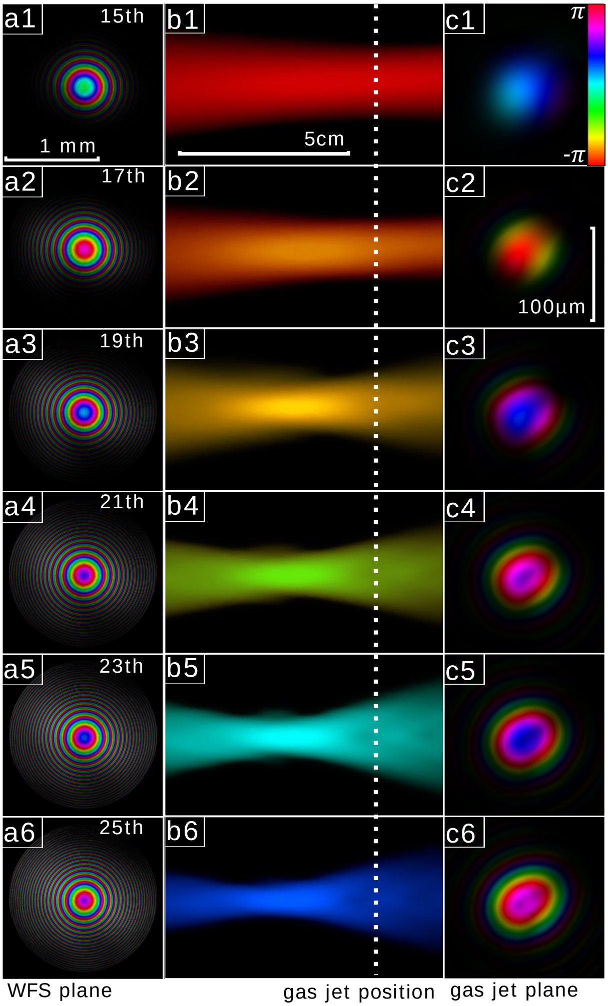

Figure 5.3: a) Reconstructed HHG wavefronts and focusing properties for a laser focus positioned 3.6 mm downstream of the jet. Left column (a1-a6): Reconstructed wavefronts of harmonic beams in the wavefront sensor plane. The corresponding wavelength (harmonic order) is 54.7 nm (15th), 48.2 nm (17th), 43.1 nm (19th), 38.9 nm (21st), 35.5 nm (23rd) and 32.6 nm (25th). Middle column (b1-b6): axial cross section of the reconstructed beam propagating through their foci. The scale bars are shared for all panels. The white dashed line indicates the gas jet position. Right column(c1-c6): reconstructed beam profiles in the gas jet plane. Intensity is linearly encoded in brightness, and phase is encoded as color.

considered here, and any (nonlinear) effects of the gas jet on the beam propagation are not included. This approach provides a detailed view of the HHG beams around their focus region, with sufficient resolution to identify that the generated harmonics clearly have different focusing properties. In this example we find that the 15$^{\text{th}}$ harmonic focuses near the gas jet plane, while the higher harmonics show progressively larger divergence at the gas jet plane (Figs. 5.3,c1-c6), and have virtual foci up to several centimeters upstream of the jet. From the ptychography scans, the complex fields of the fundamental and the generated harmonics can be directly compared around the focus region.

To study the harmonic-order dependence of the focusing properties in detail, we performed a series of PWFS measurements while varying the relative position between the laser focus and the gas jet. The results are shown in Figs. 5.4a,b where the apparent focus position of harmonics 15 to 25 is determined as a function of the relative gas jet position. Due to slight astigmatism in the fundamental beam, we observed minor differences in horizontal and vertical focusing behaviour, therefore we show separately the focus positions in the horizontal and vertical plane in Figs. 5.4a and b respectively.

In Fig. 5.4 we maintain the axis convention of Fig. 5.1, with positive numbers indicating a focus behind the gas jet (i.e. a real focus). The high resolution of our wavefront measurements enables an accurate determination of the focus position of the individual harmonics, with the major advantage that there are no assumptions needed to retrieve the focus position from the measured data, other than the paraxial approximation used in the numerical propagation of the fields. Therefore, we obtain a detailed overview of the intrinsic chromatic aberration resulting from the HHG process itself.

5.4 Discussion

The observed chromatic aberrations qualitatively follow the trends predicted by the single-atom model (Fig. 5.1b). In the regime of HHG with a converging drive laser beam, some lower-order harmonics are found to have a real focus behind the jet [139]. For these harmonics, the fundamental wavefront contribution dominates the dipole phase. When the laser focus coincides with the gas jet, all harmonic wavefronts are diverging, as only the dipole phase contribution to the harmonic phase is present, which is always divergent. The harmonic-wavelength-dependence of the dipole phase then directly results in chromatic variations. For a laser focus before the jet, all harmonics have diverging wavefronts and thus virtual foci, as expected from Eq. (5.2). Note that these virtual harmonic foci are located several centimeters upstream of the laser focus. An important observation however, is that the chromatic aberrations are significantly smaller in this geometry. The origin of this behaviour is that, while both the dipole phase and fundamental wavefront are diverging, their change as a function of harmonic order is largely inverse, thus partially cancelling wavelength-dependent variations. Figure 5.5 shows the separate influence of dipole phase (Fig. 5.5a) and wavefront transfer (Fig. 5.5b).

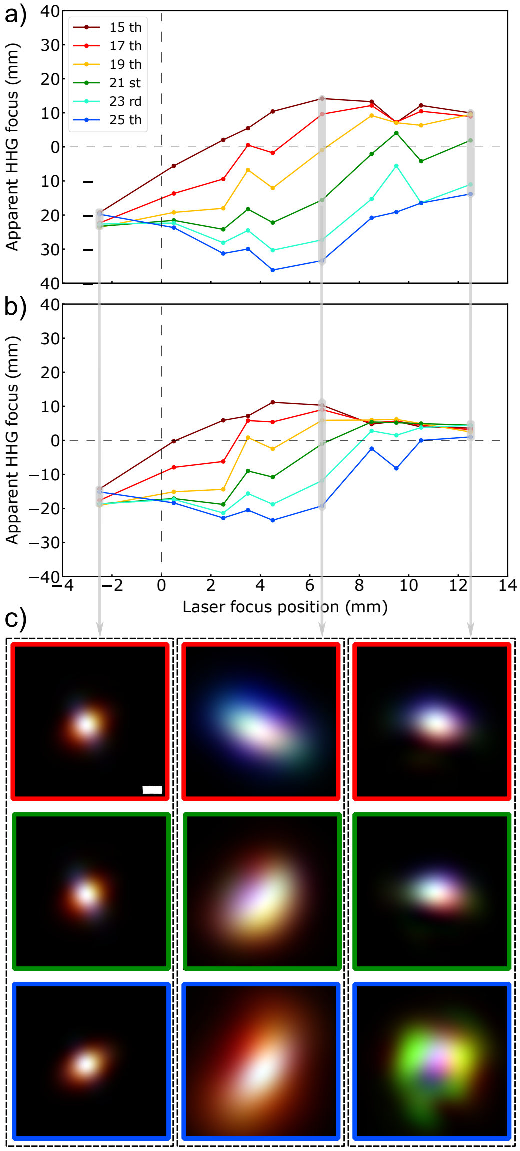

Figure 5.4: a,b) Wavelength-dependent (a) horizontal and (b) vertical focus position of the different harmonics, as determined from reconstructed HHG wavefronts. c) Overlay of reconstructed intensity profiles of harmonics 17 (red), 21 (green) and 25 (blue), at the apparent focus positions of the respective harmonics. The frame color indicates the harmonic that is in focus in that image (red H17, green H21, blue H25). The scale bar in the top left frame is 20 μm, and is shared among all images.

By analyzing the reconstructed complex beam profiles, we find that the shift between the apparent HHG source positions of different harmonics can exceed the Rayleigh length of the harmonic beams, in the present geometry by up to 2-4 times. This effect reaches a maximum when the laser focus is ~5 mm downstream of the gas jet, corresponding to about one fundamental Rayleigh length. Refocusing of such a multi-wavelength beam, even with perfectly achromatic optics, will result in an aberrated focal spot with spatially varying spectral density and therefore similarly varying durations of attosecond pulses, following model predictions [137]. To give more direct insight into the beams produced in the HHG process, we numerically reconstruct the intensity profiles of three different harmonics around the generation region. The results are shown in Fig. 5.4c, which contain the overlaid intensity profiles of harmonics 17, 21 and 25, at propagation distances that correspond to the apparent focus of each of these harmonics, for three different fundamental focus positions. For a laser focus position before the gas jet, the apparent focus positions of all harmonics are almost identical, and we find a small HHG source spot with a similar profile for all harmonics. Moving to a laser focus behind the gas jet, where a large chromatic aberration was measured, we also observe significant differences in the intensity profiles of the respective harmonics: when reconstructing the HHG beam at the apparent focus position of one specific harmonic, the other harmonics appear clearly defocused, and there is no single position where all harmonics have identical profiles. Further details and additional visualizations are provided in Appendix C. We previously already found that astigmatism transfers from the fundamental to the HHG beam in a wavelength-dependent way [147], which is also observed in the present beam reconstructions. We now conclude that dipole-phase-induced wavefront curvature also leads to significant chromatic aberration, and this effect would remain even for diffraction-limited beams.

To connect these experimental results to expectations, a model is needed that simulates the properties of HHG fields based on fundamental field properties. The analytical single-atom model described by Eqs. (5.1) and (5.2) gives an expression for the wavefront, but not the intensity distribution, limiting the options for direct numerical propagation. To find the apparent focus position, the single-atom model does allow for a determination of the radius of curvature through Eq. (5.2). By approximating the beam properties in a Gaussian model, assuming a Gaussian intensity profile and considering only quadratic phase profiles following the paraxial approximation, the focus position z of a beam can be calculated from the radius of curvature R and beam radius w at a given position along the beam propagation axis:

$$z_q = -\frac{R_q}{1 + \left(\lambda_q R_q / \pi w_q^2\right)^2}. \tag{5.3}$$

This Gaussian beam approach can be used when only HHG wavefront information is available, but does require an assumption for the waist of the generated HHG beam. In strong-field approximation (SFA) models, an effective nonlinearity m_{eff} is often assumed for plateau harmonics, resulting in a harmonic waist

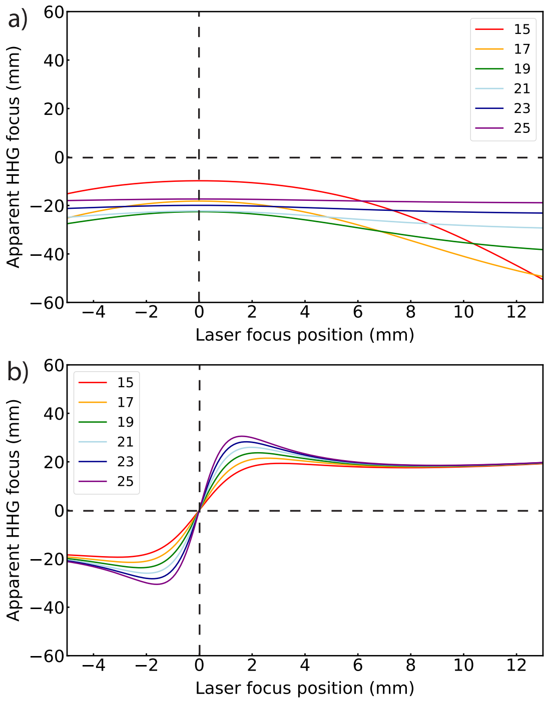

Figure 5.5: Relative contributions to the wavefront and the resulting focus of the HHG beams. a) The calculated apparent focus position only taking into account the dipole phase. b) The calculated apparent focus without dipole phase, only considering transfer of the fundamental wavefront to the harmonics. Note that even for this contribution only, a chromatic effect appears. This is the result of the chosen waist size of the harmonics, which we set as $w_{\mathrm{HHG}} = w_f(z)/\sqrt{m_{\mathrm{eff}}}$ as discussed in the text. For an HHG waist size that scales as $w_f(z)/\sqrt{q}$, this chromatic effect in the phase transfer disappears.

approximation as $w_{\mathrm{HHG}} = w_f(z)/\sqrt{m_{\mathrm{eff}}}$. For all our present single-atom model calculations we have taken $m_{\mathrm{eff}} = 4$. Further details about the procedure to reconstruct the HHG focus position from the measured fundamental field are given in Appendix A.

The high accuracy of the focus determination through ptychographic wavefront sensing enables a critical assessment of the dipole phase model. To this end, we calculate the single-atom model predictions using different approximations for the dipole phase, using the experimentally measured fundamental field as the starting point (Fig. 5.6). This field is numerically propagated to the gas jet plane, and its intensity and phase distributions serve as input to Eq. (5.1). This approach enables model predictions for astigmatic and otherwise aberrated beams, as often encountered experimentally. As the model does not include an estimate of the HHG efficiency, we assume Gaussian HHG intensity profiles when calculating the expected HHG focus position.

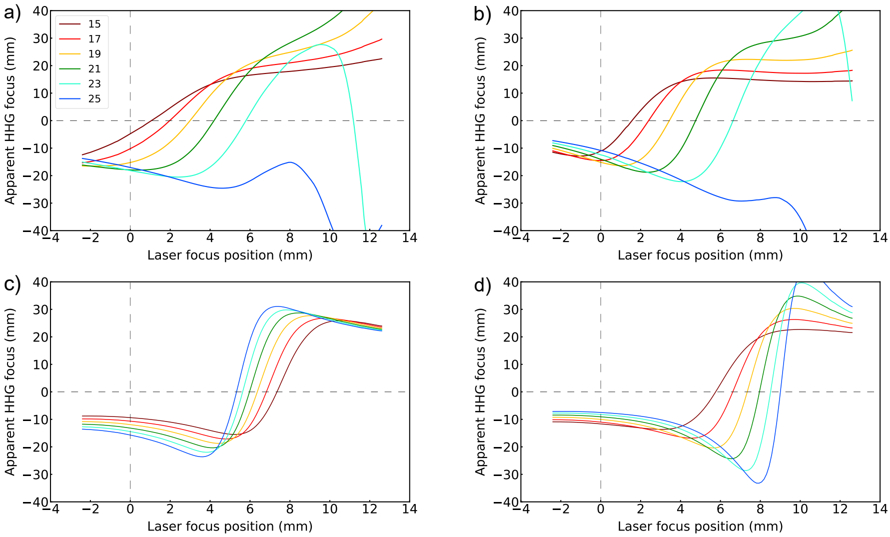

Figure 5.6: Expected wavelength-dependent HHG focusing properties for different dipole phase models, based on the experimentally measured fundamental field. a,b) Calculated a) horizontal and b) vertical focus positions using the $\Phi_i \sim \gamma/I$ model, using $\gamma = 0.9569 \times 10^{-18}$ s^2 W/cm^2. c) Calculation of horizontal focus positions using $\Phi_i \sim \alpha I$, taking a constant value $\alpha = -3 \times 10^{-14}$ cm^2/W. d) Model with $\Phi_i \sim \alpha I$, taking $\alpha \sim q^2$, increasing from -2.025×10^{-14} at $q = 15$ to -7.225×10^{-14} at $q = 25$.

Figures 5.6a and b show the result for the horizontal and vertical focus positions respectively using the model introduced by Guo et al. [30] and Wikmark et al. [137], based on an analytical derivation resulting in a $1/I-$dependence for the dipole phase. These calculations show a high degree of similarity with the experimental results in Fig. 5.4. In Figs. 5.6c,d we plot the results of the horizontal focus positions for two other commonly used approaches to model the dipole phase, based on a $\Phi_i \sim \alpha I$ relation, in which the factor α is either constant (Fig. 5.6c) or quadratically proportional to harmonic order (Fig. 5.6d). Note that in both cases, the values of α are chosen negative, to ensure that the dipole phase adds a diverging wavefront curvature as physically expected. For the model with constant α, the chromatic aberrations are markedly different from the experimental observations. Making α dependent on harmonic order leads to a qualitative improvement, but this model significantly underestimates the magnitude of the chromatic aberrations when the gas jet is close to the laser focus, and predict variations around positive laser-gas jet positions that are not commensurate with the experimental results.

From this comparison we conclude that the $\Phi_i \sim \gamma/I$ dipole phase model provides an accurate description of the atomic response in our experimental geometry with a thin jet. While nonlinear propagation and phase matching effects cannot be excluded, the close correspondence between the experimental results and simulations indicates that the observed chromatic effects are well-described by the single-atom response. Since our experiments are performed at high backing pressure, generating sufficient flux to collect the diffraction data needed in ptychographic imaging, self-focusing and plasma-induced defocusing should be considered. For our experimental parameters, we estimate a B-integral of 0.2, and an ionization level of 4% at the peak of the fundamental pulse. From these numbers we estimate that both self-focusing and plasma defocusing separately may lead to additional wavefront curvatures in the range $R \approx 5-10$ cm, and partially cancel as both effects have opposite signs. Such wavefront curvatures will not lead to significant shifts of the HHG foci, and are to first order wavelength-independent. Including such estimates in the calculations of Fig. 5.1b therefore only leads to a small horizontal shift of all the curves with respect to the laser focus position. Given the quantitative agreement between our single-atom calculations (Fig. 5.6a,b) and experimental observations (Fig. 5.4a,b), we conclude that for our parameters propagation-induced effects do not lead to significant modifications of the HHG focusing properties.

For HHG geometries with extended propagation length, more detailed simulations would be required for a quantitative analysis. However, the PWFS approach remains applicable to experimentally characterize the resulting chromatic effects in the HHG beam.

5.5 Conclusion

In conclusion, we have experimentally demonstrated that the wavefronts of the HHG EUV beams can strongly depend on the wavefront and intensity profile of the fundamental laser, as well as the wavelengths of the harmonics themselves. We confirm that the $1/I$-model for the dipole phase can be used for realistic predictions of HHG wavefronts if a measured fundamental laser field is available. Our findings provide guidance for experiments that aim to tightly focus broadband attosecond pulses, where the effects of intrinsic chromatic aberration in the HHG process should be minimized.

5.6 Appendix

5.6.1 Calculating HHG focus position from fundamental beam reconstructions

As stated before, having the measured detailed complex field information for both the fundamental and the HHG beams enables a direct comparison, taking the effect of aberrations in the fundamental beam into account [147]. For the model predictions we initially calculate the phase of the high harmonic field at each frequency $q\omega_l$ according to Eq. (5.1), where the driving laser phase and intensity are known from the ptychographic characterization of the beam at a wavelength close to the central laser wavelength of 830 nm. By numerically propagating the reconstructed wavefront over a range of positions around the focus, we can simulate the high harmonic generation conditions for the different positions of the focusing lens.

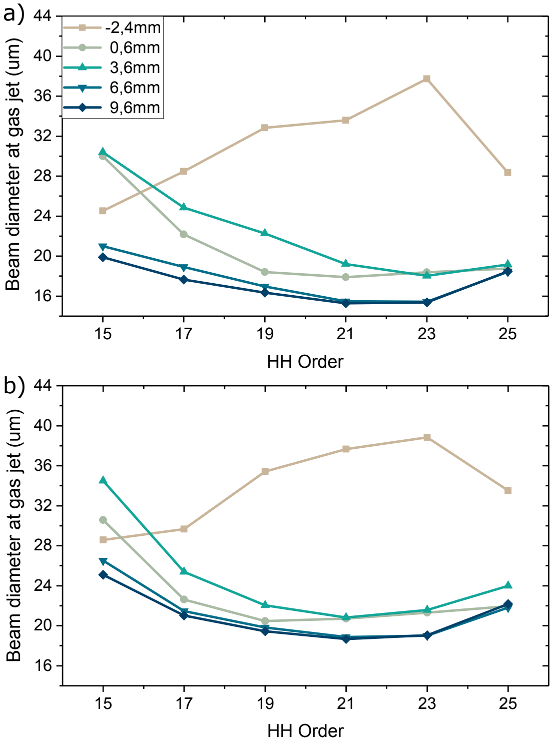

Figure 5.7: Beam diameter of the different harmonics at the gas jet position as reconstructed from the ptychography measurements, for various distances between the gas jet and the fundamental beam waist position. a) horizontal direction, b) vertical direction.

From the estimated phase of the high harmonic wavefronts, we calculate the radius of curvature at the horizontal and vertical directions though fitting a quadratic curve on the 1D wavefront cuts. The radius of curvature for each direction is then

$$R_{x/y} = \frac{k_q}{2a_{2,x/y}}, \tag{5.4}$$

where k_q is the propagation number of the harmonic q, and a_2 is the quadratic term of the fitting curve. The focal distance can then be calculated directly from the radius of curvature using Eq. (5.3), which we apply for the x- and y-directions separately, with the assumption that $w_{\mathrm{HHG}} = w_f(z)/\sqrt{m_{\mathrm{eff}}}$.

To facilitate the quadratic fitting near the saddle point of the fundamental beam, we apply the fit separately to the two phase contributions $\Phi_1 = q\phi$ and $\Phi_2 = \Phi_i$. From these fits we get two radii of curvature per direction $R_{1,x/y}$ and

$R_{2,x/y}$. The total radius of curvature then becomes:

$$R_{x/y} = (\frac{1}{R_{1,x/y}} + \frac{1}{R_{2,x/y}})^{-1}. \tag{5.5}$$

The results from this process are equivalent to the results obtained when we fit a quadratic curve to the total HHG wavefront directly.

For the results shown in Figs. 5.6 we used a peak intensity at the fundamental beam waist of 2.3 $\times 10^{14}$ W/cm^2. At different gas jet positions, the peak intensity is scaled inversely proportional to the increase of the beam size and numerically calculated.

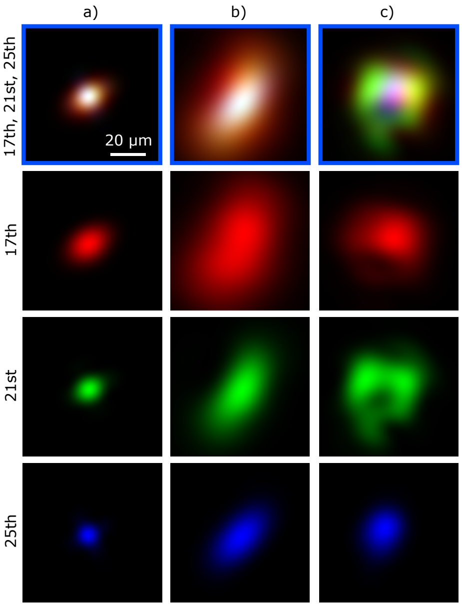

Figure 5.8: Reconstructed beam profiles of harmonics 17, 21 and 25, both overlaid (top row) and separated, at the plane where harmonic 25 has its apparent focus, for three different drive laser positions. The first row corresponds to the last row of Fig. 3 in the main text.

5.6.2 HHG beam diameters at the generation plane

As explained in the main text, the model used to estimate the intensity distribution of harmonics from a known fundamental field assumes a constant effective nonlinearity for plateau harmonics. Numerically propagating the measured harmonic fields to the source plane allows a verification of this assumption. From this data (Fig. 5.7), we actually find significant deviations from this SFA model waist assumption based on a constant effective nonlinearity. This discrepancy may limit the accuracy of a determination of the HHG wavefront based only on such model calculations, although we find that it does not change the conclusions for our experimental conditions.

5.6.3 Harmonic-resolved beam profile reconstructions

Figure 5.4c shows the reconstructed beam profiles of harmonics 17, 21 and 25 at different positions around the gas jet, for three different generation positions. In those figures, the different harmonics are overlaid as RGB color plots. To provide a more detailed decomposition, we separate the channels of the bottom row of Fig. 5.4c and plot them together in Fig. 5.8. These are the beam profiles of the respective harmonics, back-propagated to the position where harmonic 25 has its apparent focus. For the left column, which corresponds to a generation condition where the jet is positioned after the fundamental focus, little variation between the harmonics is observed and the spots are generally small. For conditions where the gas jet is placed before the laser focus (Fig. 5.8b,c), strong chromatic effects are observed. For large focus-jet separation (Fig. 5.8c), additional aberrations also become more apparent.

Acknowledgements

We acknowledge funding from the European Research Council (ERC-CoG 864016), the Netherlands Organisation for Scientific Research NWO through the LINX Perspectief Programme, and Laserlab-Europe (H2020 EC-GA 871124).

Summary

High harmonic generation (HHG) serves as a transformative gateway to the quantum dynamics of electrons, offering a unique perspective on the ultrafast processes that govern chemical and physical transformations at the atomic scale. By focusing intense laser pulses into a noble gas, we can coerce the gas's electrons into a nonlinear dancewhere they absorb multiple photons, tunnel through their atomic potentials, and re-emit this energy as they snap back to lower energy states, producing bursts of extreme ultraviolet (EUV) and soft X-ray radiation. Each burst, encapsulated in attosecond timescales, is a harmonic of the driving laser's frequency, unveiling a new realm of time-resolved spectroscopy and microscopy. This interaction not only underscores the fundamental aspects of light-matter interactions but also paves the way for revolutionary technological advancements in imaging and diagnostics, probing dynamics previously veiled by the limits of temporal resolution.

The focus of the second chapter is the application of HHG in coherent diffractive imaging (CDI), where the coherence and extreme ultraviolet wavelengths of HHG sources allow for imaging with high spatial resolution and chemical sensitivity. CDI, a lensless imaging technique, circumvents the resolution limits imposed by lens-based systems, exploiting the phase retrieval from diffraction patterns to reconstruct images of nanostructures and biological specimens. The unique properties of HHG-enhanced CDI lie in its ability to spectrally reconstruct the image of the object, providing a powerful tool for understanding the 3D structure of the object and its chemical composition. This chapter paves the way towards spectrally resolved ptychography.

In the third chapter, we propose the concept of spatial entropy minimization as a computational design principle for both mono- and polychromatic focusing optics. We show that spatial entropy minimization yields conventional ZPs for monochromatic radiation. For polychromatic radiation, we observe a previously unexplored class of diffractive optical elements (DOEs), allowing for balanced spectral efficiency. We apply the proposed approach to the design of a binary ZP, tailored to multispectral focusing of extreme ultraviolet (EUV) radiation from a high-harmonic table top source. The polychromatic focusing properties of these ZPs are experimentally confirmed using ptychography. This work provides a new route towards polychromatic wavefront engineering at EUV and soft-X-ray wavelengths. In this work, we also demonstrated the possibility of reconstructing multi-color images of the object, which could be used for EUV wavefront sensing.

The fourth chapter focus on the technical challenges and solutions associated with measuring and manipulating the wavefronts of high-order harmonic beams. Here we present a wavefront sensing solution based on multiplexed ptychography, with which we show spectrally-resolved, high-resolution beam reconstructions.using these high fidelity quantitative wavefront measurements, we investigate aberration transfer mechanisms in the high harmonic generation process, where we present and explain harmonic-order dependent astigmatism inheritance from the fundamental wavefront. This ptychographic wavefront sensing concept thus enables detailed studies of the high-harmonic generation process, such as spatiotemporal effects in attosecond pulse formation. The development of wavefront sensors tailored for the EUV spectrum plays a critical role in these improvements, enabling more precise and flexible control over the properties of attosecond light pulses.

The final chapter consolidates the chromatic aberrations inherent in the HHG process, highlighting their impact on the focusability and quality of generated beams across different harmonic orders. By systematically varying the generation conditions and employing sophisticated wavefront characterization techniques, we uncover the wavelength-dependent focusing properties of HHG beams. The insights gained from these studies are crucial for optimizing the generation and application of high harmonics in various scientific and technological arenas. We experimentally demonstrate and characterize these chromatic effects in high-harmonic generation by measuring the spectrally resolved high harmonic wavefronts as a function of generation conditions. We find that the high-harmonic generation process can have significant intrinsic chromatic aberration, particularly for converging incident laser fields. Furthermore, we identify regimes where chromatic effects can be minimized, and show that analytical single-atom models allow accurate predictions of harmonic wavefronts produced by a specific driving field.

Acknowledgments

Completing this thesis marks not only the end of my Ph.D. journey but also a significant chapter in my life, filled with wonder and excitement. During this time, I've encountered numerous challenges and joys that have deeply influenced both my academic and personal development. Reflecting on these years, they seem to have passed in the blink of an eye, yet every moment is a treasured memory.

I am profoundly grateful to the many individuals who have supported, guided, and inspired me throughout this process. Their steadfast support and invaluable contributions have been fundamental to my success and have greatly enriched my experience. I extend my sincere thanks to all of them.

Stefan, your mentorship was crucial in shaping my Ph.D. journey. You provided not only invaluable knowledge but also taught me the nuances of scientific thinking and demeanor. Your broad expertise and openness have been truly inspiring. Our discussions, whether about complex research topics or during lighthearted group lunches with your humorous stories, were immensely enriching. In times of challenge - moving to a new lab, troubleshooting a burnt post-amp, or addressing the peculiarities of a malfunctioning Yag rod - your encouragement and optimism guided me. Your belief in the power of perseverance, reminding us that "we can always try again tomorrow," has made a lasting impact. I am deeply grateful for your steadfast support and guidance, and proud of what we have accomplished together.

Kjeld, being neighbors in the lab has been nothing short of fortuitous. Your profound knowledge, infectious humor, and skill in demystifying complex concepts have been both admirable and inspirational. Your curiosity and clarity have been a continual source of learning for me.

Anne, starting our Ph.D.s around the same time, we've truly journeyed together. I vividly recall the day we spent alongside the post-amp, laboring to perfect the wavefront at each critical planes, it was intimidating due to the invisible high power laser beam yet thrilling with solid progress. Through frustrations and breakthroughs, your presence and thoughtful insights were invaluable. Your kindness and camaraderie have warmed my heart. Thanks for being there and helping me through difficult times.

Antonios, you joined the group later, but we have worked together for a long time when you started working with our HHG setup, I believe we have formed a strong bound by fighting the bad lucks when the setup gave us some tough time, but we encouraged and helped each other, exploring and moving forward together. In the end, we achieved the desired results with the chromatic aberration project, and I am proud of what we have accomplished.

Fengling, you learned how to operate the setup and how to prepare samples with focused ion beam very quickly, you very soon became a significant part of the HHG team, you are very responsible and conscientious. Thank you for helping with all the measurements that took a lot of time, and also thank you for those wonderful dinners.

Jan, I cannot remember for how many times, I went to your lab to ask for help, you never turned me down. Your willingness to assist, even during the demanding final phases of our Ph.D.s, was invaluable. Thank you for the fruitful discussions in the office and thank you for the games at home.

Matthijs, you introduced the HHG setup to me and you taught many programming techniques to me. I learned from you how to work with our high power laser system, and learned how to ”make things work”, funny enough that sometimes this is not as easy as it sounded. All projects that we did together were very much enjoyable, wavefront sensing at Lund, DSI with a very complex VU logo sample, and the dispersion measurement. Oh, and steaming the CCD camera with flammable solvent. All these are beautiful memories.

Lars L.,thank you for bringing ptychography, which became a significant component of my PhD work, and for showing me the impressive foosball tricks. It was a great pleasure to work with you. I greatly admire your extensive knowledge and your relentless passion for progress.

Maisie, you encourage me to join Stefan’s group on a conference, and introduced me to the group and made me feel welcome. I am sincerely grateful to the various help you lend to me. Also thank you for inviting me and Qian over for the delicious food and games. It meant a lot to me.

Matthias, Matthijs V., Maksym, thank you guys for sharing brilliant ideas during group meetings which definitely helped my projects.

Lars F. it was a great pleasure to have worked together with you, thank you for teaching me how to use FIB. And thank you for standing by my side in the brutal fights in MORDHAU.

Nik, thank you for your support, it was more than necessary. The solutions you came up with was always solid and robust. Thank you for always being ready to help.

I would like to thank all other members of the EUV Generation and Imaging group, for the fruitful discussion, advises on experiments, and making the time so enjoyable at ARCNL. I would like to mention Ale, Zeudi, Amelie, Hao, Dirk. You all provided help to me in one way or another. Aside from helping me with Ph.D work, you also helped me out when I had car accident in Italy, or shared many useful tips for job hunting, it was truly heart warming memories.

Christos, thanks for your patients at me when we had the TA task and I got frustrated at my own solutions for the exercise at the black board, and thank you for the wavefront reconstruction attempt using your code.

Yu, Lianjia, Sonia, Aniket, Adrian and Jarich, thank you for being there during my internship times at ARCNL. Your warm welcomes will never be forgotten.

And Sonia, thanks for the basket ball!

Niklas, thanks for inviting me to ARCNL for the internship and offering me the PhD position.

I should also mention Arend-Jan from contact dynamics, for helping me solving many vacuum system questions. And Bob, Adries Lof, Dimitri from Amolf, you were the heroes of the AMOLF nano center.

Joost and Marjan, thank you for giving me invaluable support during the re-organizing of the research group. Thank you for making sure the transition of me went smooth.

Life could not have been this cherished without all my friends. I am honored to have all of you around me. Che Huilu, Chen Yicheng, Liu Bo, Liu Shuo, Lu Shan, Shen Shiyu, Wang Zhe, Wang Xin, Xiao Chen, Zhonghui, Zozo, I am sure I must have missed someone here, but thanks to all of you, for making the life so vibrate, for all the dinners, fun games, sports, and all the interesting conversations. I am grateful for having all of you and happy that our path crossed.

I would also like to take this opportunity to thank Xiaohan, my dearest friend, who encouraged me to venture abroad and provided invaluable support countless times along the way. As I complete this thesis, marking an important milestone, I want to express my deepest gratitude to you. Thank you for teaching me so many things, and thank you for all the ski trips, bike trips, and all the phone calls. Thank you for always being there.

I want to thank my parents. Dad, you were like my first physics teacher. I still remember you explaining the Rutherford atomic model to me when I was 10. While I could barely understand all the terms at the time, the idea of particles passing through gold foil and some bouncing back sparked my fascination with physics. You helped me step out of my comfort zone when I was 16, encouraged me when things seemed stuck at 24, and supported me tremendously when I decided to go to the Netherlands for my master's studies. This thesis would never have been possible without you. Mom, you taught me how to read, how to count, how to make friends at school, and how to solve chemistry problems. Pushing me to explore the world must not have been easy for you, thanks for this deepest love. Thank you for your belief in my potential, it empowers me with boundless courage to forge ahead.

Qian, you have been my steadfast companion throughout almost my entire journey abroad. Countless have been the nights when I toiled until late, yet never once did I feel alone. Your enduring encouragement, gentle consolations, and unwavering support in moments of doubt and despair have guided me back to my path. Thank you for everything you have illuminated in my life.

-Xiaomeng

Bibliography

[1] A. Shadfan, M. Pawlowski, Y. Wang, K. Subramanian, I. Gabay, A. Ben-Yakar, and T. Tkaczyk, *Design and fabrication of a miniature objective consisting of high refractive index zinc sulfide lenses for laser surgery*, Optical Engineering **55**(2):025107–025107 (2016). 9

[2] P. V. Parimi, W. T. Lu, P. Vodo, and S. Sridhar, *Imaging by flat lens using negative refraction*, Nature **426**(6965):404–404 (2003). 9

[3] S. W. Hell and J. Wichmann, *Breaking the diffraction resolution limit by stimulated emission: stimulated-emission-depletion fluorescence microscopy*, Optics Letters **19**(11):780–782 (1994). 9

[4] J. Miao, P. Charalambous, J. Kirz, and D. Sayre, *Extending the methodology of X-ray crystallography to allow imaging of micrometre-sized non-crystalline specimens*, Nature **400**(6742):342–344 (1999). 9, 10, 11, 14

[5] S. Marchesini, H. Chapman, S. Hau-Riege, R. London, A. Szoke, H. He, M. Howells, H. Padmore, R. Rosen, J. Spence, *et al.*, *Coherent X-ray diffractive imaging: applications and limitations*, Optics Express **11**(19):2344–2353 (2003). 9

[6] J. W. Goodman, *Introduction to Fourier optics*, Roberts and Company Publishers (2005). 10

[7] J. R. Fienup, *Phase retrieval algorithms: a comparison*, Applied Optics **21**(15):2758–2769 (1982). 11

[8] J. M. Rodenburg and H. M. Faulkner, *A phase retrieval algorithm for shifting illumination*, Applied Physics Letters **85**(20):4795–4797 (2004). 11

[9] J. Miao, J. Kirz, and D. Sayre, *The oversampling phasing method*, Acta Crystallographica Section D: Biological Crystallography **56**(10):1312–1315 (2000). 11

[10] A. M. Maiden and J. M. Rodenburg, *An improved ptychographical phase retrieval algorithm for diffractive imaging*, Ultramicroscopy **109**(10):1256–1262 (2009). 12

[11] R. L. Sandberg, A. Paul, D. A. Raymondson, S. Hädrich, D. M. Gaudiosi, J. Holtsnider, I. T. Raanan, O. Cohen, M. M. Murnane, H. C. Kapteyn, *et al.*, *Lensless diffractive imaging using tabletop coherent high-harmonic soft-x-ray beams*, Physical Review Letters **99**(9):098103 (2007). 14, 23, 72

[12] A. Rundquist, C. G. Durfee III, Z. Chang, C. Herne, S. Backus, M. M. Murnane, and H. C. Kapteyn, *Phase-matched generation of coherent soft X-rays*, Science **280**(5368):1412–1415 (1998). 14, 23

[13] A. McPherson, G. Gibson, H. Jara, U. Johann, T. S. Luk, I. McIntyre, K. Boyer, and C. K. Rhodes, *Studies of multiphoton production of vacuum-ultraviolet radiation in the rare gases*, Journal of the Optical Society of America B **4**(4):595–601 (1987). 14, 23

[14] P. B. Corkum, *Plasma perspective on strong field multiphoton ionization*, Physical review letters **71**(13):1994 (1993). 14, 72

[15] J. L. Krause, K. J. Schafer, and K. C. Kulander, *High-order harmonic generation from atoms and ions in the high intensity regime*, Physical Review Letters **68**(24):3535 (1992). 14

[16] M. V. Ammosov, N. B. Delone, and V. P. Krainov, *Tunnel ionization of complex atoms and of atomic ions in an alternating electromagnetic field*, Soviet Journal of Experimental and Theoretical Physics **64**(6):1191 (1986). 14

[17] Y. Mairesse, A. De Bohan, L. Frasinski, H. Merdji, L. Dinu, P. Monchicourt, P. Breger, M. Kovacev, R. Taïeb, B. Carré, *et al.*, *Attosecond synchronization of high-harmonic soft x-rays*, Science **302**(5650):1540–1543 (2003). 14, 17, 72

[18] F. Krausz and M. Ivanov, *Attosecond physics*, Reviews of modern physics **81**(1):163 (2009). 14, 72

[19] P.-M. Paul, E. S. Toma, P. Breger, G. Mullot, F. Augé, P. Balcou, H. G. Muller, and P. Agostini, *Observation of a train of attosecond pulses from high harmonic generation*, Science **292**(5522):1689–1692 (2001). 14, 72

[20] M. Lewenstein, P. Balcou, M. Y. Ivanov, A. L'Huillier, and P. B. Corkum, *Theory of high-harmonic generation by low-frequency laser fields*, Physical Review A **49**:2117–2132 (1994). 15, 17, 72, 73

[21] G. S. M. Jansen, A. de Beurs, X. Liu, K. S. E. Eikema, and S. Witte, *Diffractive shear interferometry for extreme ultraviolet high-resolution lensless imaging*, Optics Express **26**(10):12479–12489 (2018). 16, 23, 24, 26, 72

[22] R. Zerne, C. Altucci, M. Bellini, M. B. Gaarde, T. Hänsch, A. L'Huillier, C. Lyngå, and C.-G. Wahlström, *Phase-locked high-order harmonic sources*, Physical Review Letters **79**(6):1006 (1997). 16

[23] R. A. Bartels, A. Paul, H. Green, H. C. Kapteyn, M. M. Murnane, S. Backus, I. P. Christov, Y. Liu, D. Attwood, and C. Jacobsen, *Generation of spatially coherent light at extreme ultraviolet wavelengths*, Science **297**(5580):376–378 (2002). 16

[24] T. Popmintchev, M.-C. Chen, A. Bahabad, M. Gerrity, P. Sidorenko, O. Cohen, I. P. Christov, M. M. Murnane, and H. C. Kapteyn, *Phase matching of high harmonic generation in the soft and hard X-ray regions of the spectrum*, Proceedings of the National Academy of Sciences **106**(26):10516–10521 (2009). 17

[25] H. Wikmark, C. Guo, J. Vogelsang, P. W. Smorenburg, H. Coudert-Alteirac, J. Lahl, J. Peschel, P. Rudawski, H. Dacasa, S. Carlström, S. MacLot, M. B. Gaarde, P. Johnsson, C. L. Arnold, and A. L'Huillier, *Spatiotemporal coupling of attosecond pulses*, Proceedings of the National Academy of Sciences of the United States of America **116**(11):4779–4787

(2019). `1810.06462`. 17, 54

[26] P. Balcou, P. Salieres, A. L'Huillier, and M. Lewenstein, *Generalized phase-matching conditions for high harmonics: The role of field-gradient forces*, Physical Review A **55**(4):3204 (1997). 17

[27] A. H. Zewail, *Femtochemistry: Atomic-scale dynamics of the chemical bond*, The Journal of Physical Chemistry A **104**(24):5660–5694 (2000). 17, 72

[28] E. Goulielmakis, Z.-H. Loh, A. Wirth, R. Santra, N. Rohringer, V. S. Yakovlev, S. Zherebtsov, T. Pfeifer, A. M. Azzeer, M. F. Kling, *et al.*, *Real-time observation of valence electron motion*, Nature **466**(7307):739–743 (2010). 17, 72

[29] C. Bourassin-Bouchet, M. M. Mang, F. Delmotte, P. Chavel, and S. De Rossi, *How to focus an attosecond pulse*, Optics Express **21**(2):2506–2520 (2013). 17, 72

[30] C. Guo, A. Harth, S. Carlström, Y.-C. Cheng, S. Mikaelsson, E. Mårsell, C. Heyl, M. Miranda, M. Gisselbrecht, M. B. Gaarde, *et al.*, *Phase control of attosecond pulses in a train*, Journal of Physics B: Atomic, Molecular and Optical Physics **51**(3):034006 (2018). 17, 73, 81

[31] M. Lewenstein, P. Salires, and A. L'Huillier, *Phase of the atomic polarization in high-order harmonic generation*, Physical Review A **52**(6):4747–4754 (1995). 17, 73

[32] U. Keller, *Recent developments in compact ultrafast lasers*, Nature **424**(6950):831–838 (2003). 18

[33] S. Witte and K. S. E. Eikema, *Ultrafast optical parametric chirped-pulse amplification*, IEEE Journal of Selected Topics in Quantum Electronics **18**(1):296–307 (2011). 19, 20

[34] G. Cerullo and S. De Silvestri, *Ultrafast optical parametric amplifiers*, Review of Scientific Instruments **74**(1):1–18 (2003). 19

[35] D. W. E. Noom, S. Witte, J. Morgenweg, R. K. Altmann, and K. S. E. Eikema, *High-energy, high-repetition-rate picosecond pulses from a quasi-CW diode-pumped Nd:YAG system*, Optics Letters **38**(16):3021–3023 (2013). 19

[36] D. Attwood, *Soft x-rays and extreme ultraviolet radiation: principles and applications*, Cambridge University Press (2000). 23

[37] M. Ferray, A. L'Huillier, X. Li, L. Lompre, G. Mainfray, and C. Manus, *Multiple-harmonic conversion of 1064 nm radiation in rare gases*, Journal of Physics B: Atomic, Molecular and Optical Physics **21**(3):L31 (1988). 23

[38] S. Witte, V. T. Tenner, D. W. E. Noom, and K. S. E. Eikema, *Lensless diffractive imaging with ultra-broadband table-top sources: from infrared to extreme-ultraviolet wavelengths*, Light: Science & Applications **3**(3):e163–e163 (2014). 23

[39] G. S. M.Jansen, X. Liu, K. S. E. Eikema, and S. Witte, *Broadband extreme ultraviolet dispersion measurements using a high-harmonic source*, Optics Letters **44**(15):3625–3628 (2019). 23

[40] R. Bell, *Introductory Fourier transform spectroscopy*, Elsevier (2012). 23

[41] A. de Beurs, X. Liu, G. S. M. Jansen, K. S. E. Eikema, and S. Witte, *Rotational diffractive shear interferometry for extreme ultraviolet imaging*

(2019). 23

[42] M. Abd Mutalib, M. Rahman, M. Othman, A. Ismail, and J. Jaafar, *Scanning electron microscopy (SEM) and energy-dispersive X-ray (EDX) spectroscopy*, in *Membrane characterization*, pp. 161–179, Elsevier (2017). 26

[43] M. Williams, B. Thomas, J. Farrar, and C. Pollock, *Visualizing the distribution of elements within barley leaves by energy dispersive X-ray image maps (EDX maps)*, New Phytologist **125**(2):367–372 (1993). 26

[44] B. L. Henke, E. M. Gullikson, and J. C. Davis, *X-ray interactions: photoabsorption, scattering, transmission, and reflection at E= 50-30,000 eV, Z= 1-92*, Atomic data and nuclear data tables **54**(2):181–342 (1993). 27

[45] J. M. Rodenburg, A. Hurst, A. G. Cullis, B. R. Dobson, F. Pfeiffer, O. Bunk, C. David, K. Jefimovs, and I. Johnson, *Hard-x-ray lensless imaging of extended objects*, Physical review letters **98**(3):034801 (2007). 29

[46] M. D. Seaberg, B. Zhang, D. F. Gardner, E. R. Shanblatt, M. M. Murnane, H. C. Kapteyn, and D. E. Adams, *Tabletop nanometer extreme ultraviolet imaging in an extended reflection mode using coherent Fresnel ptychography*, Optica **1**(1):39–44 (2014). 29

[47] M. Wieland, C. Spielmann, U. Kleineberg, T. Westerwalbesloh, U. Heinzmann, and T. Wilhein, *Toward time-resolved soft X-ray microscopy using pulsed fs-high-harmonic radiation*, Ultramicroscopy **102**(2):93–100 (2005). 32

[48] G. Vaschenko, C. Brewer, F. Brizuela, Y. Wang, M. A. Larotonda, B. M. Luther, M. C. Marconi, J. J. Rocca, C. S. Menoni, E. H. Anderson, W. Chao, B. D. Harteneck, J. A. Liddle, Y. Liu, and D. T. Attwood, *Sub-38 nm resolution tabletop microscopy with 13 nm wavelength laser light*, Optics Letters **31**(9):1214 (2006). 32

[49] S. J. Bennett, *Achromatic combinations of hologram optical elements*, Applied Optics **15**(2):542 (1976). 32, 54

[50] I. Weingärtner, *Real and achromatic imaging with two planar holographic optical elements*, Optics Communications **58**(6):385–388 (1986). 32, 54

[51] D. Paganin, *Coherent X-Ray Optics*, Oxford University Press, 1st edn. (2006). 32, 39

[52] G. S. M. Jansen, X. Liu, K. S. E. Eikema, and S. Witte, *Broadband extreme ultraviolet dispersion measurements using a high-harmonic source*, Optics Letters **44**(15):3625 (2019). 32

[53] J. Miao, P. Charalambous, and J. Kirz, *Extending the methodology of X-ray crystallography to allow imaging of micrometre-sized non-crystalline specimens*, Nature **400**:342–344 (1999). 32

[54] R. L. Sandberg, A. Paul, D. A. Raymondson, S. Hädrich, D. M. Gaudiosi, J. Holtsnider, R. I. Tobey, O. Cohen, M. M. Murnane, H. C. Kapteyn, C. Song, J. Miao, Y. Liu, and F. Salmassi, *Lensless diffractive imaging using tabletop coherent high-harmonic soft-X-ray beams*, Physical Review Letters **99**(9):098103 (2007). 32

[55] J. R. Fienup, *Reconstruction of an object from the modulus of its Fourier transform*, Optics Letters **3**(1):27 (1978). 32

[56] S. Marchesini, H. He, H. N. Chapman, S. P. Hau-Riege, A. Noy, M. R.

Howells, U. Weierstall, and J. C. H. Spence, *X-ray image reconstruction from a diffraction pattern alone*, Physical Review B **68**(14):140101 (2003). 32

[57] T. Ditmire, E. T. Gumbrell, R. A. Smith, J. W. Tisch, D. D. Meyerhofer, and M. H. Hutchinson, *Spatial coherence measurement of soft x-ray radiation produced by high order harmonic generation*, Physical Review Letters **77**(23):4756–4759 (1996). 32

[58] R. Zerne, C. Altucci, M. Bellini, M. B. Gaarde, T. W. Hänsch, A. L'huillier, C. Lyngå, and C. G. Wahlström, *Phase-locked high-order harmonic sources*, Physical Review Letters **79**(6):1006–1009 (1997). 32

[59] R. A. Bartels, A. Paul, H. Green, H. C. Kapteyn, M. M. Murnane, S. Backus, I. P. Christov, Y. Liu, D. Attwood, and C. Jacobsen, *Generation of Spatially Coherent Light at Extreme Ultraviolet Wavelengths*, Science **297**(5580):376–378 (2002). 32

[60] B. Abbey, L. W. Whitehead, H. M. Quiney, D. J. Vine, G. A. Cadenazzi, C. A. Henderson, K. A. Nugent, E. Balaur, C. T. Putkunz, A. G. Peele, G. J. Williams, and I. McNulty, *Lensless imaging using broadband X-ray sources*, Nature Photonics **5**(7):420–424 (2011). 32

[61] J. Huijts, S. Fernandez, D. Gauthier, M. Kholodtsova, A. Maghraoui, K. Medjoubi, A. Somogyi, W. Boutu, and H. Merdji, *Broadband coherent diffractive imaging*, Nature Photonics **14**(10):618–622 (2020). 32

[62] S. Witte, V. T. Tenner, D. W. E. Noom, and K. S. E. Eikema, *Lensless diffractive imaging with ultra-broadband table-top sources: from infrared to extreme-ultraviolet wavelengths*, Light: Science & Applications **3**(3):e163 (2014). 32

[63] R. Früke, J. Kutzner, T. Witting, H. Zacharias, and T. Wilhein, *EUV scanning transmission microscope operating with high-harmonic and laser plasma radiation*, EPL (Europhysics Letters) **72**(6):915 (2005). 32

[64] H. Coudert-Alteirac, H. Dacasa, F. Campi, E. Kueny, B. Farkas, F. Brunner, S. Maclot, B. Manschwetus, H. Wikmark, J. Lahl, L. Rading, J. Peschel, B. Major, K. Varjú, G. Dovillaire, *et al.*, *Micro-Focusing of Broadband High-Order Harmonic Radiation by a Double Toroidal Mirror*, Applied Sciences **7**(11):1159 (2017). 32

[65] J. M. Rodenburg and H. M. L. Faulkner, *A phase retrieval algorithm for shifting illumination*, Applied Physics Letters **85**(20):4795 – 4797 (2004). 32, 57

[66] J. Rodenburg and A. Maiden, *Ptychography*, in *Springer Handbook of Microscopy*, pp. 2–2, Springer (2019). 32

[67] P. Thibault, M. Dierolf, A. Menzel, O. Bunk, C. David, and F. Pfeiffer, *High-Resolution Scanning X-ray Diffraction Microscopy*, Science **321**(5887):379–382 (2008). 32, 57

[68] M. D. Seaberg, B. Zhang, D. F. Gardner, E. R. Shanblatt, M. M. Murnane, H. C. Kapteyn, and D. E. Adams, *Tabletop nanometer extreme ultraviolet imaging in an extended reflection mode using coherent Fresnel ptychography*, Optica **1**(1):39 (2014). `1312.2049`. 32, 33

[69] M. Du, L. Loetgering, K. S. E. Eikema, and S. Witte, *Measuring laser*

beam quality, wavefronts, and lens aberrations using ptychography, Optics Express **28**(4):5022–5034 (2020). 32

[70] D. J. Batey, D. Claus, and J. M. Rodenburg, *Information multiplexing in ptychography*, Ultramicroscopy **138**:13–21 (2014). 33, 42, 43, 51, 53, 57, 60

[71] A. Rana, J. Zhang, M. Pham, A. Yuan, Y. H. Lo, H. Jiang, S. J. Osher, and J. Miao, *Potential of Attosecond Coherent Diffractive Imaging*, Physical Review Letters **125**(8):086101 (2020). 33, 53

[72] P. D. Baksh, M. Odstrčil, H.-S. Kim, S. A. Boden, J. G. Frey, and W. S. Brocklesby, *Wide-field broadband extreme ultraviolet transmission ptychography using a high-harmonic source*, Optics Letters **41**(7):1317 (2016). 33

[73] C. L. Porter, M. Tanksalvala, M. Gerrity, G. Miley, X. Zhang, C. Bevis, E. Shanblatt, R. Karl, M. M. Murnane, D. E. Adams, and H. C. Kapteyn, *General-purpose, wide field-of-view reflection imaging with a tabletop 13 nm light source*, Optica **4**(12):1552 (2017). 33

[74] J. Rothhardt, G. K. Tadesse, W. Eschen, and J. Limpert, *Table-top nanoscale coherent imaging with XUV light*, Journal of Optics **20**(11):113001 (2018). 33

[75] G. K. Tadesse, W. Eschen, R. Klas, M. Tschernajew, F. Tuitje, M. Steinert, M. Zilk, V. Schuster, M. Zürch, T. Pertsch, C. Spielmann, J. Limpert, and J. Rothhardt, *Wavelength-scale ptychographic coherent diffractive imaging using a high-order harmonic source*, Scientific Reports **9**(1):1–7 (2019). `1805.09588`. 33

[76] P. D. Baksh, M. Ostrčil, M. Miszczak, C. Pooley, R. T. Chapman, A. S. Wyatt, E. Springate, J. E. Chad, K. Deinhardt, J. G. Frey, and W. S. Brocklesby, *Quantitative and correlative extreme ultraviolet coherent imaging of mouse hippocampal neurons at high resolution*, Science Advances **6**(18):eaaz3025 (2020). 33

[77] B. Zhang, D. F. Gardner, M. H. Seaberg, E. R. Shanblatt, C. L. Porter, R. Karl, C. A. Mancuso, H. C. Kapteyn, M. M. Murnane, and D. E. Adams, *Ptychographic hyperspectral spectromicroscopy with an extreme ultraviolet high harmonic comb*, Optics Express **24**(16):18745–18754 (2016). 33

[78] A. M. Maiden, M. J. Humphry, F. Zhang, and J. M. Rodenburg, *Superresolution imaging via ptychography.*, Journal of the Optical Society of America A **28**(4):604–612 (2011). 33, 48

[79] M. Guizar-Sicairos, M. Holler, A. Diaz, J. Vila-Comamala, O. Bunk, and A. Menzel, *Role of the illumination spatial-frequency spectrum for ptychography*, Physical Review B **86**(10):100103 (2012). 33, 46, 48

[80] M. Odstrčil, M. Lebugle, M. Guizar-Sicairos, C. David, and M. Holler, *Towards optimized illumination for high-resolution ptychography*, Optics Express **27**(10):14981 (2019). 33, 48

[81] L. Loetgering, M. Baluktsian, K. Keskinbora, R. Horstmeyer, T. Wilhein, G. Schütz, K. S. E. Eikema, and S. Witte, *Generation and characterization of focused helical x-ray beams*, Science Advances **6**(7):eaax8836 (2020). 33, 39, 48, 49

[82] R. B. Ash, *Information Theory*, Dover, New York, 1 edn. (1990). 35

[83] K. Kreutz-Delgado, *The Complex Gradient Operator and the CR-Calculus*, arXiv:0906.4835 (2009). `0906.4835`. 35

[84] K. Matsushima and T. Shimobaba, *Band-limited angular spectrum method for numerical simulation of free-space propagation in far and near fields.*, Optics express **17**(22):19662–19673 (2009). 36

[85] J. W. Goodman, *Introduction to Fourier Optics*, WH Freeman, 4th edn. (2017). 40, 43, 48

[86] J. Schmidt, *Numerical Simulation of Optical Wave Propagation With Examples in MATLAB*, SPIE Press, Bellingham, 1 edn. (2010). 42, 43

[87] A. Maiden, D. Johnson, and P. Li, *Further improvements to the ptychographical iterative engine*, Optica **4**(7):736 (2017). 42

[88] B. Enders and P. Thibault, *A computational framework for ptychographic reconstructions*, Proceedings of the Royal Society A: Mathematical, Physical and Engineering Sciences **472**(2196):20160640 (2016). 42

[89] G. Parry, *Some effects of surface roughness on the appearance of speckle in polychromatic light*, Optics Communications **12**(1):75–78 (1974). 47

[90] S. L. Jacques, *Optical properties of biological tissues: A review*, Physics in Medicine and Biology **58**(11) (2013). 48

[91] J. Miao, D. Sayre, and H. N. Chapman, *Phase retrieval from the magnitude of the Fourier transforms of nonperiodic objects*, Journal of the Optical Society of America A **15**(6):1662–1669 (1998). 48

[92] L. Freisem, G. S. M. Jansen, D. Rudolf, K. S. E. Eikema, and S. Witte, *Spectrally resolved single-shot wavefront sensing of broadband high-harmonic sources*, Optics Express **26**(6):6860 (2018). 50, 51

[93] F. Tuitje, W. Eschen, G. K. Tadesse, J. Limpert, J. Rothhardt, and C. Spielmann, *Reliability of ptychography on periodic structures*, OSA Continuum **3**(6):1691–1702 (2020). 49

[94] O. Bunk, M. Dierolf, S. Kynde, I. Johnson, O. Marti, and F. Pfeiffer, *Influence of the overlap parameter on the convergence of the ptychographical iterative engine.*, Ultramicroscopy **108**(5):481–487 (2008). 51

[95] J. Durnin, *Exact solutions for nondiffracting beams. I. The scalar theory*, Journal of the Optical Society of America A **4**(4):651 (1987). 53

[96] S. Akturk, X. Gu, P. Bowlan, and R. Trebino, *Spatio-temporal couplings in ultrashort laser pulses*, Journal of Optics **12**(9) (2010). 54, 72

[97] H. Dacasa, H. Coudert-Alteirac, C. Guo, E. Kueny, F. Campi, J. Lahl, J. Peschel, H. Wikmark, B. Major, E. Malm, D. Alj, K. Varjú, C. L. Arnold, G. Dovillaire, P. Johnsson, *et al.*, *Single-shot extreme-ultraviolet wavefront measurements of high-order harmonics*, Optics Express **27**(3):2656 (2019). 54

[98] M. Ferray, A. L'Huillier, X. F. Li, L. A. Lompre, G. Mainfray, and C. Manus, *Multiple-harmonic conversion of 1064 nm radiation in rare gases*, Journal of Physics B: Atomic, Molecular and Optical Physics **21**(3):L31–L35 (1988). 56

[99] R. Bartels, A. Paul, H. Green, H. C. Kapteyn, M. M. Murnane, S. Backus, I. Christov, Y. Liu, D. Attwood, and C. Jacobsen, *Generation of spatially coherent light at extreme ultraviolet wavelengths*, Science **297**:376–378

(2002). 56

[100] M. Zürch, J. Rothhardt, S. Hädrich, S. Demmler, M. Krebs, J. Limpert, A. Tünnermann, A. Guggenmos, U. Kleineberg, and C. Spielmann, *Real-time and sub-wavelength ultrafast coherent diffraction imaging in the extreme ultraviolet*, Scientific reports **4**(1):7356 (2014). 56

[101] E. R. Shanblatt, C. L. Porter, D. F. Gardner, G. F. Mancini, R. M. Karl, M. D. Tanksalvala, C. S. Bevis, V. H. Vartanian, H. C. Kapteyn, D. E. Adams, and M. M. Murnane, *Quantitative Chemically Specific Coherent Diffractive Imaging of Reactions at Buried Interfaces with Few Nanometer Precision*, Nano Letters **16**(9):5444–5450 (2016). 56

[102] M. Tanksalvala, C. L. Porter, Y. Esashi, B. Wang, N. W. Jenkins, Z. Zhang, G. P. Miley, J. L. Knobloch, B. McBennett, N. Horiguchi, S. Yazdi, J. Zhou, M. N. Jacobs, C. S. Bevis, R. M. Karl, *et al.*, *Nondestructive, high-resolution, chemically specific 3D nanostructure characterization using phase-sensitive EUV imaging reflectometry*, Science Advances **7**(5):eabd9667 (2021). 56

[103] P. á. Corkum and F. Krausz, *Attosecond science*, Nature physics **3**(6):381–387 (2007). 56

[104] J. Li, J. Lu, A. Chew, S. Han, J. Li, Y. Wu, H. Wang, S. Ghimire, and Z. Chang, *Attosecond science based on high harmonic generation from gases and solids*, Nature Communications **11**:2748 (2020). 56

[105] F. Sanson, A. K. Pandey, I. Papagiannouli, F. Harms, G. Dovillaire, E. Baynard, J. Demailly, O. Guilbaud, B. Lucas, O. Neveu, M. Pittman, D. Ros, M. Richardson, E. Johnson, W. Li, *et al.*, *Highly multimodal structure of high topological charge extreme ultraviolet vortex beams*, Optics letters **45**(17):4790–4793 (2020). 56

[106] A. K. Pandey, A. de las Heras, T. Larrieu, J. San Romn, J. Serrano, L. Plaja, E. Baynard, M. Pittman, G. Dovillaire, S. Kazamias, C. Hernndez-Garca, and O. Guilbaud, *Characterization of Extreme Ultraviolet Vortex Beams with a Very High Topological Charge*, ACS Photonics **9**(3):944–951 (2022). 56

[107] L. Quintard, V. Strelkov, J. Vabek, O. Hort, A. Dubrouil, D. Descamps, F. Burgy, C. Pjot, E. Mvel, F. Catoire, and E. Constant, *Optics-less focusing of XUV high-order harmonics*, Science Advances **5**(4):eaau7175 (2019). 56, 61

[108] M. Hoflund, J. Peschel, M. Plach, H. Dacasa, K. Veyrinas, E. Constant, P. Smorenburg, H. Wikmark, S. Maclot, C. Guo, C. Arnold, A. L'Huillier, and P. Eng-Johnsson, *Focusing Properties of High-Order Harmonics*, Ultrafast Science **2021**:9797453 (2021). 56

[109] L. Loetgering, X. Liu, A. C. C. D. Beurs, M. Du, G. Kuijper, K. S. E. Eikema, and S. Witte, *Tailoring spatial entropy in extreme ultraviolet focused beams for multispectral ptychography*, Optica **8**(2):130–138 (2021). 56, 57

[110] P. Mercère, P. Zeitoun, M. Idir, S. L. Pape, D. Douillet, X. Levecq, G. Dovillaire, S. Bucourt, K. A. Goldberg, P. P. Naulleau, and S. Rekawa, *Hartmann wave-front measurement at 13.4 nm with λEUV/120 accuracy*, Optics Let-

ters **28**(17):1534–1536 (2003). 56, 74

[111] C. Valentin, J. Gautier, J.-P. Goddet, C. Hauri, T. Marchenko, E. Papalazarou, G. Rey, S. Sebban, O. Scrick, P. Zeitoun, G. Dovillaire, X. Levecq, S. Bucourt, and M. Fajardo, *High-order harmonic wave fronts generated with controlled astigmatic infrared laser*, Journal of the Optical Society of America B **25**(7):B161–B166 (2008). 56, 63

[112] H. Dacasa, H. Coudert-Alteirac, C. Guo, E. Kueny, F. Campi, J. Lahl, J. Peschel, H. Wikmark, B. Major, E. Malm, D. Alj, K. Varjú, C. L. Arnold, G. Dovillaire, P. Johnsson, *et al.*, *Single-shot extreme-ultraviolet wavefront measurements of high-order harmonics*, Optics Express **27**(3):2656–2670 (2019). 56, 63

[113] D. G. Lee, J. J. Park, J. H. Sung, and C. H. Nam, *Wave-front phase measurements of high-order harmonic beams by use of point-diffraction interferometry*, Optics Letters **28**(6):480–482 (2003). 56, 74

[114] E. Frumker, G. G. Paulus, H. Niikura, D. M. Villeneuve, and P. B. Corkum, *Frequency-resolved high-harmonic wavefront characterization*, Optics Letters **34**(19):3026–3028 (2009). 56

[115] E. Frumker, G. G. Paulus, H. Niikura, A. Naumov, D. M. Villeneuve, and P. B. Corkum, *Order-dependent structure of high harmonic wavefronts*, Optics Express **20**(13):13870–13877 (2012). 56, 61

[116] H. Wikmark, C. Guo, J. Vogelsang, P. W. Smorenburg, H. Coudert-Alteirac, J. Lahl, J. Peschel, P. Rudawski, H. Dacasa, S. Carlstrm, S. Maclot, M. B. Gaarde, P. Johnsson, C. L. Arnold, and A. L'Huillier, *Spatiotemporal coupling of attosecond pulses*, Proceedings of the National Academy of Sciences **116**(11):4779–4787 (2019). 56, 61, 65

[117] D. R. Austin, T. Witting, C. A. Arrell, F. Frank, A. S. Wyatt, J. P. Marangos, J. W. Tisch, and I. A. Walmsley, *Lateral shearing interferometry of high-harmonic wavefronts*, Optics Letters **36**(10):1746–1748 (2011). 56

[118] L. Freisem, G. S. M. Jansen, D. Rudolf, K. S. E. Eikema, and S. Witte, *Spectrally resolved single-shot wavefront sensing of broadband high-harmonic sources*, Optics Express **26**(6):6860–6871 (2018). 56, 59

[119] L. Loetgering, M. Baluktsian, K. Keskinbora, R. Horstmeyer, T. Wilhein, G. Schtz, K. S. E. Eikema, and S. Witte, *Generation and characterization of focused helical x-ray beams*, Science Advances **6**(7):eaax8836 (2020). 57

[120] M. Du, L. Loetgering, K. S. E. Eikema, and S. Witte, *Measuring laser beam quality, wavefronts, and lens aberrations using ptychography*, Optics Express **28**(4):5022–5034 (2020). 57

[121] D. Goldberger, D. Schmidt, J. Barolak, B. Ivanic, C. G. Durfee, and D. E. Adams, *Spatiospectral characterization of ultrafast pulse-beams by multiplexed broadband ptychography*, Optics Express **29**(20):32474–32490 (2021). 57

[122] C. M. Kewish, M. Guizar-Sicairos, C. Liu, J. Qian, B. Shi, C. Benson, A. M. Khounsary, J. Vila-Comamala, O. Bunk, J. R. Fienup, A. T. Macrander, and L. Assoufid, *Reconstruction of an astigmatic hard X-ray beam and alignment of K-B mirrors from ptychographic coherent diffraction data*, Optics Express **18**(22):23420–23427 (2010). 57

[123] B. J. Daurer, S. Sala, M. F. Hantke, H. K. N. Reddy, J. Bielecki, Z. Shen, C. Nettelblad, M. Svenda, T. Ekeberg, G. A. Carini, P. Hart, T. Osipov, A. Aquila, N. D. Loh, F. R. N. C. Maia, *et al.*, *Ptychographic wavefront characterization for single-particle imaging at x-ray lasers*, Optica **8**(4):551–562 (2021). 57

[124] P. Thibault and A. Menzel, *Reconstructing state mixtures from diffraction measurements*, Nature **494**(7435):68–71 (2013). 57

[125] R. Rhrich, A. F. Koenderink, S. Witte, and L. Loetgering, *Spatial coherence control and analysis via micromirror-based mixed-state ptychography*, New Journal of Physics **23**(5):053016 (2021). 57

[126] S. Witte and K. S. E. Eikema, *Ultrafast Optical Parametric Chirped-Pulse Amplification*, IEEE Journal of Selected Topics in Quantum Electronics **18**(1):296–307 (2012). 57

[127] L. Loetgering, T. Aidukas, M. Du, D. B. Flaes, D. Penagos, M. Rose, A. Pelekanidis, A. D. Beurs, W. Eschen, J. Hess, T. Wilhein, R. Heintzmann, J. Rothhardt, and S. Witte, *ptyLab: a cross-platform inverse modeling toolbox for conventional and Fourier ptychography*, in *OSA Imaging and Applied Optics Congress 2021 (3D, COSI, DH, ISA, pcAOP)*, p. CW6B.3, Optica Publishing Group (2021). 60

[128] L. Loetgering, X. Liu, A. C. De Beurs, M. Du, G. Kuijper, K. S. E. Eikema, and S. Witte, *Tailoring spatial entropy in extreme ultraviolet focused beams for multispectral ptychography*, Optica **8**(2):130–138 (2021). 72, 73, 74

[129] K. Schafer, B. Yang, L. DiMauro, and K. Kulander, *Above threshold ionization beyond the high harmonic cutoff*, Physical review letters **70**(11):1599 (1993). 72

[130] K. Varju, P. Johnsson, J. Mauritsson, A. L'Huillier, and R. Lopez-Martens, *Physics of attosecond pulses produced via high harmonic generation*, American Journal of Physics **77**(5):389–395 (2009). 72

[131] G. Cerullo, A. Dienes, and V. Magni, *Space–time coupling and collapse threshold for femtosecond pulses in dispersive nonlinear media*, Optics Letters **21**(1):65–67 (1996). 72

[132] B. Beaurepaire, D. Guénot, A. Vernier, F. Böhle, M. Perrier, A. Jullien, R. Lopez-Martens, A. Lifschitz, and J. Faure, *Limitations in ionization-induced compression of femtosecond laser pulses due to spatio-temporal couplings*, optics Express **24**(9):9693–9705 (2016). 72

[133] M. A. Porras, *Propagation-induced changes in the instantaneous polarization state, phase, and carrier-envelope phase of few-cycle pulsed beams*, Journal of the Optical Society of America B **30**(6):1652–1659 (2013). 73

[134] A. L. Cavalieri, N. Müller, T. Uphues, V. S. Yakovlev, A. Baltuška, B. Horvath, B. Schmidt, L. Blümel, R. Holzwarth, S. Hendel, *et al.*, *Attosecond spectroscopy in condensed matter*, Nature **449**(7165):1029–1032 (2007). 73

[135] M. Schultze, M. Fieß, N. Karpowicz, J. Gagnon, M. Korbman, M. Hofstetter, S. Neppl, A. L. Cavalieri, Y. Komninos, T. Mercouris, *et al.*, *Delay in photoemission*, science **328**(5986):1658–1662 (2010). 73

[136] B. Zhang, D. F. Gardner, M. H. Seaberg, E. R. Shanblatt, C. L. Porter, R. Karl, C. A. Mancuso, H. C. Kapteyn, M. M. Murnane, and D. E. Adams,

Ptychographic hyperspectral spectromicroscopy with an extreme ultraviolet high harmonic comb, Optics express **24**(16):18745–18754 (2016). 73

[137] H. Wikmark, C. Guo, J. Vogelsang, P. W. Smorenburg, H. Coudert-Alteirac, J. Lahl, J. Peschel, P. Rudawski, H. Dacasa, S. Carlström, *et al.*, *Spatiotemporal coupling of attosecond pulses*, Proceedings of the National Academy of Sciences **116**(11):4779–4787 (2019). 73, 79, 81

[138] E. Frumker, G. G. Paulus, H. Niikura, A. Naumov, D. M. Villeneuve, and P. B. Corkum, *Order-dependent structure of high harmonic wavefronts*, Optics Express **20**(13):13870 (2012). 73, 74

[139] L. Quintard, V. Strelkov, J. Vabek, O. Hort, A. Dubrouil, D. Descamps, F. Burgy, C. Péjot, E. Mével, F. Catoire, *et al.*, *Optics-less focusing of XUV high-order harmonics*, Science advances **5**(4):eaau7175 (2019). 73, 77

[140] M. Hoflund, J. Peschel, M. Plach, H. Dacasa, K. Veyrinas, E. Constant, P. Smorenburg, H. Wikmark, S. Maclot, C. Guo, *et al.*, *Focusing Properties of High-Order Harmonics*, Ultrafast Science **2021** (2021). 73

[141] M. B. Gaarde, F. Salin, E. Constant, P. Balcou, K. J. Schafer, K. C. Kulander, and A. L'Huillier, *Spatiotemporal separation of high harmonic radiation into two quantum path components*, Physical Review A **59**(2):1367–1373 (1999). 73

[142] F. Catoire, A. Ferré, O. Hort, A. Dubrouil, L. Quintard, D. Descamps, S. Petit, F. Burgy, E. Mével, Y. Mairesse, *et al.*, *Complex structure of spatially resolved high-order-harmonic spectra*, Physical Review A **94**(6):063401 (2016). 73, 74

[143] D. R. Austin, T. Witting, C. A. Arrell, F. Frank, A. S. Wyatt, J. P. Marangos, J. W. Tisch, and I. A. Walmsley, *Lateral shearing interferometry of high-harmonic wavefronts*, Optics letters **36**(10):1746–1748 (2011). 74

[144] D. T. Lloyd, K. O'Keeffe, and S. M. Hooker, *Complete spatial characterization of an optical wavefront using a variable-separation pinhole pair*, Optics letters **38**(7):1173–1175 (2013). 74

[145] L. Freisem, G. Jansen, D. Rudolf, K. Eikema, and S. Witte, *Spectrally resolved single-shot wavefront sensing of broadband high-harmonic sources*, Optics express **26**(6):6860–6871 (2018). 74

[146] M. Du, L. Loetgering, K. S. E. Eikema, and S. Witte, *Measuring laser beam quality, wavefronts, and lens aberrations using ptychography*, Optics Express **28**(4):5022 (2020). 74

[147] M. Du, X. Liu, A. Pelekanidis, F. Zhang, L. Loetgering, P. Konold, C. L. Porter, P. Smorenburg, K. S. E. Eikema, and S. Witte, *High-resolution wavefront sensing and aberration analysis of multi-spectral extreme ultraviolet beams*, Optica **10**(2):255 (2023). 74, 75, 79, 82

[148] A. L'Huillier, P. Balcou, S. Candel, K. J. Schafer, and K. C. Kulander, *Calculations of high-order harmonic-generation processes in xenon at 1064 nm*, Physical Review A **46**(5):2778 (1992). 74

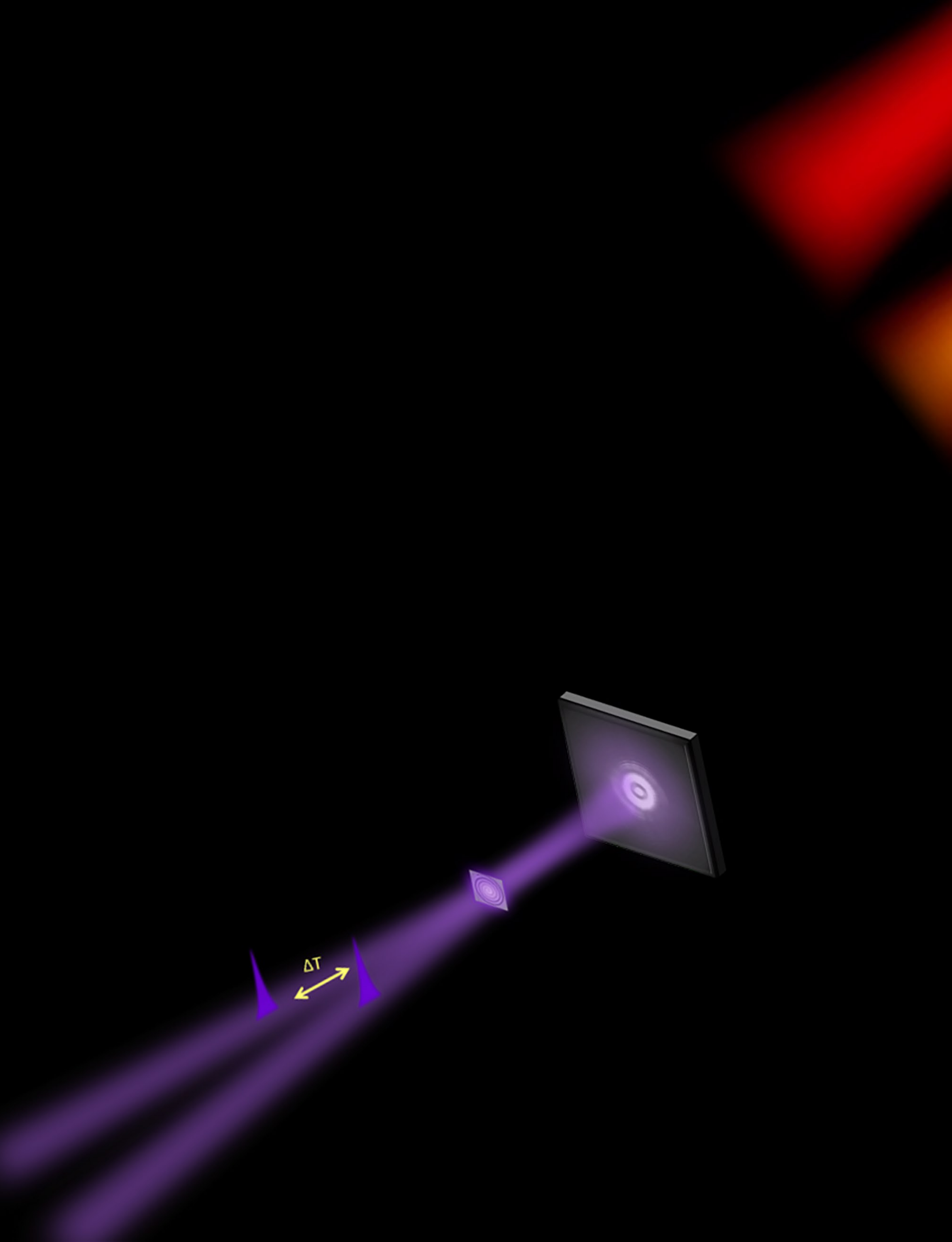
ΔT